Master's thesis

NTNU
Norwegian University of Science and Technology
Faculty of Natural Sciences
Department of Materials Science and Engineering

Marthe Nybrodahl

# The effect of MgO-addition on sintering properties and Li-ion conductivity of solid-state electrolytes with composition $Li_{6.25}Al_{0.25}La_3Zr_2O_{12}$

Master's thesis in Materials Science and Engineering
Supervisor: Kjell Wiik
Co-supervisor: Mari-Ann Einarsrud and Leif Olav Jøsang
June 2022

NTNU
Norwegian University of Science and Technology

Marthe Nybrodahl

# The effect of MgO-addition on sintering properties and Li-ion conductivity of solid-state electrolytes with composition $Li_{6.25}Al_{0.25}La_3Zr_2O_{12}$

Master's thesis in Materials Science and Engineering
Supervisor: Kjell Wiik
Co-supervisor: Mari-Ann Einarsrud and Leif Olav Jøsang
June 2022

Norwegian University of Science and Technology
Faculty of Natural Sciences
Department of Materials Science and Engineering

NTNU
Norwegian University of
Science and Technology

# Preface

This master's thesis was carried out and written as part of the TMT4905 course at the Department of Materials Science and Engineering at the Norwegian University of Science and Technology.

I would like to start of by thanking my main supervisor, Prof. Kjell Wiik, for his wonderful guidance and continued support throughout the entire process. I greatly appreciate your inputs and suggestions, along with your patience and openness to answer any and all of my never-ending questions. Furthermore, I would also like to thank my co-supervisor Leif Olav Jøsang, in addition to the other employees at CerPoTech, for their valuable input and practical assistance.

Last, but not least, thank you to my amazing family who have supported me through this thesis and throughout my whole course of study. A huge thanks to all of my friends. You guys never fail to brighten my day and are what keeps me on my feet. I am and will forever be grateful for that. A last shout-out goes to the "Lunch Crew": Our breaks were among the highlights of my day! Thanks for making me smile, even on the toughest of days.

- Marthe Nybrodahl

> "No matter what, you keep finding something to fight for."
>
> Joel, The Last of Us

# Abstract

As a result of exhibiting high ionic conductivity and good stability against Li-metal, LALZO is a promising candidate for solid-electrolyte purposes in the next generation solid-state batteries. However, the material is known to suffer from abnormal grain growth (AGG) after sintering. MgO-addition was therefore introduced with the aim of reducing AGG through formation of a secondary MgO-phase on the grain boundaries. In this work, the effect of MgO-addition on the sintering properties and the Li-ion conductivity of $Li_{6.25}Al_{0.25}La_3Zr_2O_{12}$ (LALZO), produced by spray pyrolysis at CerPoTech AS, have been investigated. Three different ceramic powders were produced, with stoichiometries 0, 1 and 5 mol% MgO.

Calcination at 750 °C for 12 h in MgO-crucibles resulted in a single-phase cubic LALZO (c-LALZO) material. After sintering at 1150 °C for 1 and 6 hours, using a bedpowder ratio of 2 and MgO-crucibles, the pellets consisted of primarily c-LALZO and small amounts of secondary phases. Moreover, no Mg-containing compounds were observed by X-ray diffraction (XRD). The observation of large grains near the surface of pellets sintered at elevated temperatures (1200 °C) or by extended sintering time (6 h), revealed that the MgO-addition did not have the intended effect of reducing AGG. Energy-dispersive spectroscopy (EDS) analysis and a reduced cell parameter with increasing MgO-content showed that Mg was incorporated at either Zr-sites or Li-sites in the LALZO lattice. This had a negative impact on the total Li-ion conductivity, and decreasing conductivities were observed with increasing Mg-content. Furthermore, the samples experiencing AGG exhibited higher conductivities as a result of the reduced grain boundary resistance. The highest ionic conductivity was $1.46 \times 10^{-4}$ S/cm, achieved for the Mg-free sample sintered at 1150 °C for 6 h. The lowest ionic conductivity was $0.74 \times 10^{-4}$ S/cm, achieved for the 5 mol% MgO sample sintered at 1150 °C for 1 h. AGG was, however, found to reduce the mechanical strength of the material.

It is concluded that since Mg substitutes lattice sites and reduce the Li-ion conductivity, other strategies must be chosen to suppress AGG.

# Sammendrag

Som et resultat av den høye ioniske ledningsevnen og den gode stabiliteten mot Li metall er LALZO en lovende kandidat til bruk som faststoffelektrolytt i neste-generasjons faststoffbatteri. Materialet er imidlertid kjent for å lide av enorm kornvekst (AGG) etter sintring. MgO-tilsats ble derfor introdusert med et mål om å redusere AGG gjennom dannelse av en sekundær MgO-fase på korngrensene. I dette arbeidet har effekten av MgO-tilsats på sintringsegenskapene og Li-ioneledningsevnen til $Li_{6.25}Al_{0.25}La_3Zr_2O_{12}$ (LALZO), produsert ved spraypyrolyse av CerPoTech AS, blitt undersøkt. Tre forskjellige keramiske pulver ble produsert, med støkiometriene 0, 1 og 5 mol% MgO.

Kalsinering ved 750 °C i 12 timer i MgO-digler resulterte i et enfase kubisk LALZO (c-LALZO) materiale. Etter sintring ved 1150 °C i 1 og 6 timer, ved bruk av et "bedpowder-forhold" på 2 og MgO-digler, besto pelletene hovedsakelig av c-LALZO og små mengder sekundærfaser. Videre ble ingen Mg-innholdige faser observert ved røntgendiffraksjon (XRD). Observasjonen av store korn nær overflaten av pellets sintret ved høye temperaturer (1200 °C) eller ved forlenget sintringstid (6 timer) avslørte at MgO-tilsatsen ikke hadde den forventede effekten ved å redusere AGG. Energidispersiv spektroskopianalyse og en redusert celleparameter med økende MgO-innhold avslørte at Mg ble inkorporert på enten Zr-plass eller Li-plass i LALZO-gitteret. Dette hadde negativ innvirkning på den totale ioniske ledningsevnen, og synkende ledningsevne ble observert med økende Mg-innhold. Prøvene som opplever AGG har høyere ledningsevne, som et resultat av redusert korngrensemotstand. Den høyeste ioniske ledningsevnen var $1.46 \times 10^{-4}$ S/cm, oppnådd for den Mg-frie prøven sintret ved 1150 °C i 6 timer. Den laveste ioniske ledningsevnen var $0.74 \times 10^{-4}$ S/cm, oppnådd for 5 mol% MgO prøven sintret ved 1150 °C i 1 time. AGG ble derimot funnet til å redusere den mekaniske styrken til materialet.

Konklusjonen er at ettersom Mg substitueres på gitterposisjoner og reduserer Li-ioneledningsevnen, må andre strategier velges for å undertrykke AGG.

# Table of Contents

**List of abbreviations**

| | |
|---|---|
| AC | Alternating current |
| AGG | Abnormal grain growth |
| BP-ratio | Bedpowder ratio |
| BSE | Backscattered electrons |
| CIP | Cold isostatic pressing |
| DC | Direct current |
| EDS | Energy-dispersive X-ray spectroscopy |
| EIS | Electrochemical impedance spectroscopy |
| GB | Grain boundary |
| HT | High temperature |
| ICP-MS | Inductively coupled plasma mass spectroscopy |
| LALZO | $Li_{6.25}Al_{0.25}La_3Zr_2O_{12}$ |
| LLZO | $Li_7La_3Zr_2O_{12}$ |
| LIB | Li-ion battery |
| LT | Low temperature |
| RT | Room temperature |
| SEI | Solid electrolyte interface |
| SE | Secondary electrons |
| SEM | Scanning electron microscope |
| SSB | Solid-state battery |
| SSE | Solid-state electrolyte |
| VLCs | Volatile lithium compounds |
| WDS | Wavelength-dispersive spectroscopy |
| xMgO-LALZO | x mol% added $Li_{6.25}Al_{0.25}La_3Zr_2O_{12}$ (x = 0, 1 or 5) |
| XRD | X-ray diffraction |

# List of Figures

# List of Tables

# 1 Introduction

## 1.1 Background & motivation

The Li-ion battery (LIB) is the dominant secondary battery technology today, being utilized in for instance portable electronics and electrical vehicles. These batteries have many desirable properties that makes them popular, mainly high cell voltage, specific capacity and energy density. Despite these advantages, there are still room for improvements regarding limitations in capacity and safety considerations. The importance of battery technology will continue to increase as we move towards the energy transition and a greener future. One proposed battery technology that have gained a lot of attention is the solid-state battery (SSB).

In SSBs, the liquid electrolytes used in traditional LIBs have been replaced with a ceramic solid-state electrolyte (SSE), as shown in Figure 1.1. The solid electrolyte eliminates the need of a separator, as the electrolyte works as both the separator and the ionic conductor. This material should therefore be a good ionic conductor to allow high Li-ion mobility, while being a poor electronic conductor to avoid short-circuiting. Furthermore, the ceramic is non-flammable, as opposed to the liquid electrolyte, which eliminates fire hazards and toxic gases. This also reduces the risk of thermal runaway, where parasitic reactions cause uncontrollable, self-sustaining heat generation [1]. This allows for a more compact battery cell, giving increased design flexibility and volumetric density.

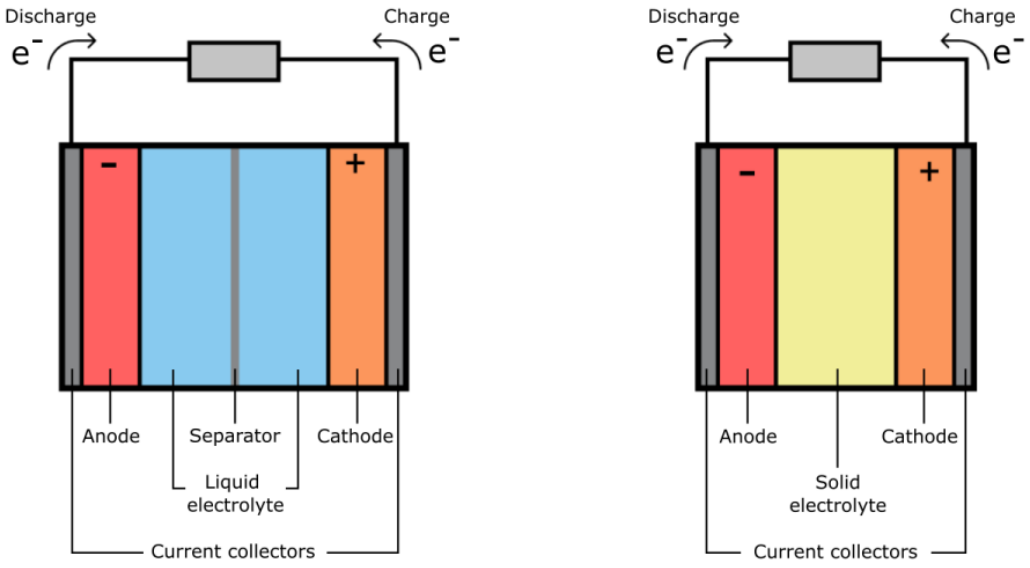


**Figure 1.1:** Schematic of Li-ion battery with liquid electrolyte (left) and solid-state battery (right)

A promising alternative for the use as an SSE is $Li_{6.25}Al_{0.25}La_3Zr_2O_{12}$ (LALZO). This is a ceramic material with a garnet-like crystal structure, consisting of $Li_7La_3Zr_2O_{12}$ (LLZO) doped with Al. There are two possible polymorphs of LLZO: A room temperature (RT) stable tetragonal structure

and a cubic structure. The cubic structure is found to have two orders of magnitude higher ionic conductivity, meaning that stabilisation of the cubic phase, here achieved by doping with Al, is desirable to enhance the ionic conductivity [2]. In addition to high ionic conductivity, other advantageous properties include a wide electrochemical potential window [3]. This means that over the applied potential range, the electrolyte does not experience any electrochemical oxidation or reduction reactions and is thus stable over a wide potential region [4]. In addition, LALZO also exhibit high (chemical) stability against Li-metal [3]. This allows for the implementation of Li-metal anodes, which have 10 times higher specific capacity compared to the graphite anodes used in today's LIBs [5]. Using Li-metal anodes in combination with solid electrolytes eliminates the breakdown of the solid electrolyte interface (SEI) and subsequent growth of Li-metal dendrites, due to the high mechanical strength of the ceramic material [6], [7].

A common challenge associated with LALZO, is that they suffer from abnormal grain growth (AGG) during sintering [8]–[10]. This is expected to cause a reduction in both the mechanical strength and ionic conductivity due to reduced densification. In this work, MgO-added LALZO powders, produced by spray pyrolysis by CerPoTech AS, will be studied. The intention is that formation of a secondary MgO-phase on the grain boundaries may reduce the grain growth, without negatively affecting the other properties. Spray pyrolysis is a soft, wet-chemical synthesis technique used in production of powder precursors with particle size in the nano range. This technique has multiple benefits compared to the more commonly applied solid-state processes or co-precipitation methods. Spray pyrolysis allows for precise control of particle size, morphology and stoichiometry. The technique produces both homogeneous and composite powders of high purity, while being affordable and can easily be scaled up for mass production [11], [12].

## 1.2 Aim & scope

This work aims to investigate the sintering properties of MgO-added LALZO powders produced by spray pyrolysis, with varying MgO-contents of 0, 1 and 5 mol% MgO. This will be done by conducting a series of sintering experiments, varying parameters like sintering temperature and sintering time, bedpowder-ratio and crucible material. The sintering mechanism and phase composition will be assessed by dilatometry and X-ray diffraction (XRD), respectively. The microstructure will be characterized by scanning electron microscopy (SEM), while semi-quantitative elemental analysis will be evaluated by energy-dispersive spectroscopy (EDS). The density of the sintered pellets will be assessed by using Archimedes' method. Lastly, the Li-ion conductivity will be measured by electrochemical impedance spectroscopy (EIS). The aim is to establish a sintering procedure that results in a dense, single-phase c-LALZO material that satisfies the requirements for the use as a solid-state electrolyte.

# 2 Theory

This section includes the relevant theoretical background to understand and explain the results from this work and is to some degree based on the theory presented in the specialization project by Nybrodahl [13]. The section presents various aspects relating to LALZO, including: The structure and crystallographic properties, the thermodynamics of the system, doping and intermediate phases, and an assessment of the $Li^+$ conductivity and sintering behavior.

## 2.1 $Li_7La_3Zr_2O_{12}$ - LLZO

The garnet-like structured Li-oxide $Li_7La_3Zr_2O_{12}$ (LLZO) has quickly become one of the most promising candidates for the use as an electrolyte in solid-state batteries. LLZO exhibits high $Li^+$-conductivity at RT, low activation energy, good mechanical and thermal stability. Furthermore, LLZO is both chemically and electrochemically compatible with Li-metal anodes and common cathode materials. Since being initially introduced by Murugan et al. in 2007 [14], LLZO have been extensively researched and major progress have been made to improve the chemical and physical properties, in hopes of achieving highly conductive LLZO SSE-material.

General garnets have the formula $A_3B_2C_3O_{12}$, where A are 8-coordinated dodecahedral sites, B are 6-fold coordinated octahedral sites and C are 4-fold coordinated tetrahedral sites. For the LLZO structure, the A, B and C sites are occupied by $La^{3+}$, $Zr^{4+}$ and $Li^+$, respectively. $Li^+$ also occupy other sites in the oxygen framework. Compared to traditional garnets, 4 additional $Li^+$ per formula unit is present at interstitial lattice sites, giving the formula $Li_7La_3Zr_2O_{12}$. This allows for increased ionic conductivity [15], [16].

The LLZO system has two known polymorphs. The first is a tetragonal modification ($I4_1/acd$, No. 142), which has a fully occupied and completely ordered $Li^+$-arrangement. The lattice structure consists of $LaO_8$ polyhedra (at the Wyckoff position *8b* and *16e*) and $ZrO_6$ octahedra (*16c*), with $Li^+$ occupying three different sites: Li(1) (tetrahedral *8a* sites), and Li(2) and Li(3) (distorted octahedral *16f* and *32g* sites). The extra $Li^+$ in the formula unit causes distortion of the LLZO lattice. This gives rise to this tetragonal modification, which is not commonly observed for traditional garnets. The other possible polymorph is the cubic modification ($Ia\bar{3}d$, No. 230). Compared to the tetragonal structure, the cubic structure displays a disordered $Li^+$-arrangement. The lattice structure consists of 8-fold coordinated $LaO_8$ dodecahedra (*24c*) and 6-fold coordinated $ZrO_6$ octahedra (*16a*), with $Li^+$ occupying interstitial sites (tetrahedral *24d*, octahedral *48g* and distorted 4-fold *96h* coordination) [17], [18]. The crystal structure of tetragonal LLZO and cubic LLZO is shown in Figure 2.1 and Figure 2.2, respectively.

Due to the lower/partial occupancy of the cubic structure, the number of available positions for $Li^+$-mitigation is higher. This makes it more desirable for the use as a solid electrolyte, due to

having Li-ion conductivities that are 2 orders of magnitude higher than the tetragonal structure [2], [19]–[21]. The appearance of the tetragonal modification is a result of the distortion of the lattice due to the additional Li-ions [19]. The tetragonal is also the phase that is stable at RT, though the cubic modification can be stabilized through doping with supervalent cations. This causes a reduced $Li^{+}$-content, which gives rise to additional Li-vacancies. The formation of vacancies and the disordered Li-arrangement causes enhanced entropy of the system, which gives a reduction in the Gibbs free energy of the cubic modification. This allows for a preferred stabilization of the the cubic phase [17], [22], [23]. Options for possible cations are many, with $Al^{3+}$ being one of the most common and will be discussed in Section 2.2.2.

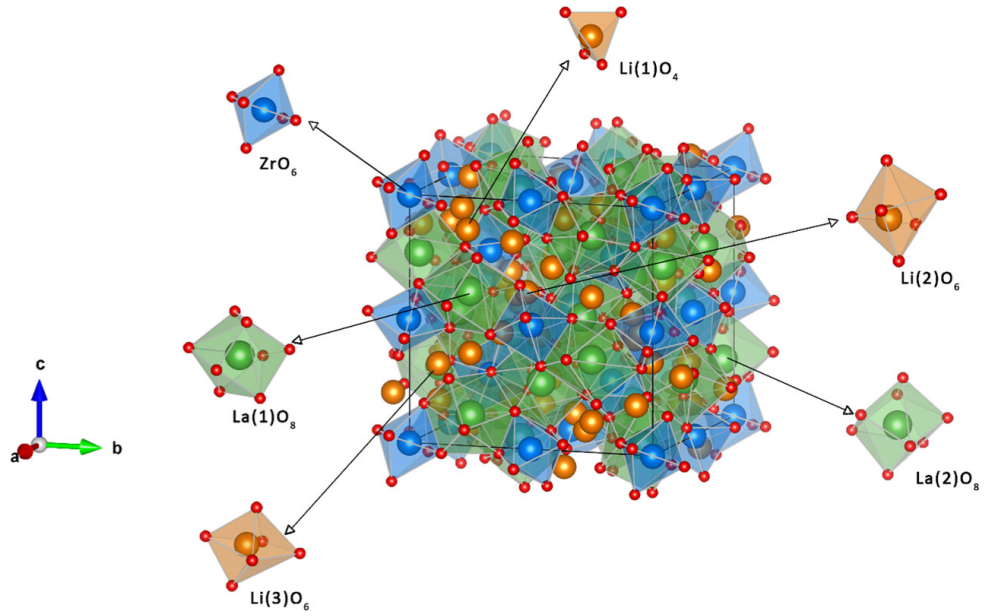


**Figure 2.1:** Crystal structure of tetragonal $Li_7La_3Zr_2O_{12}$. Dodecahedral La-coordination sites are shown in green (*8b* and *16e*), octahedral Zr-coordination sites are shown in blue (*16c*) and the different Li-coordination sites are shown in orange (*8a*, *16f* and *32g*). Adopted from Yeandel et al. [18].

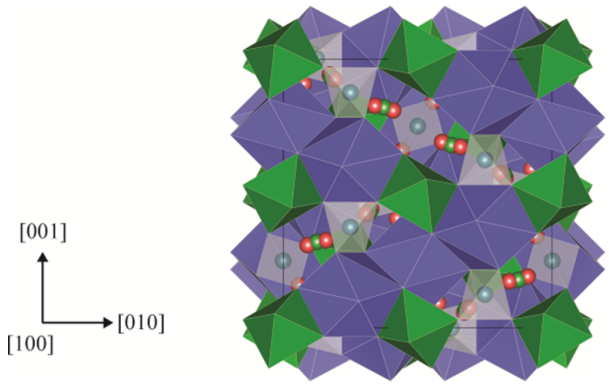


**Figure 2.2:** Crystal structure of cubic $Li_7La_3Zr_2O_{12}$. Dodecahedral La-coordination sites are shown in blue (*24c*), octahedral Zr-coordination sites are shown in green (*16a*) and the different Li-coordination sites are shown as blue, green and red spheres, representing tetrahedral (*24d*), octahedral (*48g*) and distorted 4-fold coordinated (*96h*) sites, respectively. Adopted from Rettenwander et al. [16].

## 2.2 LLZO phases, doping and thermodynamic considerations

It is reported that LLZO has three phases: A tetragonal phase, a low temperature (LT)-cubic phase formed by reactions with moisture or $CO_2$ and a high temperature (HT)-cubic phase with superior ionic conductivity [24]–[26]. Due to the low conductivities of the other phases, the (HT)-cubic phase is the only suitable option for SSBs. Conductivity values of above $1 \times 10^{-4}$ S/cm have been reported for (HT)-cubic, while only around $1 \times 10^{-6}$ S/cm for the other two phases [19].

### 2.2.1 Undoped LLZO

As stated previously, the tetragonal phase is the most stable polymorph at RT. Repulsive electrostatic forces between the Li-ions at the fully occupied Li-sites in structure causes increased Li-Li interatomic distance. To relieve the built-up internal strain, the lattice gets distorted and consequentially induces a tetragonal transformation [25], [27]. The complete occupancy impede migration between Li-sites, decreasing the number of equivalent positions and hence lowers the $Li^+$-conductivity [2].

The transition between phases and their stability are governed by the thermodynamic properties of the system. The free energy of the tetragonal-to-cubic phase transition can be described by Equation 2.1:

$$\Delta G_{t\to c} = \Delta H_{t\to c} - T\Delta S_{t\to c} \tag{2.1}$$

where $\Delta G_{t\to c}$ is the Gibbs free energy, $\Delta H_{t\to c}$ is the enthalpy, $T$ is the absolute temperature and $\Delta S_{t\to c}$ is the entropy. Due to the low ionic conductivity of the tetragonal phase, it is desirable to find ways to induce the tetragonal-to-cubic transition. A transition can be regarded as spontaneous when the Gibbs free energy is negative. As a result of the different ordering of the tetragonal phase (ordered) and the cubic phase (disordered), these phases possess different entropies and internal free energies. The entropy term is dependent on temperature, where increasing temperature gives a more negative term. This means that the tetragonal-to-cubic transition should be spontaneous at *some* elevated temperature. This is the case regardless of the Li-content, though increased Li-vacancy concentration is found to lower this temperature [27]. The temperature at which $\Delta G_{t\to c}$ is 0, is called the transition temperature ($T_t$). Table 2.1 lists examples of values for $T_t$, as reported in the literature.

Based on this, the literature agrees that $T_t$ is somewhere between 610-650 °C. Some sources report transition temperatures in the range 100-200 °C, though this have been proven to be as a result of hydration of the structure via contact with water molecules or by $H^+/Li^+$ exchange [15], [28]. Further heat treatment of LLZO should therefore be conducted according to this, by applying tem-

peratures that induces this transition. Furthermore, other novel strategies to induce this transition have been studied. Li et al. successfully induced the tetragonal-to-cubic transition by combining sol-gel synthesis and high-energy planetary milling. Hence, low-temperature synthesis of c-LLZO can be obtained without the need of high-temperature calcinations [29].

**Table 2.1:** Transition temperatures for the tetragonal-to-cubic phase transition

| Transition temperature [°C] | Author |
|---|---|
| 610 - 630 | Wang and Lai [24] |
| 650 | Matsui et al. [30] |
| ∼630 | Chean et al. [31] |
| ≃645 | Larraz et al. [28] |

The tetragonal-to-cubic transition is, however, reversible. This means that the cubic phase is not quenchable to RT [30]. Thus, undoped LLZO cannot be applied as a SSE-material. However, when LLZO is doped with supervalent cations, this substitution leads to an increase in the Li-vacancy concentration and allows for stabilization of the cubic phase at RT. Two different substitution strategies are commonly applied: (i) Using cations that substitutes for Li, which reduces the Li-content and thus stabilizes the cubic phase. Examples include $Al^{3+}$ and $Ga^{3+}$. However, this causes obstructions in the $Li^{+}$-diffusion paths and can lead to reduced conductivity. (ii) Using cations that substitutes on i.e., Zr-sites, that still reduces the Li-content while avoiding obstruction of the Li-pathways. Examples include $Nb^{4+}$, $Ta^{5+}$ and $Te^{6+}$ [26], [28], [32]–[34].

### 2.2.2 Al-doped LLZO

Aluminium is one of the most studied dopants in the LLZO-system. This is due to accidental contamination of "undoped LLZO-samples", caused by reactions with $Al_2O_3$-crucibles. This caused $Al^{3+}$-ions to unintentionally be incorporated into the structure [15]. Despite this, incorporation of Al was later found to stabilize and densify the cubic LLZO phase [35]–[37].

The stabilization of the cubic phase is achieved by formation of Li-vacancies. As the vacancy concentration increases, ordering of the $Li^{+}$-ions becomes energetically unfavorable due to a higher degree of entropy. This also causes the interatomic distance between the Li-ions to increase, which reduces the repulsive forces. Stabilization of the cubic phase, or rather the avoidance of tetragonal distortion, is thus achieved [27]. As trivalent $Al^{3+}$ gets doped into the system, $Li^{+}$ substitution occurs. This causes a disruption of the charge neutrality, meaning each Al atom needs to form two Li vacancies [15], [38]. The balanced defect chemistry for Al-doping can be described according to Equation 2.2 (Kröger-Vink notation).

$$6\mathrm{Li}_{\mathrm{Li}}{}^{x} + \mathrm{Al}_2\mathrm{O}_3(s) = 2\mathrm{Al}_{\mathrm{Li}}^{\bullet\bullet} + 4V_{\mathrm{Li}}^{'} + 3\mathrm{Li}_2\mathrm{O}(g) \tag{2.2}$$

The nominal composition of the compound is therefore $\mathrm{Li}_{7-3x}\mathrm{Al}_x\mathrm{La}_3\mathrm{Zr}_2\mathrm{O}_{12}$, where altering the Al-content directly affect the tetragonal-to-cubic transition. This effect is clearly illustrated in the phase diagram produced by Matsuda et al. [25], as shown in Figure 2.3. As the Al content (x) increases, the transition temperature decreases, until 0.2 Al per formula unit (or 0.4 Li vacancies per formula unit). Above this, there is a drop-off and at 0.25 Al per formula unit, the cubic phase is stable at RT [25]. Thus, there is a solubility limit of $\mathrm{Al}^{3+}$ in the system: At ca. $\geq$ 0.21 Al per formula unit, it is possible to quench the cubic phase to RT due to the slow transition rate. Similar results have also been reported by other researchers in the literature. Bernstein et. al reported that above 0.4 Li vacancies per formula unit LLZO results in the cubic phase having lower energy compared to the tetragonal phase [27], while Rangasamy et al. found that 0.204 moles of Al stabilized the cubic phase [37].

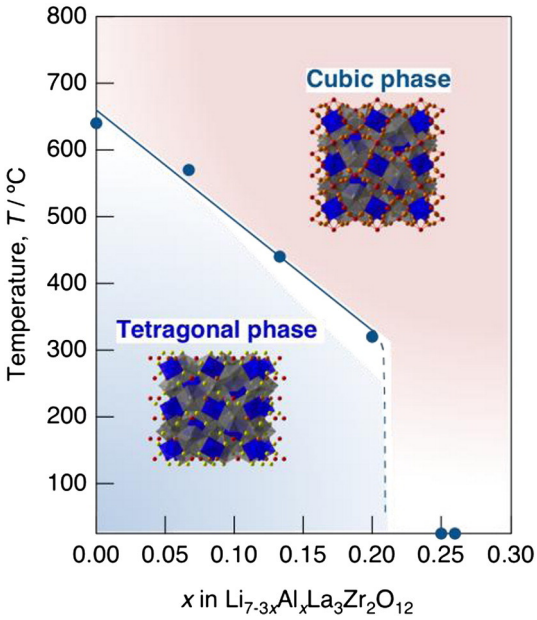


**Figure 2.3:** Phase diagram of Al-doped LLZO, adopted from Matsuda et al. [25]

An additional beneficial aspect of Al-doping is that it works as a sintering aid, via formation of a Li−Al−O phase. This is an amorphous phase that gets formed and distributes at the grain boundaries. Here, an increase in sintering activity gets promoted [39]. This gives increased densification, which in turn allows for higher Li-ion conductivity. This is due to enhanced Li-diffusion between the grains, lower grain boundary resistance and reduced porosity. This Li−Al−O phase is also a good ionic conductor and a poor electronic conductor, giving it additional benefits regarding the ionic conductivity [40]. A detailed crystal structure or stoichiometry of this phase is not evident from the literature. However, some reports it to be a moderately $\mathrm{Li}^{+}$ conductive glass electrolyte [41], or a high-temperature liquid phase appearing in the $\mathrm{Li}_2\mathrm{O}$-$\mathrm{Al}_2\mathrm{O}_3$ phase diagram [42].

### 2.2.3 MgO-added LALZO

A challenge commonly associated with LALZO, which have been reported both in the literature and by Eriksen [10], is the phenomenon AGG. AGG appears to be related to the formation of a $Li_2O$-$Al_2O_3$ liquid phase at elevated temperatures. This allows for liquid phase sintering, which gives rise to rapid and extensive growth of a few large grains. The small neighbouring grains in the matrix have very slow growth rates. As a result of higher thermodynamic driving forces for the larger grains and due to the difference in curvature, the small grains will be consumed. This results in a coarsening of the microstructure and gives a bimodal grain size distribution [43]. This will negatively impact the resulting properties of the electrolyte, leading to deterioration of the mechanical strength. Furthermore, Li-metal dendrites experiences preferred propagation along grain boundaries. This means that the formation and growth of dendrites will occur more easily, making the material not suitable for solid electrolyte purposes. Preferably, a uniform microstructure with small, strongly bound grains is desirable in terms of density, mechanical strength and the total ionic conductivity [44]. In order to optimize the mechanical and electrochemical properties, means of reducing AGG is necessary.

The present investigation studies the effect of MgO-addition in LALZO, to determine the impact on AGG after sintering and the phase stability of the system. MgO-additives have been used to restrict grain growth in $Al_2O_3$, where the formation of a secondary $MgAl_2O_4$ (spinel) phase limits the mobility of the GBs and effectively reduces the grain growth [45], [46]. The decision of using MgO was also partially based on a suggestion from Mike Tucker, a researcher in the Tucker Research Lab at Lawrence Berkeley National Laboratory. He claims that MgO might help in reducing the grain growth in sintered samples [47].

The effect of $Mg^{2+}$-doping on densification and ionic conductivity of sintered LLZO garnets have been studied by Jiang et al., using a compound with the composition $Li_7La_3Zr_{2-x}Mg_{2x}O_{12}$ [48]. Inspired by the works of Miara et al., who found $Mg^{2+}$-doping on the octahedral Zr-sites to be stable [49], a similar substitution was applied in this work. Pellets with various Mg-content were sintered at 1075 °C for 12 h and were subsequently characterized according to the phase composition and ionic conductivity. Upon XRD analysis, a shift in the diffraction patterns was observed for the doped samples, and the lattice parameter was found to increase up until x = 0.05. After this, a slight decrease was observed. The authors claim that as $Mg^{2+}$ gets introduced into the LLZO lattice, an uneven number of $Mg^{2+}$-ions may substitute on Zr-sites. For instance, x = 0.05 gives $Li_7La_3Zr_{1.95}Mg_{0.1}O_{12}$ meaning that some Zr-sites are occupied by two $Mg^{2+}$-ions. This causes an expansion of the unit cell and an increase in the lattice parameter. When the doping content is further increased, the authors claim that the site occupancy would be saturatedly performed by one $Mg^{2+}$ on one Zr-site, meaning that the lattice parameter would be decreased due to the $Mg^{2+}$ ion being smaller than $Zr^{4+}$ (0.66Å vs. 0.79 Å) [48]. These values do however differ from those reported by Shannon, who reports identical ionic radii of 0.72 Å for 6-coordinated $Mg^{2+}$ and

$Zr^{4+}$ [50]. Furthermore, Mg-doping proved to have multiple beneficial effects on the properties of the material. A dense and homogeneous microstructure was obtained, with a uniform Mg-distribution and no noticeable grain boundaries. This was also reflected on the sintering properties and ionic conductivity, producing high-density samples (96.6 %) with a total ionic conductivity of 0.291 mS/cm at RT for a doping content of x = 0.05. The high conductivity can be attributed to the non-separable contributions of the bulk and grain boundary resistance, indicating that the grain boundary resistance is negligible. However, too high doping contents leads to a reduction of the total ionic conductivity and relative density. A trade-off between the doping level and the resulting properties and finding an optimal doping level is important in order to achieve a high-quality electrolyte material [48].

Song et al. also reports similar beneficial properties when $Mg^{2+}$ is allocated at the Zr-sites. Sintering $Li_{7.1}La_3Zr_{1.95}Mg_{0.05}O_{12}$ at 1230 °C for 16 h yielded high ionic conductivity ($4.32 \times 10^{-4}$ S/cm), a wide electrochemical stability window and good stability against Li-metal [51]. Furthermore, Yang et al. found that Mg-doping decreases the sintering temperature and duration. When MgO combines with other metal oxides in the system, solid solutions can be formed. This causes lattice distortions and can cause increased diffusivity of the grain boundaries, allowing for lower sintering temperature and -time. The authors report that Mg-doped LLZO shows a slightly lower ionic conductivity compared to LLZO without Mg, but still possesses a wide and stable electrochemical window to Li-metal [52].

The effects of MgO-addition has also been studied by Jonson et al. [53], who studied tape casted LALZO sheets with MgO introduced as a sintering additive. This was done in order to increase the density and yield a more uniform microstructure. The thin films were sintered at 1115 °C for 2-5 h in an inert Ar atmosphere. A trade-off was observed between the density and the ionic conductivity. Adding 3 wt% MgO resulted in the highest conductivity ($4.35 \times 10^{-4}$ S/cm), but gave a less dense sheet compared to other doping contents. The decrease in the conductivity associated with higher MgO-content might be attributed to reactions between the supposedly chemically inert MgO and LALZO. This is evident by the appearance of unidentified impurity peaks in the XRD-diffractograms. Furthermore, the lattice parameters changes very little regardless of the MgO-content and thus gives no indication whether Mg enters the lattice or not. SEM-micrographs do, however, reveal that AGG has been inhibited. As such, sheets with reduced grain size and small pores centered around the grain boundaries were produced. This work also illustrates the influence of sample geometry. When studying pellet samples, higher MgO-contents were necessary in order to produce a fine-grained microstructure without intragranular pores, compared to sheet-samples. Thus, optimization of Li-content, amounts of sintering additives and sintering conditions is required [53].

Huang et al. have studied sintering of a Ta-doped LLZO/MgO composite system. Here, MgO have been introduced in order to reduce AGG, while still producing a high-quality electrolyte material

[54]–[56]. The sintering temperature and holding time varied for the different publications. But the sintering temperature was generally chosen to be either 1150 °C or 1250 °C, while the duration varied from as little as 40 min to as long as 10 h. During the initial stage of the sintering, neck formation occurs between LLZO grains and the MgO is distributed uniformly in the LLZO grains and will effectively hinder material transport. This is due to the high melting point and low reactivity of MgO, making it inert towards LLZO. As the temperature is further increased during the intermediate stage of the sintering, we see continued grain growth occurring and a higher degree of connection between neighbouring grains. The final stage of sintering is associated with the formation of tightly bound polyhedron shaped LLZO-grains that agglomerate together. Meanwhile, the MgO-grains continue to grow and agglomerates. Eventually, MgO gets pushed to the triple points of the GBs where it prevents severe grain growth. By having the non-conductive MgO accumulate at the triple points, high mobility of $Li^+$ across the GBs is still achievable. The function of MgO is also illustrated in Figure 2.4. Hence, AGG can be controlled by adding MgO to LLZO. This allows for higher densities and increased fracture strength, without major interference with the ionic conductivity. Agglomeration of MgO on the triple points and the subsequent prevention of AGG have also been observed for the same composite system by other researchers [57], [58].

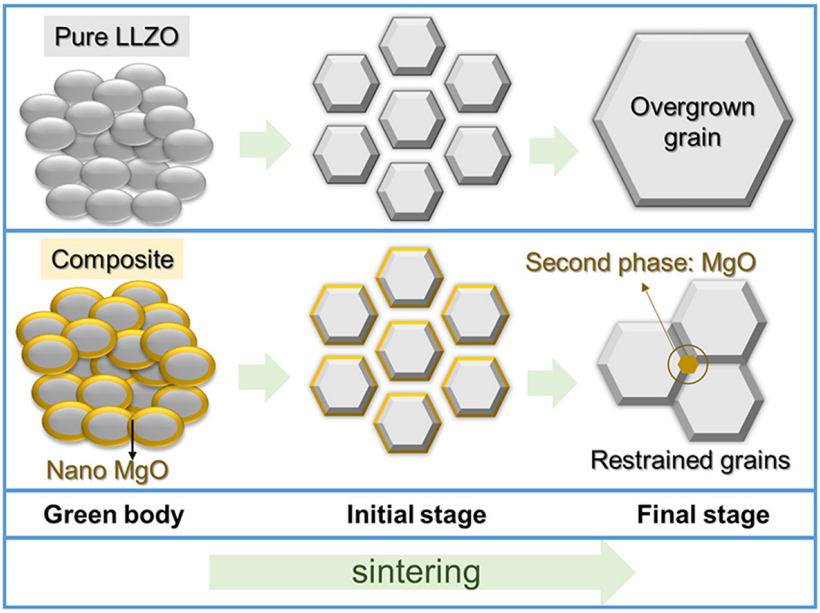


**Figure 2.4:** Schematic showing the presence of MgO, as well as the effect on the final microstructure after sintering. Adopted from Huang et al. [55]

An alternative composite system, also studied by Huang et al.[59], is the Nb-doped LLZO/MgO system. High densities were achievable even after sintering for only 1 min at 1250 °C. The cross-sectional SEM images indicate transgranular fractures, round grain edges and only a few pores. As the sintering duration is increased (40 min), the density is further increased and the pellets now experience intergranular fractures. The grain edges are well-faceted, giving tight intergrain bonding. As the duration is increased further (360 min), AGG is observed, and the degree of porosity is higher. The distribution of MgO also changes depending on the sintering duration. For

shorter sintering times, the MgO-particles are very small and has poor crystallinity, meaning no MgO-peaks is observed in the X-ray diffractograms. After prolonged sintering, they are observed in the diffractograms. The ceramic quality is however found to decrease as apparent from the fact that: (i) the samples experiences AGG, (ii) the bonds between the grains are weak and (iii) there is an increased porosity. This is specifically prevalent for low Nb-doping contents. Furthermore, the distribution of MgO is similar to the Ta-doped LLZO/MgO composite system. MgO is positioned at the triple points of the GBs, where the AGG is inhibited [59].

## 2.3 Intermediate phases

The LLZO system commonly experiences the presence of intermediate phases. These can occur due to unwanted or in-complete reactions, varying depending on the chosen precursors and the Li-content. These phases tend to negatively impact the final composition, so eliminating their presence is essential in order to yield a single phase cubic LLZO material with high ionic conductivity.

**Tetragonal LLZO** phase can commonly occur in systems where the Li content is high. Excess Li is often implemented in order to compensate for Li-losses during processing. This causes successive distortions of the LLZO lattice, giving the tetragonal polymorph. As the temperature increases, an increased Li loss will occur. This causes a transformation from tetragonal to cubic phase. It is desirable to minimize the tetragonal content, due to the lower ionic conductivity of this polymorph. XRD can help identify the existence of tetragonal phase. Despite the cubic and tetragonal phases having similar Bragg peaks, they can be distinguished on the symmetry of the tetragonal unit cell causing peak splitting. This is not the case for the cubic structure, where single Bragg peaks are produced [29], [30].

**LT-cubic LLZO** forms due to reactions with moisture and $CO_2$. This is the undesirable phase compared to the HT-cubic counterpart, as the phase formed at low temperatures has a lower ionic conductivity. This is a result of the lower Li site occupancy, causing the formation of intermediate phases such as $La_2Zr_2O_7$ (pyrochlore) and $Li_2CO_3$, which subsequently hinders Li-ion transport [30]. Formation of LT-cubic LLZO can be avoided by limiting exposure to moisture and $CO_2$, which can be achieved by utilizing a $CO_2$-free or otherwise inert atmosphere. In addition to different conductivities, the HT and LT cubic phases can be distinguished based on their lattice parameters. LT-cubic has a slightly higher lattice parameter compared to HT-cubic [25].

**$La_2Zr_2O_7$ (pyrochlore)** is one of the most common intermediate phases formed in the LLZO system. This is usually a result of Li loss at elevated temperature, causing a deficiency of Li. The presence of pyrochlore acts as an indicator of incomplete reactions or can occur after calcination and sintering due to decomposition of c-LLZO [60]–[62]. The formation of pyrochlore can be avoided by controlling the Li content via adding excess Li or trying to minimize Li-loss during processing. Utilizing bedpowders when sintering is one of the main approaches for minimizing Li-loss, by being

a source of additional Li. In addition, the pyrochlore content seems to be affected by the presence of another intermediate phase, $Li_2CO_3$. It appears that $Li_2CO_3$ needs to decompose to $Li_2O$, which can then react with pyrochlore to form c-LLZO. The decomposition rate of $Li_2CO_3$ is highly dependent on the $CO_2$-partial pressure. When calcining larger batches at moderate temperatures, the partial pressure is low, which causes slower transportation of $CO_2$ out of the charge, and in turn slows down the transformation to c-LLZO. Thus, increased temperatures and reducing charge sizes reduces the amount of pyrochlore and increases the c-LLZO content [13].

**$Li_2CO_3$** is another typical intermediate phase that can occur. It can also be used as a precursor during synthesis, acting as the Li source. This is a very stable phase that can be formed if carbon containing species are present. The high stability of this phase makes it challenging, as it limits the Li accessible in the system and therefore hinders LLZO-formation. As mentioned previously, decomposition of $Li_2CO_3$ is required in order to form c-LLZO. This can be described by Equation 2.3. From here, $Li_2O$ can react with pyrochlore to form c-LLZO [63].

$$Li_2CO_3 \rightarrow Li_2O + CO_2 \tag{2.3}$$

Low $CO_2$-partial pressure at moderate temperatures causes slow decomposition kinetics and slow transportation of $CO_2$ out of the charge, impeding the formation of c-LLZO. To avoid $Li_2CO_3$, enough time to allow for sufficient $CO_2$-release or higher calcination temperatures should be implemented. Above the melting temperature (723 °C), the decomposition proceeds more rapidly as the $CO_2$ partial pressure continues to increase [13], [31], [64]. The formation of $Li_2CO_3$ can also be suppressed by minimizing exposure to air, or in other words avoiding unwanted reactions with humidity and $CO_2$ [65].

**$Li_2ZrO_3$** is another secondary phase that can occur in high Li-content systems, which is a common practice to compensate for Li-loss and to avoid formation of pyrochlore [31]. A study by Liu et al suggests that the dwelling time during sintering has an influence on whether $Li_2ZrO_3$ will be formed or not [66]. Results showed that pellets sintered at 1000 °C for 24 h gave single phase c-LLZO, while shorter times (9 h, 18 h) and longer times (36 h) results in a mixture of c-LLZO and $Li_2ZrO_3$. By controlling the dwelling time, it is possible to avoid the formation of this secondary phase. Though rarely mentioned in the literature, other potential intermediate phases could also occur in Li-rich LLZO systems. Based on the $Li_2O$-$ZrO_2$ phase diagram shown in Figure 2.5, potential phases include $Li_6Zr_2O_7$ and $Li_8ZrO_6$.

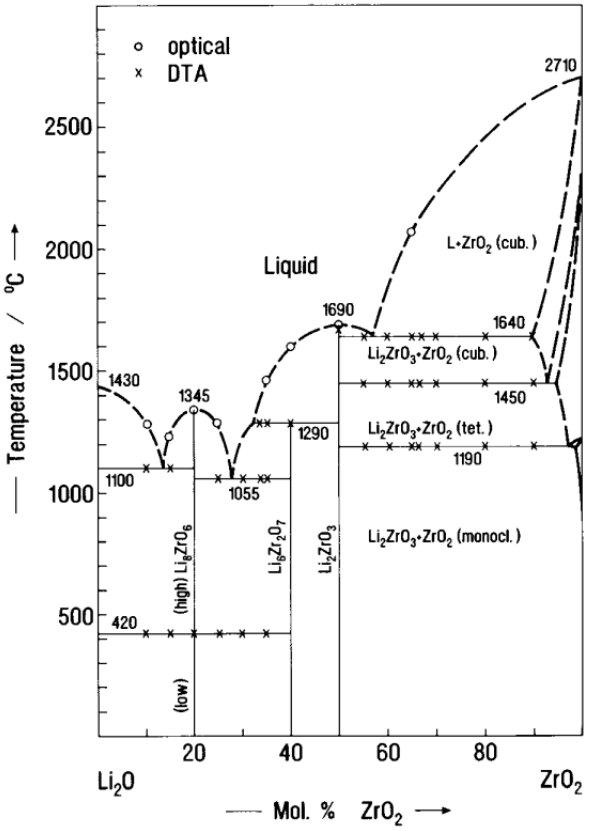


**Figure 2.5:** Phase diagram of the $Li_2O$-$ZrO_2$ system, adopted from Skokan [67]

**$LaAlO_3$** phase can occur for Al-doped LLZO systems if the Al-content exceeds the solubility limit of c-LLZO. Rangasamy et al. reports that formation of this secondary phase occurred for an Al-concentration of 0.389 mol [37]. This is in good agreement with the Al-concentration of 0.4 moles, as reported by Kumazai et al. [41]. The formation of this phase works as an additional contributor to further Li-loss. By lowering the Al-content, the amount of $LaAlO_3$ will be reduced.

**Li-Al-O** phases can also potentially occur in Al-doped LLZO systems. Formation of this phase works as a sintering aid, as the phase allows for heightened Li diffusion between LLZO grains. Sintering can thus be promoted, forming a densely sintered material [39]. As seen in the $Li_2O$-$Al_2O_3$ phase diagram in Figure 2.6, there is a eutectic melt at 1055 °C for mol % $Li_2O$ just above 20 mol %. This is below the most common sintering temperatures, making it contribute to promoted sintering activity via viscous flow.

**$Li_{0.5}Al_{0.5}La_2O_4$** is another intermediate phase that has been observed in the literature. The origin of this phase is not clear, but might be due to Li-loss at elevated temperatures and/or longer sintering durations [68]–[70]. Similarly, formation of $Li_{0.5}Al_{0.5}La_2O_4$ also occurs for systems with high excess Al-content. This occurs as Al substitutes on the Li-sites, causing a depletion of Li [71], [72].

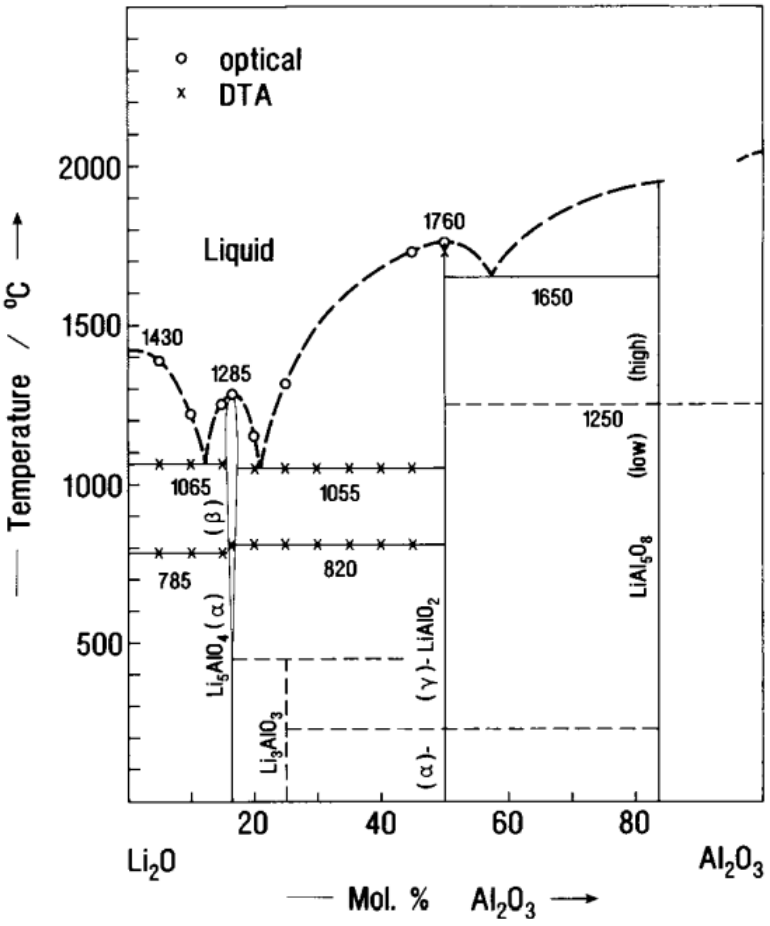


**Figure 2.6:** Phase diagram of the $Li_2O$-$Al_2O_3$ system, adopted from Skokan [67]

**$Li_4SiO_4$** have been reported to have beneficial effects on the density and total $Li^+$-conductivity of LALZO, when being used as a sintering additive. Additionally, the sintering temperature and sintering duration is reported to be reduced by the addition of this compound [73]. The melting temperature of $Li_4SiO_4$ is 1255 °C, which is close to conventional sintering temperatures used for LLZO-sintering. This allows for the formation of a liquid phase, enabling viscous flow sintering or liquid phase sintering, as opposed to solid state sintering. The result is a dense microstructure with small pores. At temperatures below the melting point, $Li_4SiO_4$ may also segregate to the grain boundaries without reducing the grain boundary conductivity. Furthermore, there is a possibility that $Si^{4+}$ replaces some of the $Al^{3+}/Li^+$ in the LALZO-lattice. This may result in extraction of $Al^{3+}/Li^+$, being extracted from the bulk to the grain boundary region. This forms favorable $Li^+$-conducting paths along the grain boundaries, such as Li-Al-Si-O and $LiAlSi_2O_6$. This, in combination with the now increased number of empty lattice sites, allows for enhanced conductivity [74]. $Li_4SiO_4$ is also intrinsically a $Li^+$-conductor, being among the top candidates among the lithium-silicates and alumino-silicates. This means that the presence of this phase will not negatively impact the total conductivity. Moreover, when being used in solid solutions with other compounds, further enhancements of the conductivity have been observed [75].

**Mg-based** phases are not well documented in the literature for the LLZO system. The most common observation is that a secondary phase of MgO in a LLZO/MgO composite system has been proved to control AGG, while still yielding a dense, highly conductive electrolyte material [54]–[57], [59]. Another scenario is that the $Mg^{2+}$ enters the LLZO lattice structure, which was the case when studying Al/Mg co-doped LLZO. This material also maintained high conductivity, in addition to long term air stability [76]. Another Mg-phase that might potentially occur is $MgAl_2O_4$ (spinel). As shown in the MgO-$Al_2O_3$ phase diagram, shown in Figure 2.7, spinel forms a broad solid solution area.

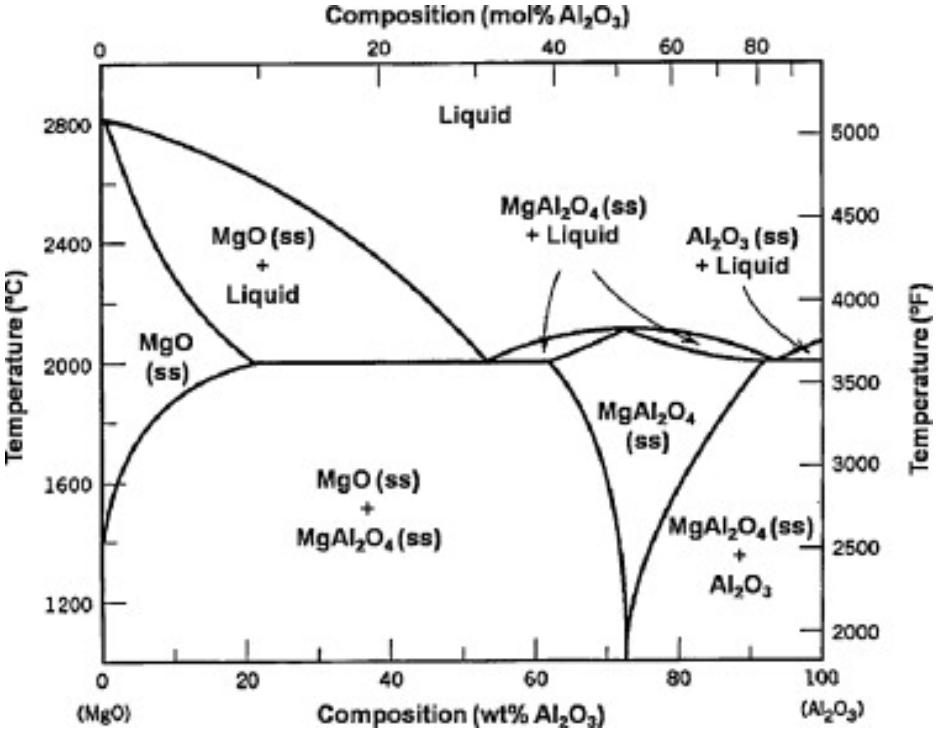


**Figure 2.7:** Phase diagram of the MgO-$Al_2O_3$ system, adopted from Braulio et al. [77]

## 2.4 Li loss and volatile lithium compounds

High Li-loss is linked to the use of high temperatures during calcination and sintering. Li-loss from the garnet phase can have multiple different origins, including formation of evaporated volatile lithium compounds (VLCs) and/or secondary phases. Various methods have been suggested to help minimize the Li-loss in LLZO. This includes altering the sintering techniques and -conditions. Examples of novel sintering methods include hot-pressing, field assisted sintering technique (FAST) and spark plasma sintering (SPS). The downside to these techniques is that they are quite expensive and challenging, due to the use of high pressures, in-situ heating and tightly closed chambers [78].

Another source of Li-loss comes from reactions with the crucible. One of the most commonly used crucible materials is $Al_2O_3$, which will react with Li-containing species such as LLZO. This introduces $Al^{3+}$, which will substitute with $Li^+$ and thus lower the Li-content. Ideally, inert

crucibles such as MgO or platinum should be used. Using MgO-crucibles will introduce some $Mg^{2+}$ to the system. $Mg^{2+}$ has also been found to give higher ionic conductivity at RT compared to $Al^{3+}$ [51], [79]. Moreover, bedpowders are commonly used when sintering LLZO samples. This has two main intentions: (i) Minimizing contact between the pellet and the crucible material, to avoid unwanted reactions with the crucible material and (ii) Provide additional Li to compensate for high-temperature Li-loss. If bedpowders are not implemented, inert crucibles should definitely be utilized [80].

The effect of VLCs in the LLZO system have been studied by Huang et al., who through a series of sintering experiments managed to capture VLC on an $Al_2O_3$ sheet. Despite the LLZO sample not being in direct contact with the $Al_2O_3$ sheet, XRD-analysis confirmed the presence of $LiAl_5O_8$ and $LiAlO_2$. These phases originate from VLC-gas that has formed during evaporation of the bedpowder. This effectively proves the existence of VLCs [81]. $Li_2O$ is another prevalent VLC, that has been studied by using a platinum Knudsen cell set-up connected to mass spectrometers. In this way, the partial pressure of solid $Li_2O$ could be determined. The equilibrium vapor pressures for a few different VLCs at various temperatures are listed in Table 2.2. As $Li_2O$(s) reacts, which is a prerequisite for the formation of LLZO, Li(g) or $Li_2O$(g) are likely the formed VLCs. Li(g) can generally be neglected, as it gets suppressed when sintering in an atmosphere with high oxygen partial pressures. That leaves $Li_2O$(g) as the main VLC-component for the LLZO system [81]–[83].

**Table 2.2:** Vapor pressure of VLCs, adopted from Kudo et al. [83]

| Temperature [°C] | Vapor pressure [atm] | | |
|---|---|---|---|
| | Li | LiO | $Li_2O$ |
| 1079 | $5.04 \times 10^{-7}$ | $9.93 \times 10^{-9}$ | $1.49 \times 10^{-7}$ |
| 1141 | $1.51 \times 10^{-6}$ | $1.04 \times 10^{-8}$ | $6.75 \times 10^{-7}$ |
| 1195 | $4.73 \times 10^{-6}$ | $4.30 \times 10^{-8}$ | $2.36 \times 10^{-6}$ |
| 1230 | $8.98 \times 10^{-6}$ | $8.84 \times 10^{-8}$ | $5.04 \times 10^{-6}$ |
| 1277 | $1.90 \times 10^{-5}$ | $2.22 \times 10^{-7}$ | $1.25 \times 10^{-5}$ |

## 2.5 $Li^+$-transport and -conductivity

One of the main aspects that contribute to the popularity of LLZO among the other solid electrolyte materials, is the high $Li^+$-conductivity. The extra Li atoms per formula unit causes a lattice distortion as Li-atoms are forced into interstitial positions. The increase in volume reduces the distance between Li-atoms and lowers the ionic interactions, resulting in enhanced $Li^+$-conductivity. The conductivity can also be increased further by optimizing synthesis conditions, sintering procedures or by implementing doping strategies [15], [16].

As previously mentioned, the cubic LLZO structure shows higher $Li^+$-conductivity compared to the tetragonal phase. One of the reasons for this is that the cubic phase displays short atomic displacement and isotropic $Li^+$ diffusion pathways, compared to the tetragonal phase which displays large atomic displacement and anisotropic pathways. This causes the cubic phase to have greater static disorder, unlike the Li-ordering of the tetragonal polymorph [15], [84].

Due to c-LLZO not being stable at RT, measures to ensure phase stability must be applied. Aliovalent doping of LLZO, where high valence cations are introduced to the LLZO, causes stabilization of the cubic structure. This is achieved via vacancy formation, which promotes $Li^+$ transport and allows for enhanced ionic conductivity. At the same time, the doping concentration cannot be too high as this causes destabilization of the cubic phase. Another negative effect is that doping can cause deactivated vacancies. This occurs when the Li-vacancies in close proximity feels the effect of the strong repulsions, making them less likely for $Li^+$-occupancy. This reduces the amount of accessible Li-vacancies. In other words, it is necessary to find suitable dopant amounts in order to fine-tune the quantity and quality of the Li-vacancies in the LLZO structure [85], [86]. Moreover, when doping with elements that leads to $Li^+$ substitution, the foreign element can hinder $Li^+$-motion by blocking the conduction pathways in the lattice. As a result, many studies have focused on substitution on sites that avoid the $Li^+$ conduction pathway. Substitution with dopants such as Ta and Nb on the Zr-sites makes in possible to avoid interference with the Li-sublattice, while still reducing the Li-content [87]. The La-site can also be doped, for instance with Rb, which was found to result in high conductivity as well. This is due to the larger Rb-cation radius compared to the La-cation, which enables more free space for $Li^+$ to migrate along the conduction pathways [19].

In addition to the doping concentration, the $Li^+$-concentration also directly influences the $Li^+$-transport. For cubic Li-garnets, with the stoichiometry $Li_xA_3B_2O_{12}$ (where A = $Y^{3+}$, $La^{3+}$, $Sr^{2+}$, $Ba^{2+}$; B = $Te^{6+}$, $Ta^{5+}$, $Zr^{4+}$; x = 3, 5, 6, 6.5, 7 and 7.5), an increase in $Li^+$-conductivity is observed with increasing x. A maximum is achieved for x = 7, followed by a reduced conductivity upon a further increase in x [88].

Table 2.3 lists a selection of total ionic conductivity values for LALZO, as described in the literature. Here, various synthesis methods and sintering conditions are taken into consideration. The general consensus is that LALZO can obtain conductivity values $> 10^{-4}$ S/cm.

Table 2.4 lists the highest achieved conductivities for LLZO systems where MgO have been added as a sintering additive. The various sample systems and sintering conditions are taken into consideration. The general consensus is that using MgO as a sintering additive generally does not reduce the ionic conductivity, even achieving values above what is reported for LALZO. It should be noted that the highest conductivities were obtained for LLZO doped with other elements than Al, which is expected to give higher conductivities.

**Table 2.3:** Total ionic conductivity ($\sigma_{tot}$) and relative density (RD) values of LALZO, as reported in the literature. SSR=Solid-state reaction, FS = Flash sintering, AAS=Ambient air sintering, HP = Hot pressing, SPS = Spark plasma sintering, FAST = Field assisted sintering technology.

| Synthesis method | Sintering conditions | RD [%] | $\sigma_{tot}$ [$\cdot 10^{-4}$ S/cm] | Source |
|---|---|---|---|---|
| SSR | FS, 1200 °C @ 3 h, 2.45 GHz | 89.3 | 1.06 (25 °C) | [89] |
| Sol-gel | AAS, 1200 °C @ 12 h | 79 | 1.1 (33 °C) | [74] |
| Sol-gel | AAS, 1230 °C @ 36 h | N/A | 1.4 (25 °C) | [90] |
| SSR | AAS, 1230 °C @ 6 h | 89.8 | 1.8 (RT) | [91] |
| SSR | AAS, 1230 °C @ 36 h | N/A | 2.0 (RT) | [92] |
| Pechini | AAS, 1200 °C @ 6 h | 86 | 2.0 (RT) | [35] |
| Co-precipitation | AAS, 1180 °C @ 20 h | >90 | 2.0 (30 °C) | [26] |
| SSR | AAS, 1300 °C @ 1 h | N/A | 2.1 (25 °C) | [25] |
| SSR | AAS, 900 °C @ 12 h | N/A | 2.11 (25 °C) | [93] |
| SSR | AAS, 1230 °C @ 36 h | N/A | 2.44 (25 °C) | [14] |
| SSR | ASS, 1200 °C @ 24 h | 93 | 2.48 (N/A) | [94] |
| Sol-gel | AAS, 1100 °C @ 15 h | 92.5 | 3.08 (20 °C) | [8] |
| Sol-gel | AAS, 1150 °C @ 1 h | N/A | 3,4 (25 °C) | [71] |
| SSR | HP, 1050 °C @ 4 h, 62 MPa | 98 | 3.4 (20 °C) | [95] |
| SSR | AAS, 1230 °C @ 36 h | N/A | 3.5 (25 °C) | [96] |
| SSR | ASS, 1230 °C @ 35 h | 96 | 3.6 (N/A) | [97] |
| SSR | HP, 1100 °C @ 1 h, 62 MPa | 99 | 3.7 (N/A) | [98] |
| SSR | HP, 1000 °C @ 1 h, 40 MPa | 98 | 4.0 (RT) | [37] |
| SSR | AAS, 1200 °C @ 24 h | 96 | 4.48 (N/A) | [34] |
| SSR | SPS/FAST, 1150 °C @ 3 min, 10 MPa | 99.8 | 5.7 (25 °C) | [99] |

**Table 2.4:** The highest total ionic conductivity ($\sigma_{tot}$) and relative density (RD) achieved for LLZO systems where MgO have been added as a sintering additive, as reported in the literature. Ar=Ar-filled atmosphere, AAS=Ambient air sintering and pfu = Per formula unit.

| Sample system | Sintering conditions | RD [%] | $\sigma_{tot}$ [$\cdot 10^{-4}$ S/cm] (MgO-content) | Source |
|---|---|---|---|---|
| Al-LLZO + MgO (sheet) | Ar, 1115 °C @ 3h | 87.7 | 4.2 (3 wt%) | [53] |
| Al-LLZO + MgO (pellet) | Ar, 1115 °C @ 7h | 88 | $<$ 0.4 (3 wt%) | [53] |
| Ta-LLZO/MgO composite | ASS, 1150 °C @ 5h | 98.2 | 5.17 (6 wt%) | [54] |
| Ta-LLZO/MgO composite | ASS, 1250 °C @ 10h | 98 | 5.7 (3 wt%) | [55] |
| Ta-LLZO/MgO composite | ASS, 1250 °C @ 40min | ∼95 | 3.5 (6 wt%) | [56] |
| Ta-LLZO/MgO composite | ASS, 1250 °C @ 1h | $>$97 | 7 (4 wt%) | [57] |
| Ta-LLZO/MgO composite | ASS, 1230 °C @ 1h | 97.89 | 7.76 (4 wt%) | [58] |
| Nb-LLZO/MgO composite | ASS, 1250 °C @ 40min | 97 | 6 (0.4 pfu) | [59] |

The ionic conductivity of a material is referring to the total ionic conductivity, $\sigma_{tot}$, of the material. This consists of contributions from the bulk and the grain boundaries, where the $Li^+$-transport is especially influenced by the grain boundary contributions. In general, grain boundaries can either suppress or enhance the ionic diffusion rates relative to the bulk diffusion. This depends on the material. For LLZO, high GB-resistance causes decreasing $Li^+$ conductivity. One way of reducing these GB-effects is producing a microstructure with larger grains, that is, a smaller volume fraction of GBs [100]. However, this will also lower the mechanical strength of the electrolyte material. Similarly, GB-resistance can be lowered by producing samples with high RD and tightly bound grains. For a microstructure with a high degree of porosity, $Li^+$-transport through the crystal structure is disturbed by the pores acting as physical barriers [98], [101]. Various strategies for increasing the RD and subsequently the $Li^+$-conductivity, will be discussed in Section 2.7.1.

Despite of LLZO having good electrochemical stability, there are some challenges regarding the electrolyte-electrode interfaces. Due to the solid nature of ceramics, achieving good contact with the electrodes in fully assembled batteries is difficult. This results in high interface resistance, which will influence the total resistance in the cell and the resulting $Li^+$-conductivity [102]. However, this is beyond the scope of this work and will not be further discussed.

## 2.6 Electrochemical impedance spectroscopy (EIS)

EIS is a non-destructive technique that is widely used to analyse the electrical properties and determine the ionic conductivity of solid electrolytes. Solid electrolytes are made out of ceramics, which are dielectric materials. This means that when applying a direct current (DC), charge

polarization will occur at the electrode-electrolyte interface and/or phase boundaries of the sample. In other words, dielectric materials are non-ideal resistors and does not obey Ohm's law. This means that the resistance of these materials cannot be measured by a traditional DC-method. The solution to avoiding this problem is by instead utilizing an alternating current (AC) and measuring the impedance. During EIS-analysis, small sinusoidal AC voltage impulses are applied over a wide frequency range (MHz to mHz). This induces a phase-shifted current response, where the impedance can be quantified based on this phase shift and its amplitude [103], [104]. The results of EIS-measurements give an indication of the overall resistance of the material and being able to identify and differentiate the bulk and grain boundary components. The results can also demonstrate the ceramic quality and electrical homogeneity [105].

Complex impedance plots, i.e., Nyquist plots, utilizes complex plane analysis to study the real and imaginary parts of the complex electrical quantities of a material. The impedance data is plotted in diagrams, where the imaginary part (Z") is plotted on the y-axis and the real part (Z') is plotted on the x-axis. This is visualized in the schematic shown in Figure 2.8. Data from the low frequency range are on the right side, while the high frequency data are on the left side. Each point represents the impedance at a certain frequency, described by a vector of length |Z|, alternating dependent on the frequency ($\omega$)/the angle ($\phi$) [106].

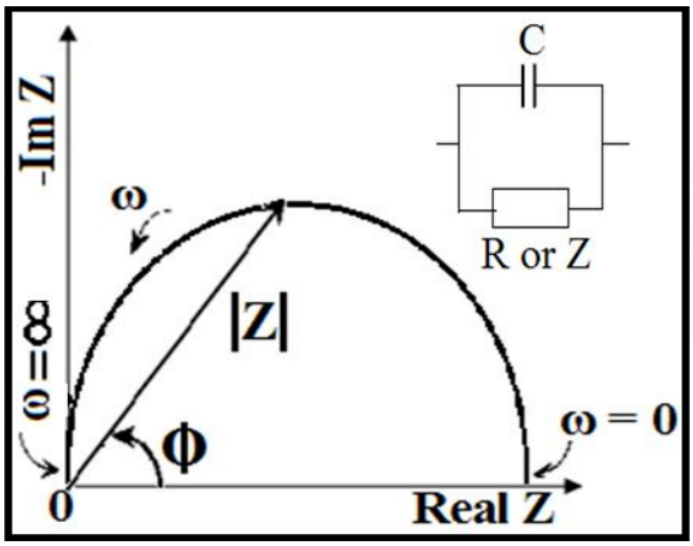


**Figure 2.8:** Schematic of a typical Nyquist plot. The inset shows a parallel R-C circuit. Adopted from Joshi [106].

The frequency-dependent AC impedance, $Z(\omega)$, can be described as a complex number, according to Equation 2.4 [107].

$$Z(\omega) = \frac{E}{I} = \frac{E_0 \exp(j\omega t)}{I_0 \exp(j\omega t - \phi)} = Z_0 \exp(j\phi) = Z_0(\cos\phi + j\sin\phi) \tag{2.4}$$

where $E$ is the potential signal, $I$ is the current response, $E_0$ is the potential amplitude, $I_0$ is the current amplitude, $j$ is a complex number, $\omega$ is the radial frequency, $t$ is the time, $\phi$ is phase shift and $Z_0$ is the impedance amplitude.

The impedance spectrum for a two-point blocking electrode-solid electrolyte set-up commonly display two distinct features, which can be attributed to intragrain (bulk) and intergrain (grain boundary) contributions. When the impedance data is plotted, each parallel RC-element results in a semicircle [105]. The AC-response for the bulk and grain boundary contributions is shown in Figure 2.9 [106]. An additional feature of these plots is an inclined spike/tail in the low frequency region. This spike is due to polarization of the blocking electrodes [105]. If the bulk and grain boundary contributions can not be separates, due to negligible grain boundary resistance, the Nyquist plots would consist of only one semicircle. Temperature dependent impedance measurements would allow for a more reliable separation of the ionic conductivity contribution from bulk and grain boundaries, respectively.

The contribution of the bulk and the grain boundaries can be modeled by implementing equivalent circuits, like the one shown in Figure 2.9. Depressed semicircles can be modeled by circuits with a resistor, R, and a constant phase element, Q, in parallel [103], [108]. The total (bulk + grain boundary) $Li^+$ conductivity can be calculated from the inverse of the resistivity, which is obtained from the point of intersection between the high frequency semicircle and the Z'-axis. The inclusion of the blocking electrolyte CPE|R parallel has no physical meaning, but allows for an enhanced fitting due to the blocking electrodes being non-ideal [109].

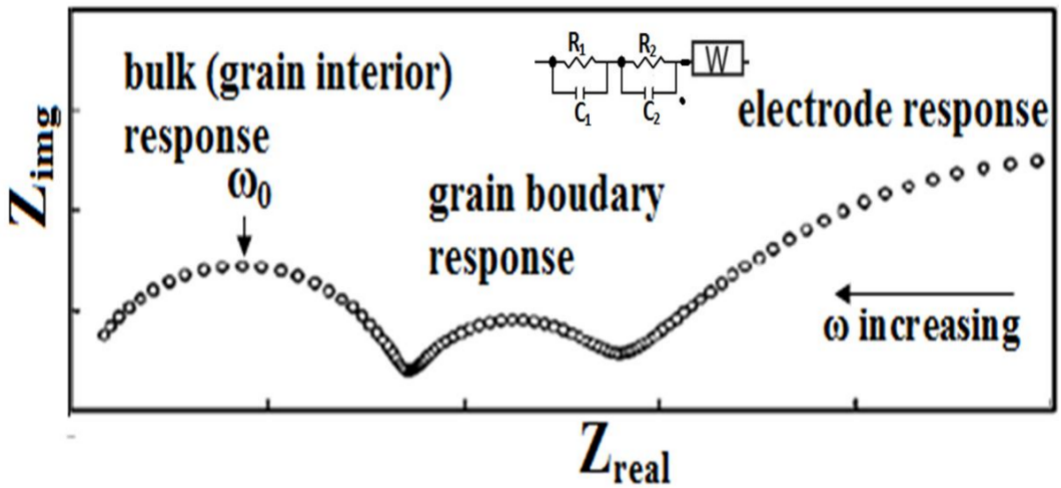


**Figure 2.9:** Schematic of bulk and grain boundary contributions in a typical Nyquist plot. The inset shows a parallel R-C circuit. Adopted from Joshi [106].

## 2.7 LLZO sintering

Sintering of LLZO is necessary in order to obtain a material that is suitable for electrolyte purposes. After sintering, the aim is to have produced a pure, single phase c-LLZO material with small, tightly bound grains. This is in order to allow for increased ionic conductivity, by minimizing the GB-resistance. Additionally, the porosity needs to be low, reaching relative densities close to the theoretical density. Having a high degree of porosity, with relative densities below 90%, would make the material prone to Li-metal dendrite growth [110]. High mechanical strength is a prerequisite to limit dendrite growth [111]. Acquiring pure, dense c-LLZO has proven to be quite challenging. This can mostly be attributed to Li, which is a highly volatile element. To avoid Li-loss and formation of unwanted intermediate phases during production, a sufficient Li-excess must be added and measures such as implementing bedpowders should be considered.

### 2.7.1 Strategies for increasing the RD of doped LLZO

Generally, densification is achieved by conventional sintering at high temperatures. However, this is associated with severe Li-loss, AGG and formation of t-LLZO. These topics have been subject to extensive research, focusing on alternative fabrication methods of dense LLZO materials. A selection of relative density values for LALZO sintered with various sintering techniques and LLZO systems where MgO have been added as a sintering aid are listed in Table 2.3 and Table 2.4, respectively.

The main approach is to make alterations to the sintering programs, in order to lower the sintering temperatures while still achieving c-LLZO. A possible option is to utilize rapid sintering at high temperatures (i.e., 1360 °C), reducing the sintering time significantly (10 min) while still achieving high densities (97 %) [112]. Furthermore, a dense microstructure and high RD-values are achievable by implementing a multi-step sintering strategy. RDs of 98 % were produced by a two-step sintering program, consisting of one short-time high-temperature step (1150 °C @ 1 min or 1250 °C @ 10 min) and one long-time low-temperature step (1000 °C @ 3 h or 1150° @ 5 h) [9], [113]. In addition to the conventional sintering techniques, several advanced sintering techniques have been found to successfully produce high density LLZO materials. Using such techniques helps avoid problems related to conventional sintering. Such techniques include: (i) Hot pressing [37], [95], [98], (ii) Microwave assisted sintering [89], [114], and (iii) Spark plasma sintering/field-assisted sintering [99].

There are also options regarding the quality of the precursor powder. For instance, powder agglomeration can be limited by freeze drying. This gives improved control of the microstructure, yielding LLZO with a low degree of porosity and high relative density (98 %) [115]. Another option is to utilize a composite system or implementing sintering additives, which can promote densification [54], [59]. Furthermore, the existence of VLCs have a strong influence on the final product. By

altering the amounts of bedpowder used and the degree of contact between the powder and the pellets, the VLC-vapor pressures and Li-loss can be controlled, and densification can be promoted [81]. The choice of crucible material has also been found to have a significant influence on the properties after sintering. When comparing alumina and platinum crucibles, the later was found to give the highest relative density, in addition to exhibiting higher ionic conductivities and greater air stability [34]. When utilizing inert crucibles, unintentional incorporation of Al or other dopants can be avoided, and Li-loss can be suppressed [34].

### 2.7.2 The influence of AGG

As discussed in Section 2.2.3, Al-doped LLZO is prone to AGG. Extensive grain growth of particular grains consumes smaller neighbouring grains. This results in growth of large grains, which negatively affects the desired properties of the electrolyte material. This includes high resistivity, and thus lowering the ionic conductivity. In addition, poor stability and low mechanical strength introduces the risk of Li-dendrite penetration and propagation. In order to achieve good ionic conductivity, high mechanical strength and high relative density, the microstructure should consist of small, tightly bound grains.

AGG can be avoided by lowering the sintering temperature and holding time, though this might reduce the degree of densification. The concentration of VLCs in the system also influences the degree of AGG. In atmospheres with higher vapor pressures of VLCs, more liquid materials are available and allows AGG to occur during prolonged sintering [8], [81]. Another option for avoiding AGG is by utilizing sintering inhibitors, co-doping or composite systems. Here, the formation and embedding of secondary phases between grains effectively hinders or reduces AGG. It is however very important that the presence of these secondary phases is small, as this can block the connection between the grains and negatively affect the ionic transport across the grains [54], [59], [113], [116].

Compared to conventional one-step sintering, utilizing a two-step sintering strategy has been found to avoid AGG. By shortening the time at higher temperatures and allowing for a longer secondary step at a lower temperature, serious overgrowth can be avoided while still allowing for sufficient densification [9], [113]. Comparable effects can also be seen for rapid sintering techniques. The short duration allows for rapid removal of impurities and fine control over the microstructure. After only a matter of minutes or seconds, a high density, uniform microstructure is achievable [112], [117].

# 3 Experimental

## 3.1 Chemicals and apparatus

A list of the chemicals used in this work is shown in Table 3.1, while information about the different apparatuses and crucibles are given in Table 3.2 and Table 3.3, respectively. A schematic of the different crucibles utilized in this work is shown in Figure 3.1.

**Table 3.1:** Chemicals utilized in this work

| Chemical | Formula | State | Manufacturer | Purity |
|---|---|---|---|---|
| Lithium nitrate | $LiNO_3$ | s | RodaChem | 99.0 % |
| Aluminium nitrate | $Al(NO_3)_3 \cdot 9\,H_2O$ | s | VWR Chemicals | 98.5 % |
| Lanthanum nitrate | $La(NO_3)_3 \cdot 6\,H_2O$ | s | Auer-Remy | $\geq$ 99.9 % |
| Zirconyl nitrate | $ZrO(NO_3)_2$ | aq | Lehmann& Voss | 99.9 % |
| Magnesium nitrate | $Mg(NO_3)_2 \cdot 4\,H_2O$ | aq | VWR Chemicals | Puriss PA |
| Ammonia solution | 25 % $NH_4OH$ | aq | VWR Chemicals | - |
| Ethanol | 96 % $C_2H_5OH$ | l | VWR Chemicals | $\geq$ 99.8 % |
| Isopropanol | $(CH_2)_2CHOH$ | l | VWR Chemicals | $\geq$ 99.7 % |
| Synthetic air | 80 % $N_2$ and 20 % $O_2$ | g | Linde Group | 5.0 |

**Table 3.2:** Apparatuses utilized in this work

| Apparatus | Manufacturer & model | Purpose |
|---|---|---|
| Furnace | Nabertherm P330 | Calcination and sintering |
| Ball mill | US Stoneware 764 AVM | Milling of powder |
| Rotavapor | Buchi R-210 | Solvent evaporation |
| CIP | Autoclave Engineers CIP | Increasing pellet density |
| Dilatometer | Netzsch DIL 402 C | Study sintering behavior |
| Diffractometer | Bruker D8 A25 DaVinci | Phase identification (XRD) |
| SEM | Zeiss Supra 55VP | Microstructural imaging |
| SEM | Zeiss Ultra 55 | Microstructure & elemental analysis (EDS) |
| Sputter coater | Edwards S150B | Deposition of Au-electrode |
| Potentiostat | Solartron ModuLab XM ECS | Ionic conductivity (EIS) |
| Polishing machine | Struers LaboPol-21 | Dry polishing |
| Polishing machine | Struers Tegramin-20 | Diamond suspension polishing |

**Table 3.3:** Crucibles utilized in this work.

| Crucible material | Configuration | $d_{inner}$ [mm] | $d_{outer}$ [mm] | Height [mm] |
|---|---|---|---|---|
| $Al_2O_3$ | Round | 32.68 | 36.72 | 49.86 |
| MgO | Square | 65.74 | 73.14 | 25.53 |

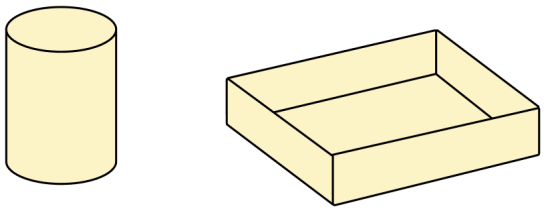

**Figure 3.1:** Schematic of the different crucibles utilized in this work, as referred to in Table 3.3. Left: $Al_2O_3$ and Right: MgO

## 3.2 Procedure

The different experimental procedures conducted during this thesis is shown in Figure 3.2.

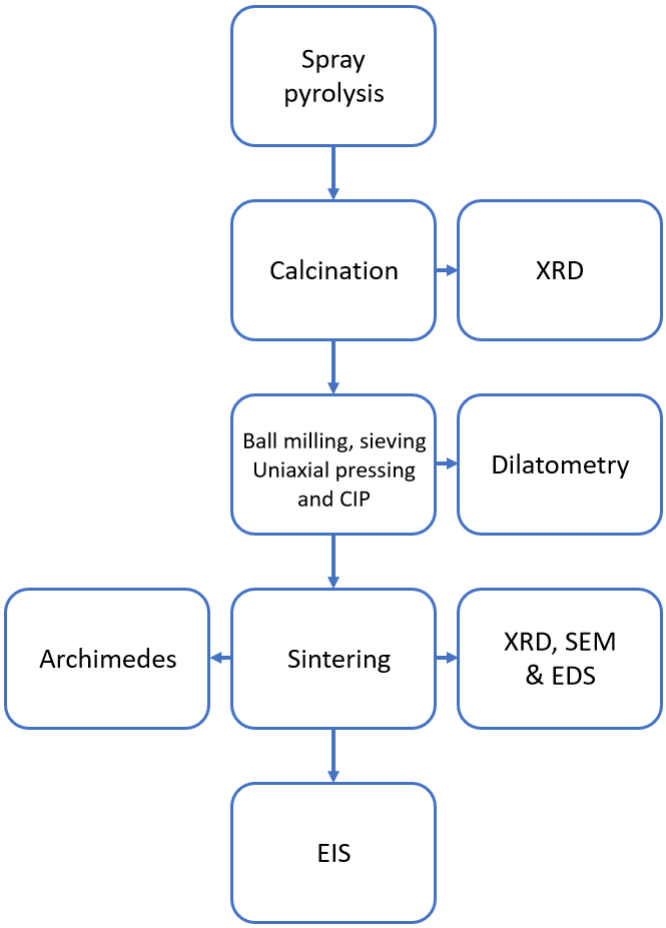


**Figure 3.2:** Flow chart of experimental procedures

### 3.2.1 Precursor powder preparation and spray pyrolysis

The precursor powders were synthesised at CerPoTech AS (Trondheim, Norway) via spray pyrolysis. Solutions consisting of nitrate-based compounds of all cations were prepared, giving the nominal stoichiometry $Li_{6.25}Al_{0.25}La_3Zr_2O_{12}$. An excess of Li corresponding to 24.2 mol% was added to compensate for Li-loss during synthesis and further processing. Lastly, varying amounts of $Mg(NO_3)_2$ was added in order to react and form MgO. The nomenclature for the different powders depending on MgO-content is given in Table 3.4 and will from now on be referred to by this terminology.

**Table 3.4:** Nomenclature for the precursor powders

| Nomenclature | MgO content [mol%] |
|---|---|
| 0 MgO – LALZO | 0 |
| 1 MgO – LALZO | 1 |
| 5 MgO – LALZO | 5 |

Organic complexing agents were then added, and ammonia was used to adjust the pH of the solution. After vigorous mixing, the solutions became transparent and was thus stable. The precursor solution was then spray pyrolyzed at 900 °C. Figure 3.3 shows a schematic of the setup for the spray pyrolysis at CerPoTech.

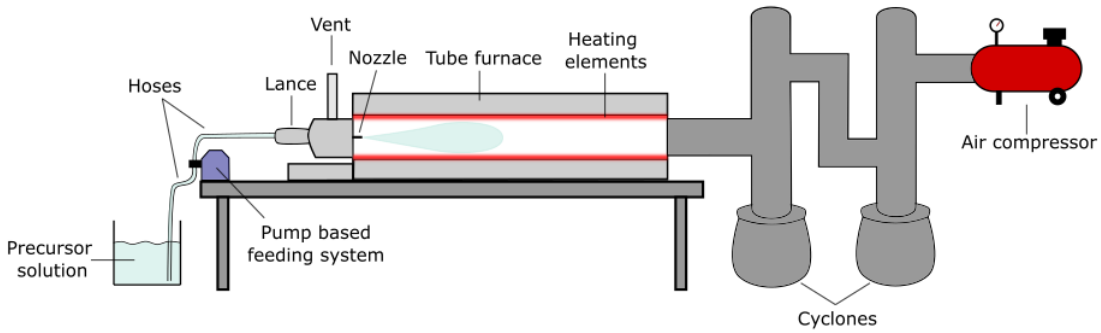


**Figure 3.3:** Schematic of the spray pyrolysis process

### 3.2.2 Calcination

Calcination of the precursor powders was conducted in order to promote reactions and remove volatile species. The powders were calcined in batch sizes of ∼4 g at 750 °C for 12 h, in ambient air using MgO-crucibles. Lids were also utilized to reduce contaminations, while leaving a small gap to allow release of gases produced during decomposition. A heating and cooling rate of 200 °C/h was chosen. The samples were removed from the furnace when the temperature had reached 200 °C and was left to cool in a desiccator.

After calcination, a ball mill was used to break up agglomerates and to reduce particle size of the powders. 100 mL of yttria-stabilized zirconia balls with $d = 5$ mm was used as the grinding media, which was added with 75 mL isopropanol solvent to 250 mL flasks with $d = 6$ cm. The rotation speed was set to 100 rpm. The powders were milled for 24 h and was then transferred to a rotavapor to evaporate the isopropanol. The powders were heated on a heating plate at 50 °C in order to remove any residual isopropanol, before being gently ground using a pestle and agate mortar to break up the soft agglomerates. Finally, the powders were sieved using a 250 $\mu$m grit sieve, producing a very fine powder and a narrow particle size distribution.

Bedpowders used for the sintering experiments were calcined at 800 °C for 12 h in MgO-crucibles. This temperature was chosen to achieve t-LALZO, which will provide additional Li to compensate for Li-loss. The 0 MgO – LALZO stoichiometry was chosen for the bedpowders, in order to avoid Mg-contamination of the Mg-free samples.

### 3.2.3 Dilatometry

Prior to the dilatometry experiments, pellets needed to be produced. Powders were calcined at 750 °C for 6 h using $Al_2O_3$-crucibles and samples were pressed into pellets using a double action uniaxial press. The diameter was set to 5 mm and the pellet mass ∼250 mg. A pressing force of 4 kN (204 MPa) was utilized. Thereafter, cold isostatic pressing (CIP) was applied in order to further enhance the green body density. The pellets were subjected to a hydrostatic pressure of 2 kbar, using a holding time of 1 min.

Dilatometry experiments were performed in order to study the sintering behavior of LALZO, by measuring the thermal expansion when exposed to sintering temperatures. The components in the dilatometer were made of $Al_2O_3$, so platinum foil was used in order to evade any reactions with the LALZO samples. An illustration of the experimental setup is shown in Figure 3.4. The heating program consisted of heating from RT to 1250 °C, using a heating rate of 120 °C/h. This temperature was then held for 1 h, before being cooled down to RT again using the same cooling rate. The samples were subjected to a synthetic air atmosphere, using a gas flow rate of 30 mL/min.

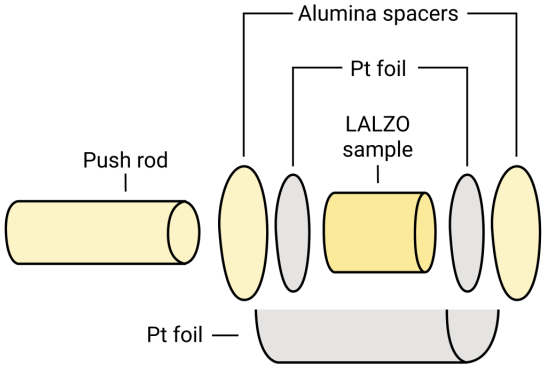


**Figure 3.4:** Schematic of the different components in the dilatometry setup

### 3.2.4 Sintering

The powders were calcined at 750 °C for 12 h in MgO-crucibles and further processed as described in Section 3.2.2. The calcined powders were then pressed into pellets using a double action uniaxial press, using a pressing force of 15 kN (191 MPa). The diameter of the pellets was chosen to be 10 mm and the pellet masses were approximately 600 mg. The pellets were then subsequently subjected to isostatic pressing, as described in Section 3.2.3.

Sintering was conducted in order to further increase the density and reduce the degree of porosity, forming a dense, solid material. In this work, ambient air sintering was carried out at 1150 °C and 1200 °C, using a heating and cooling rate of 200 °C/h. The pellets were sintered for either 1 h or 6 h, before being taken out of the furnace at 200 °C to be left to cool in a desiccator. Measurements of pellet mass, diameter and thickness were carried out prior to and after sintering. These values, in addition to the initial and final densities are listed in Table A.1. Bedpowders were implemented, in order to minimize contact with the crucible material, avoid unwanted reactions and to suppress Li-loss. The bedpowder ratio (BP-ratio) describes the mass of the pellet vs. the mass of the bedpowder. For BP-ratio = 0.5, only the bottom of the pellet was covered with bed powder, while for BP-ratio = 2 the pellet was completely covered in bed powder. This is also illustrated in Figure 3.5.

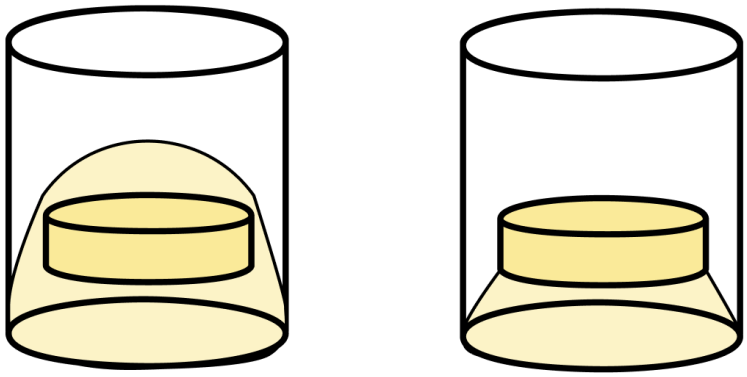

**Figure 3.5:** Schematic of the different BP-ratios implemented during sintering. On the left: BP-ratio = 2. On the right: BP-ratio = 0.5

Different crucibles were utilized, depending on the sintering program. The different crucibles are described in Table 3.3 and illustrated in Figure 3.1. To avoid contamination, lids fully covering the crucibles were used. This was done in order to preserve any Li-vapor in the crucible. All the sintering programs performed in this work, with their respective parameters, are described in Table 3.5.

**Table 3.5:** Sintering programs used in this work. $T_H$ = Sintering temperature, $t_H$ = Sintering time, BP-ratio = Bedpowder ratio, Crucible = As described in Table 3.3.

| Experiment | Nomenclature | Sample | $T_H$ [°C] | $t_H$ [h] | BP-ratio | Crucible |
|---|---|---|---|---|---|---|
| Preliminary sintering | P-1150 °C@1h/M | 0 MgO – LALZO | 1150 | 1 | 0.5 | MgO |
| | | 1 MgO – LALZO | 1150 | 1 | 0.5 | MgO |
| | | 5 MgO – LALZO | 1150 | 1 | 0.5 | MgO |
| | P-1200 °C@1h/M | 0 MgO – LALZO | 1200 | 1 | 0.5 | MgO |
| | | 1 MgO – LALZO | 1200 | 1 | 0.5 | MgO |
| | | 5 MgO – LALZO | 1200 | 1 | 0.5 | MgO |
| | P-1150 °C@1h/A | 0 MgO – LALZO | 1150 | 1 | 2 | $Al_2O_3$ |
| | | 1 MgO – LALZO | 1150 | 1 | 2 | $Al_2O_3$ |
| | | 5 MgO – LALZO | 1150 | 1 | 2 | $Al_2O_3$ |
| | P-1150 °C@6h/A | 0 MgO – LALZO | 1150 | 6 | 2 | $Al_2O_3$ |
| | | 1 MgO – LALZO | 1150 | 6 | 2 | $Al_2O_3$ |
| | | 5 MgO – LALZO | 1150 | 6 | 2 | $Al_2O_3$ |
| Main sintering | M-1150 °C@1h/M | 0 MgO – LALZO | 1150 | 1 | 2 | MgO |
| | | 1 MgO – LALZO | 1150 | 1 | 2 | MgO |
| | | 5 MgO – LALZO | 1150 | 1 | 2 | MgO |
| | M-1150 °C@6h/M | 0 MgO – LALZO | 1150 | 6 | 2 | MgO |
| | | 1 MgO – LALZO | 1150 | 6 | 2 | MgO |
| | | 5 MgO – LALZO | 1150 | 6 | 2 | MgO |
| EIS samples | E-1150 °C@1h/M | 0 MgO – LALZO | 1150 | 1 | 2 | MgO |
| | | 1 MgO – LALZO | 1150 | 1 | 2 | MgO |
| | | 5 MgO – LALZO | 1150 | 1 | 2 | MgO |
| | E-1150 °C@6h/M | 0 MgO – LALZO | 1150 | 6 | 2 | MgO |
| | | 1 MgO – LALZO | 1150 | 6 | 2 | MgO |
| | | 5 MgO – LALZO | 1150 | 6 | 2 | MgO |

### 3.2.5 Density measurements using Archimedes' method

The bulk density of sintered pellets was determined using Archimedes' method. The dry pellet masses were measured, before placing them in an evaporation dish inside a vacuum desiccator. A vacuum was then introduced in order to remove air from the pores, before the immersion liquid (Here: isopropanol) was progressively introduced to the desiccator. When the pellets were covered with a few cm of liquid, vacuum was reintroduced and sufficient time was allowed to ensure that the isopropanol penetrated into all the open pores. Air was then carefully introduced and the pellets were left to cool at ambient pressure. The evaporation dish was then transferred to a

balance, mounted with a loading pan. The pellet mass, while submerged in isopropanol, was then measured. Lastly, a damp tissue was used to remove any isopropanol on the pellet surface, before immediately measuring the wet pellet weight. All related weights, in addition to the solvent temperatures and the calculated bulk- and relative densities are listed in Table A.2.

### 3.2.6 X-ray diffraction

The phase composition of the LALZO samples were characterized via XRD-analysis, using a diffractometer with Bragg-Brentano geometry. The radiation source was Cu K$\alpha$ with wavelength $\lambda$ = 1.5406 Å, with a collection range of $2\theta \in [15°, 75°]$. Samples were analyzed in ambient conditions, where variable slits were used. Powder samples were analyzed by making a suspension of small amounts of the powder and isopropanol, before dripping some of the suspension on a flat Si-disk. Once the suspension had dried, a thin powder film was left on the surface. Pellet samples were analysed using deep holders, by placing the pellets on top of plasticine to create a leveled plane. Both the "as received" (pristine) surfaces and polished surfaces were studied. Additional XRD-parameters are listed in Table 3.6.

**Table 3.6:** XRD parameters for the different sample types

| Sample | Collection time [min] | Step size [°] | Scan rate [s] | Type of sample holder |
|---|---|---|---|---|
| Calcined powders | 60 | 0.0133 | 0.399 | Si-flat holder + Kapton film |
| Sintered pellets | 60 | 0.0133 | 0.399 | Deep holder + plasticine |

Indexing of the diffraction patterns was done using the DIFFRAC.EVA V5.2 (Bruker AXS) software, while the reference patterns used for phase identification were collected from the 2021 ICDD PDF-4+ database [118]. The relevant reference patterns for this work are listed in Table 3.7. The K$\alpha$2 contribution was stripped from the diffraction patterns, before extracting the data from the EVA-software. The diffraction patterns illustrated in this work were plotted using Python 3.7.3. Quantitative phase analysis and determining the lattice parameter for c-LALZO was done via Rietveld refinement, using the TOPAS V5.0 (Bruker AXS) software. This analysis was based on the same reference patterns as previously mentioned. The analysis also gives a value called $R_{wp}$, which gives an indication of how well the simulated patterns matches the experimental data [119].

**Table 3.7:** PDF-4+ cards for identified phases

| Phase | Formula unit | PDF-4+ card number |
|---|---|---|
| c-LALZO | $Li_{6.25}La_3Zr_2Al_{0.25}O_{12}$ | 04-023-8443 |
| t-LLZO | $Li_7La_3Zr_2O_{12}$ | 00-064-0140 |
| Pyrochlore | $La_2Zr_2O_7$ | 01-070-5602 |
| $Li_2CO_3$ | $Li_2CO_3$ | 00-022-1141 |
| LALO | $Li_{0.5}Al_{0.5}La_2O_4$ | 00-040-1167 |
| $Li_4SiO_4$ | $Li_4SiO_4$ | 01-084-7600 |

### 3.2.7 Scanning electron microscopy and elemental analysis

The microstructure of "as received" (pristine) surfaces, polished surfaces and pristine fracture surfaces of sintered pellets was studied by SEM. Imaging was done using both secondary electrons (SE) and backscattered electrons (BSE), with a 10kV accelerating voltage, a 30 $\mu$m aperture and a $\sim$10 mm working distance. The pellets were coated with carbon in order to provide conductivity and minimize charging.

In addition, EDS mapping was conducted on selected samples. The cross section of fractured samples were casted in epoxy resin and was polished by hand using SiC-sandpaper (European grit #800-#4000) and using a polishing machine with diamond suspensions (DiaPro Mol3, 3 $\mu$m and DiaPro NapB1, 1 $\mu$m). Then, the epoxy was covered with Al-foil and a carbon tape was the attached to both the sample and the foil in order to allow for electronic conduction. Finally, the samples were carbon coated and placed in a heating cabinet (60 °C) overnight to remove any moisture. Imaging was done using SE, using a 120 $\mu$m aperture and a $\sim$10 mm working distance. The accelerating voltage was set to 21 kV, which is sufficient to produce characteristic K$\alpha$ or L$\alpha$ X-rays.

### 3.2.8 Electrochemical impedance spectroscopy

The ionic conductivity of the sintered LALZO-samples was determined using EIS. Both the top and bottom of the pellets were wet polished by hand, using SiC-sandpaper (European grit (#800-#4000) and isopropanol. The polished surfaces were then sputter coated with Au, acting as the blocking electrodes. A schematic of the experimental setup of a pellet is shown in Figure 3.6. Approximate dimensions are included in the sketch, though minor varieties occurred.

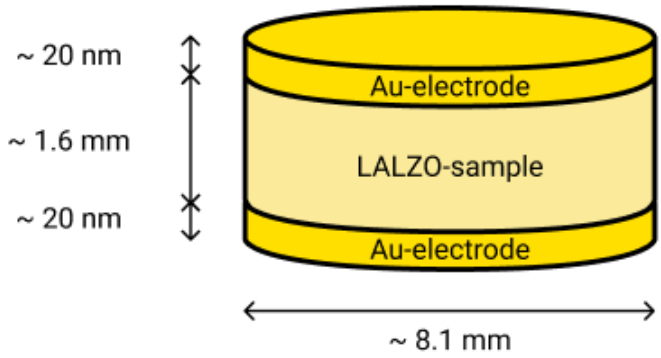


**Figure 3.6:** Schematic of experimental set-up of the pellet samples used for EIS. Approximate sample dimensions are given. The figure is not to scale.

The impedance of the samples was in a two-electrode set-up, using a frequency range of 1 MHz-100 mHz and a sinusoidal voltage amplitude of 10 mV. Measurements were conducted at RT. The experimental data was fitted with one of the equivalent circuits shown in Figure 3.7, using the XM studio ECS software.

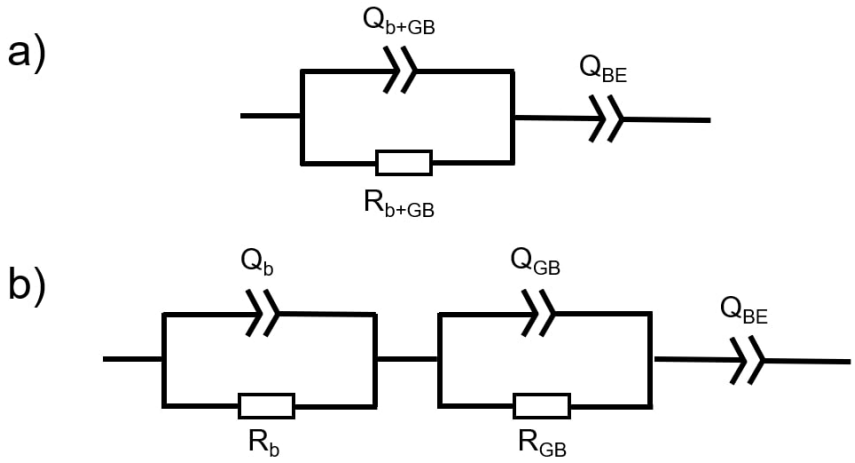


**Figure 3.7:** The two different equivalent circuits used for fitting of the experimental impedance results in the Nyquist diagrams. a) Applicable for samples where the bulk- and grain boundary contributions are non-separable. b) Applicable for samples with separable bulk- and grain boundary contributions. R = Resistor, Q = Constant phase element, b = Bulk, GB = Grain boundary and BE = Blocking electrode.

The resulting fit was then used to determine the resistance of the samples. In Figure 3.7a), the model corresponds to the total bulk + grain boundary response, as illustrated by one resistance ($R_{b+GB}$) and constant phase element ($R_{b+GB}$) in parallel. This is valid for Nyquist pots with only one semicircle. In Figure 3.7b), the bulk contribution ($R_b$) and the grain boundary contribution ($R_{GB}$) have been separated, as illustrated by two parallels. This is valid for Nyquist plots with two separable semicircles. The last RQ-parallel represents the contribution from the Au-electrodes and is valid for both models.

# 4 Results

This section includes the most noteworthy results from this work. This includes evaluation of phase composition via X-ray diffractograms and elemental quantification, study of microstructure via SEM micrographs, assessment of the densification occurring during sintering, and finally an estimation of the ionic conductivity via EIS-measurements. Other relevant results are provided in the Appendix.

All precursor powders utilized in this work were produced by spray pyrolysis, during the specialization project by Nybrodahl [13]. The diffraction patterns for the different precursor powders are shown in Figure B.1. The crystalline phases were identified and indexed, and are indicated with vertical lines in the plot. This also applies for all diffraction patterns in this work. As evident from the plot, the precursor powders consist of a mixture of c-LALZO, pyrochlore and $Li_2CO_3$.

## 4.1 Calcinations

In this work, one of the factors that was studied was the utilization of MgO-crucibles when calcining. Both the material and the dimensions of the crucibles differ from what was previously used in the specialization project by Nybrodahl [13]. A comparison of the phase purity of calcined powders using both $Al_2O_3$-crucibles and MgO-crucibles was therefore required. The choice of the calcination temperature of 750 °C was based on the calcination study from the same project [13]. As shown in Figure B.2, calcination at 750 °C for 6 h resulted in a single-phase c-LALZO powder for all the powder stoichiometries. To account for the different crucible dimensions and batch sizes, two different calcination holding times were tested. The diffraction patterns from these experiments are shown in Figure B.3. The results indicate that a duration of 6 h is sufficient for producing single-phase c-LALZO and avoiding intermediate phases when using the $Al_2O_3$-crucible. Meanwhile, the MgO-crucible requires 12 h. In this work, the MgO-crucible was chosen to be used for the calcination and sintering experiments. The main motivation for this is that MgO is inert with respect to Li, meaning no reactions with the crucible material is expected, as opposed to $Al_2O_3$. An additional benefit of the MgO-crucibles is the size (Table 3.3), meaning that larger batch sizes can be calcined.

Figure 4.1 shows the diffraction patters for ∼4 g of the various powder compositions calcined at 750 °C for 12 h in MgO-crucibles. All powders consist of single phase c-LALZO and no intermediate phases can be detected. No peak splitting can be observed, meaning no t-LALZO is present. The reference patterns for t-LALZO have been left out from the XRD-patterns, in order to increase the readability and applies for all coming diffraction plots in this work.

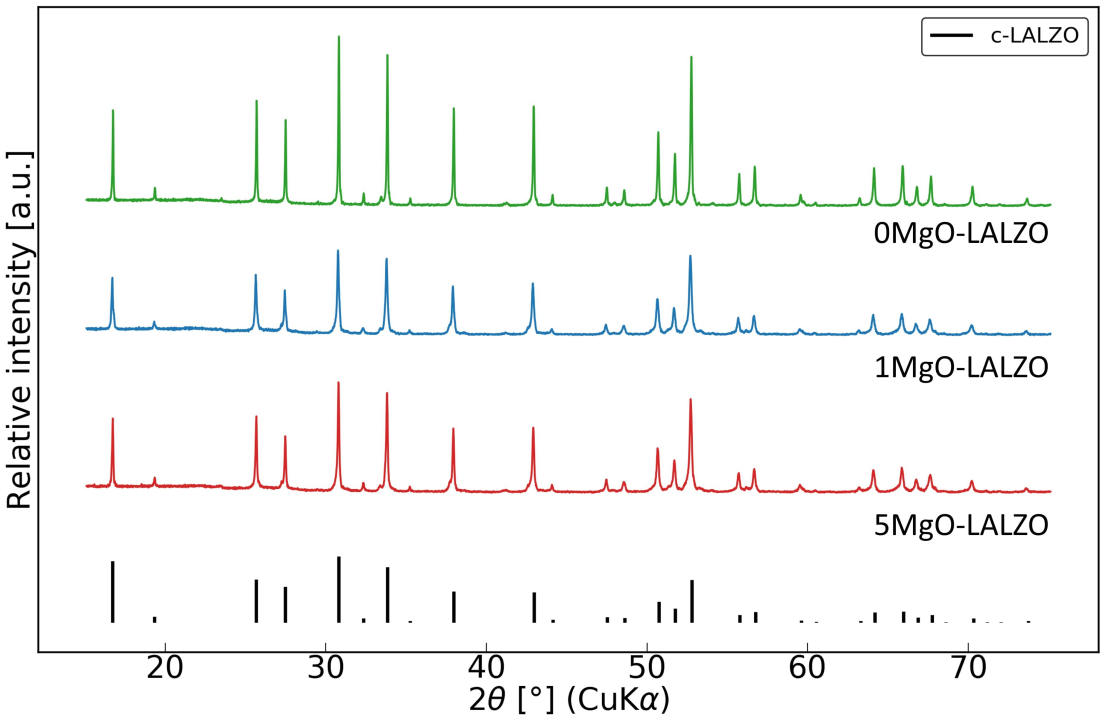


**Figure 4.1:** Diffraction patterns of MgO-added LALZO powders calcined at 750 °C for 12 h, using MgO-crucibles. All peaks belong to c-LALZO and no intermediate phases can be detected, indicating a single phase c-LALZO powder.

Bedpowders used for the sintering experiments were calcined at 800 °C for 12 h in MgO-crucibles, in batch sizes of ∼4 g. A diffraction pattern is shown in Figure B.4 and is representative for all batches produced in this work. The pattern shows that the bedpowder consists of a mixture of c-LALZO and t-LALZO. This was the goal, as this will provide sufficient excess Li in order to limit Li-loss during sintering.

## 4.2 Dilatometry and densification behavior

Figure 4.2 shows the dilatometry curves, displaying the change in the length of the LALZO pellets as a function of temperature and followed by a 1 h isothermal step at 1250 °C. The three different stoichiometries show similar densification behaviors in the early stages, before they deviate from each other. While 0 MgO – LALZO undergoes two separate densification steps, 1 MgO – LALZO and 5 MgO – LALZO undergoes three steps. The primary densification takes place in the second step, which occurs at approximately 1150 °C. This was therefore chosen to be optimal sintering temperature for this work. When approaching the isothermal step, densification of 0 MgO – LALZO stagnates while 1 MgO – LALZO and 5 MgO – LALZO continues to densify. 1 MgO – LALZO shows the lowest densification after sintering, while 0 MgO – LALZO and 5 MgO – LALZO show higher and similar densifications.

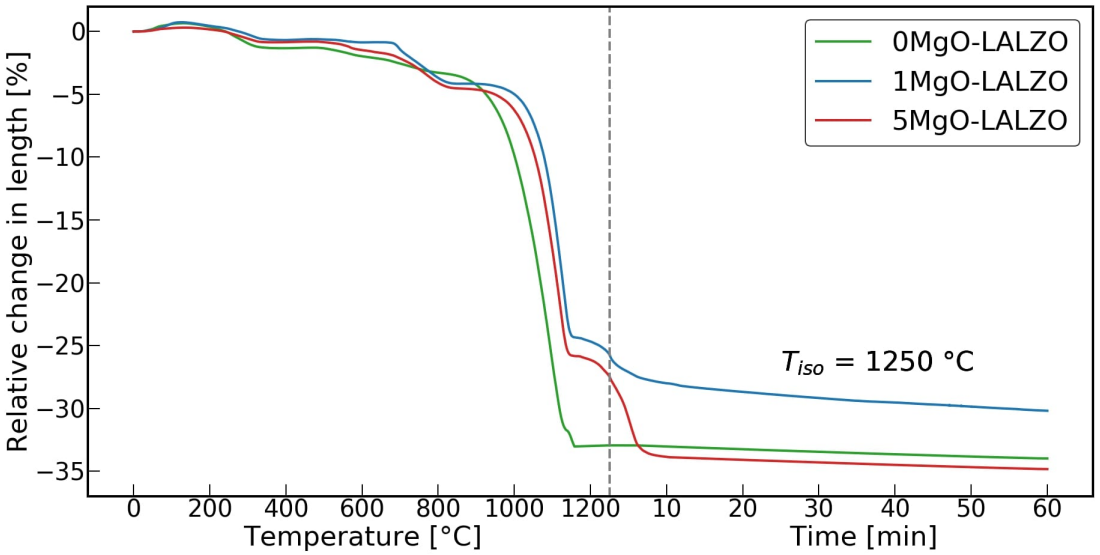


**Figure 4.2:** Comparison of the dilatometry sintering profiles of synthetic air-sintered pellets. The program consisted of dynamic heating to 1250 °C, followed by a 1 h isothermal step.

An overview of the phase purity of both the calcined powders used to produce the pellets prior to the dilatometry experiments, and the pellets after sintering is shown in Figure B.5 and Figure B.6, respectively. Despite having near phase pure c-LALZO (some t-LALZO) calcined precursors prior to the dilatometry experiments, the final pellet composition suffers from severe pyrochlore formation. This is the case both on the surface and in the center of the pellets. The pellets also got discolored after sintering, having red-brown dots across the entire surface of the pellets.

## 4.3 Preliminary sintering experiments

A preliminary sintering study was conducted in order to test out various variables like sintering temperature, sintering holding time, BP-ratio and crucible material. The diffraction patterns from the different sintering programs are summarized in Appendix C. The experiments revealed that using a BP-ratio=0.5 resulted in severe Li-loss and residual pyrochlore in the samples after sintering. This was also confirmed by backscatter electron imaging of polished pellet surfaces, as shown in Figure C.5. Furthermore, a sintering temperature of 1200 °C resulted in the formation of a few large grains in the samples, as evident from the SEM micrographs shown in Figure C.6 and Figure C.7a. The contrast between the "as received" surfaces and the cross-sectional fracture surfaces is shown in Figure C.8. Since it is desirable to avoid AGG, this sintering temperature proved to be non-ideal. Lastly, sintering experiments done using $Al_2O_3$-crucibles yielded a near phase pure c-LALZO material. This applies for both 1 h and 6 h sintering holding times. Using an inert crucible material, like MgO, would however be preferable in order to avoid any potential contamination of the pellets. Thus, the sintering programs selected for the main sintering study include sintering for 1 h and 6 h at 1150 °C, using a BP-ratio = 2 and MgO-crucibles.

## 4.4 Main sintering experiments

### 4.4.1 Sintered pellet densities

Figure 4.3 shows the relative density of the samples sintered during the main sintering experiments, based on measurements using Archimedes' method. The pellet masses, dimensions and densities of the green pellets and the sintered pellets are given in Table A.1. The weight measurements obtained during Archimedes' method and the calculated relative densities are given in Table A.2. The theoretical densities of each pellet composition was calculated based on the powder stoichiometries, as described in Appendix A. The estimated values of the theoretical densities of 0 MgO–LALZO, 1 MgO–LALZO and 5 MgO–LALZO are 5.130 g/cm$^3$, 5.166 g/cm$^3$ and 5.314 g/cm$^3$, respectively.

There seems to be no clear correlation between the Mg-content and the relative density within each sintering program. When the sintering duration is increased from 1 h to 6 h, the relative density of the 0 MgO–LALZO sample increases, while the density of 1 MgO–LALZO and 5 MgO–LALZO samples decreases. All densities are >85 %, indicating that there is still a significant degree of porosity present.

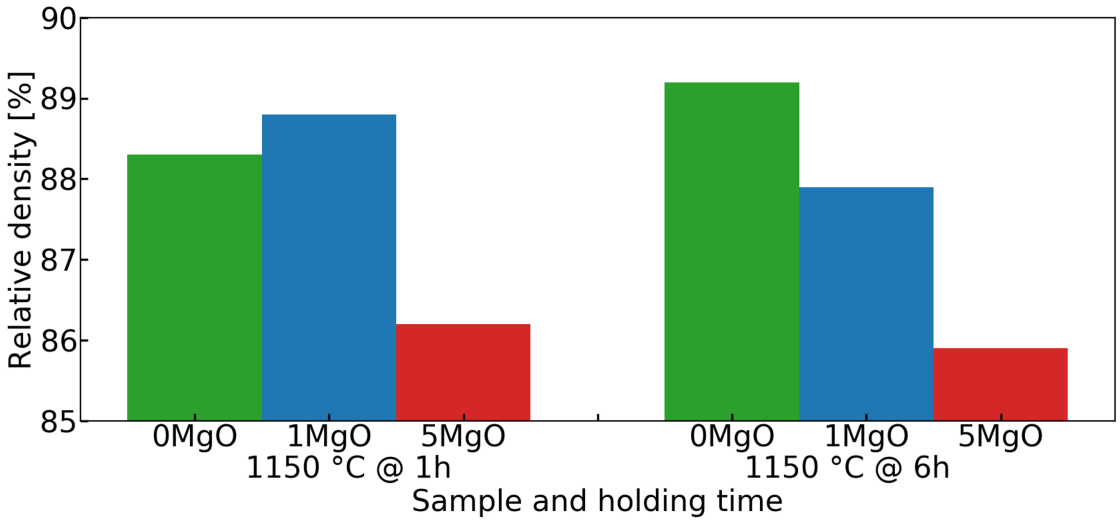


**Figure 4.3:** Histogram displaying the relative density of pellets sintered at 1150 °C for 1 h (M-1150 °C@1h/M, left) and at 1150 °C for 6 h (M-1150 °C@6h/M, right). The densities were measured using Archimedes' method. The theoretical densities of 0 MgO–LALZO, 1 MgO–LALZO and 5 MgO–LALZO are 5.130 g/cm$^3$, 5.166 g/cm$^3$ and 5.314 g/cm$^3$, respectively.

### 4.4.2 Phase composition of sintered samples

Figure 4.4 shows the diffraction patterns of the samples sintered at 1150 °C for 1 h (M-1150 °C@1h/M). All main peaks, for all three patterns, belong to c-LALZO. In addition, some low intensity peaks can observed and was indexed to be: $Li_4SiO_4$ and $Li_{0.5}Al_{0.5}La_2O_4$ (LALO). Figure B.7 shows the diffraction patterns, where a magnified section around some of the main peaks for $Li_4SiO_4$ and

LALO is shown in the inset on the right. No Si-containing species were included in the synthesis of the precursor powders and none were observed during the calcinations. This phase can therefore be termed an "impurity phase" and will from now on be referred to as such. The LALO-phase will be classified as an "intermediate phase". Figure B.9 shows a comparison of the diffraction patterns of the "as received" and polished surfaces of the sintered 5 MgO – LALZO-samples. The observation of a decreasing peak intensity of both $Li_4SiO_4$ and LALO upon polishing, alludes to these phases being surface effects.

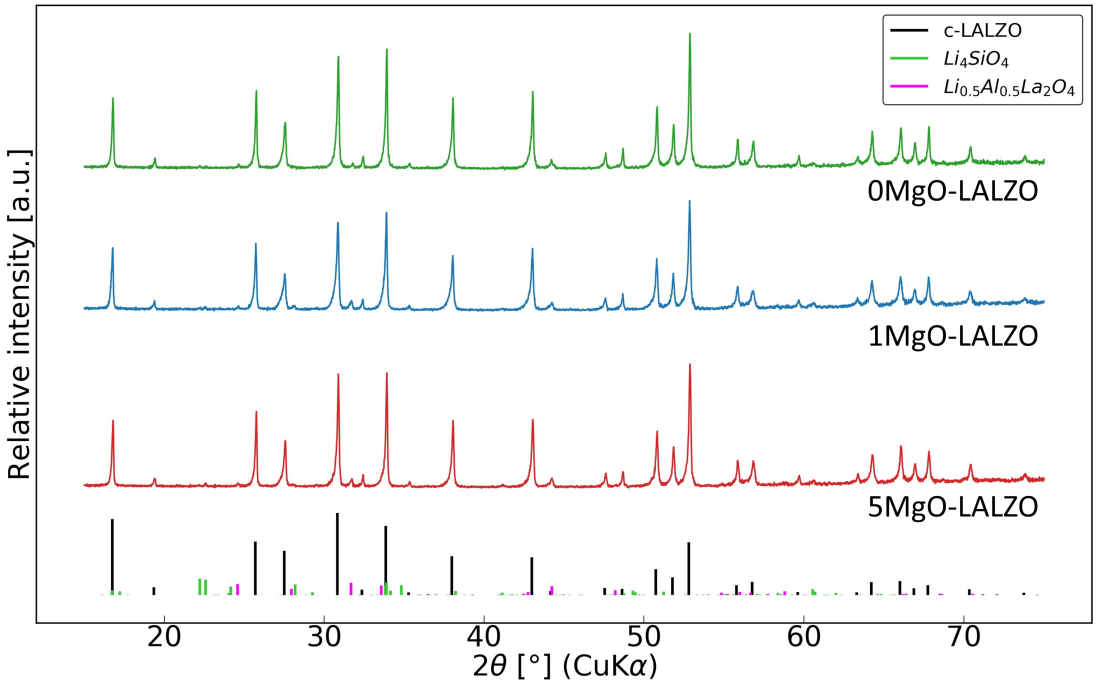


**Figure 4.4:** Bulk representative diffractograms of the samples sintered at 1150 °C for 1 h (M-1150 °C@1h/M). The main peaks are indexed to c-LALZO, in addition to some low-intensity peaks belonging to the $Li_4SiO_4$-impurity phase and the LALO-intermediate phase.

Figure 4.5 shows the diffraction patterns of the samples sintered at 1150 °C for 6 h (M-1150 °C@6h/M). Similar to the program with a 1 h-duration, all main peaks belong to c-LALZO, as well as some small amounts of the $Li_4SiO_4$-impurity phase and the LALO-intermediate phase. Figure B.8 shows the diffraction patterns, where a magnified section around some of the main peaks for $Li_4SiO_4$ and LALO is shown in the inset on the right. Furthermore, pyrochlore can also be observed for the 1 MgO – LALZO and 5 MgO – LALZO-samples. The peak intensity of the pyrochlore peaks increases with increasing Mg-content. No peaks belonging to pyrochlore can be observed for the MgO-free sample. Figure B.10 shows a comparison of the diffraction patterns of the "as received" and polished surfaces of the sintered 5 MgO – LALZO-samples. The observation of a decreasing peak intensity of $Li_4SiO_4$ upon polishing, alludes to the phase being a surface effect. This is not the case for LALO, where the peaks remain relatively unchanged. Interestingly, pyrochlore-peaks can not be observed on the "as received" surface, but only appears after polishing.

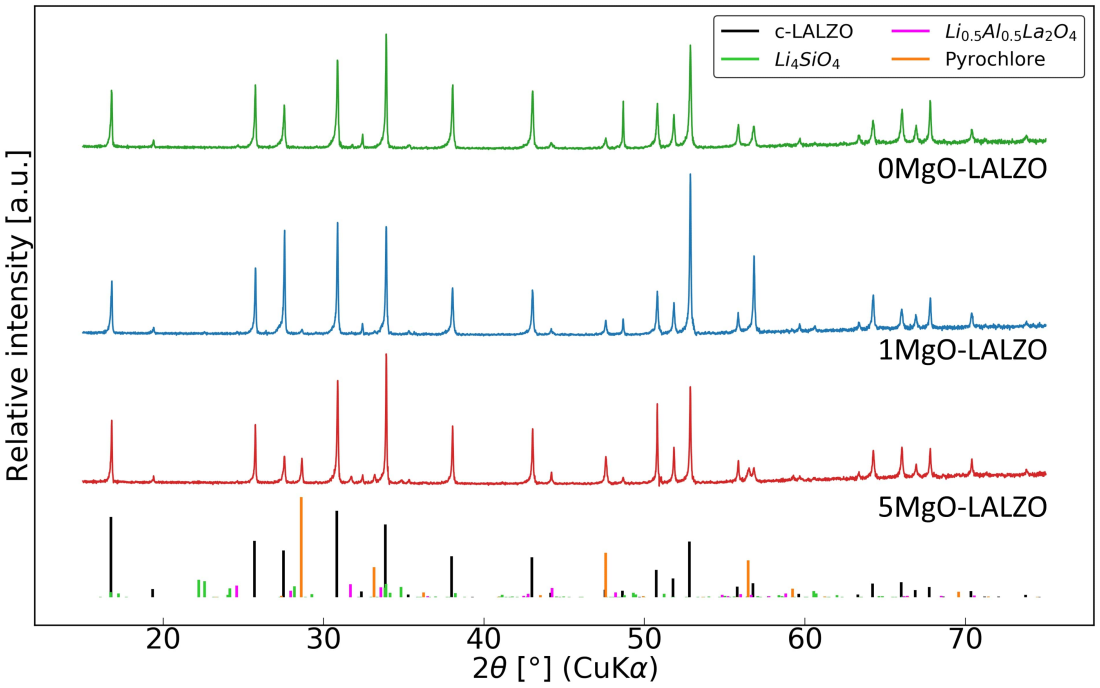


**Figure 4.5:** Bulk representative diffractograms of the samples sintered at 1150 °C for 6 h (M-1150 °C@6h/M). The main peaks are indexed to c-LALZO, in addition to some low-intensity peaks belonging to the $Li_4SiO_4$-impurity phase and the LALO-intermediate phase.

### 4.4.3 Microstructure of sintered samples

The microstructure of the pristine fracture surfaces of pellets sintered at 1150 °C for 1 h (M-1150 °C@1h/M) is shown in Figure 4.6. As seen from the low magnification images, the cross section shows a dense, homogeneous microstructure. No large grains can be observed, for neither of the pellet compositions. There is a tendency of bimodal grain size distribution, having grain sizes in the range of $<1\,\mu$m - 8 $\mu$m. From the high magnification images, it is evident that transgranular fracture occurs for the large grains and intergranular fracture for the small grains.

The microstructure of the pristine fracture surfaces of pellets sintered at 1150 °C for 6 h (M-1150 °C@6h/M) is shown in Figure 4.7. As opposed to the samples sintered for 1 h, the 6h-samples have experienced AGG. Large grains, with sizes varying from $\sim$50 $\mu$m-250 $\mu$m, have appeared in an otherwise dense, homogeneous matrix dominated by smaller grains. This is the case for all samples. The grains are mainly centered along the outer edges of the pellets, but a few larger grains can also be found in the center. From the high magnification images of areas without large grains, a very similar microstructure can be observed as that of the 1h-samples. A tendency of bimodal grain size distribution can also be observed here, having grain sizes in the range of $<1\,\mu$m - 8 $\mu$m. From the high magnification images, it is evident that transgranular fracture can be observed for the large grains and intergranular fracture for the small grains.

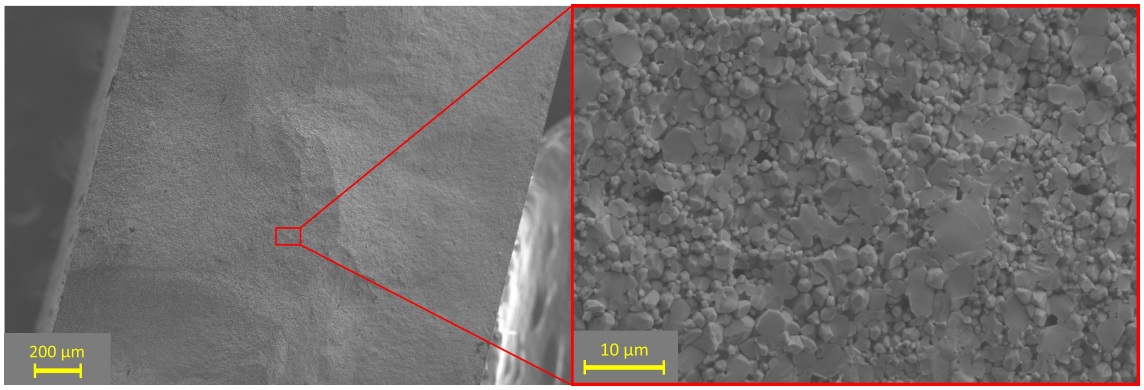


**(a)** 0MgO, 1150 °C @ 1 h, Low magnification **(b)** 0MgO, 1150 °C @ 1 h, High magnification

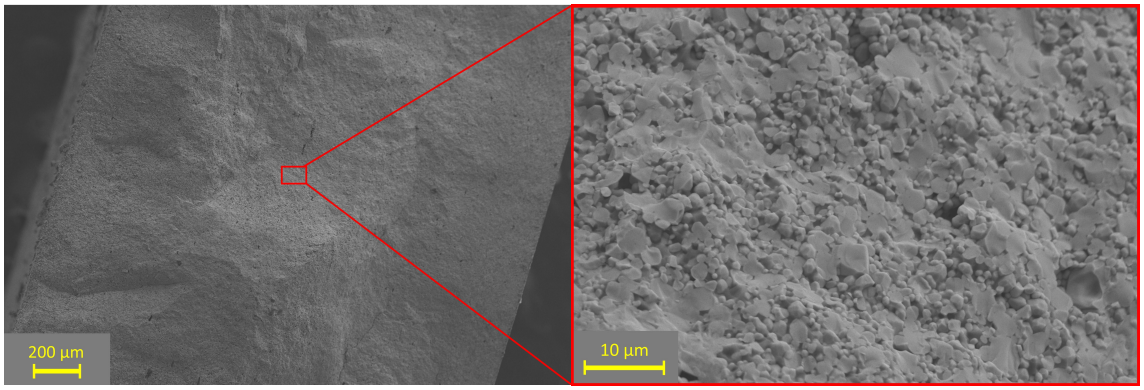


**(c)** 1MgO, 1150 °C @ 1 h, Low magnification **(d)** 1MgO, 1150 °C @ 1 h, High magnification

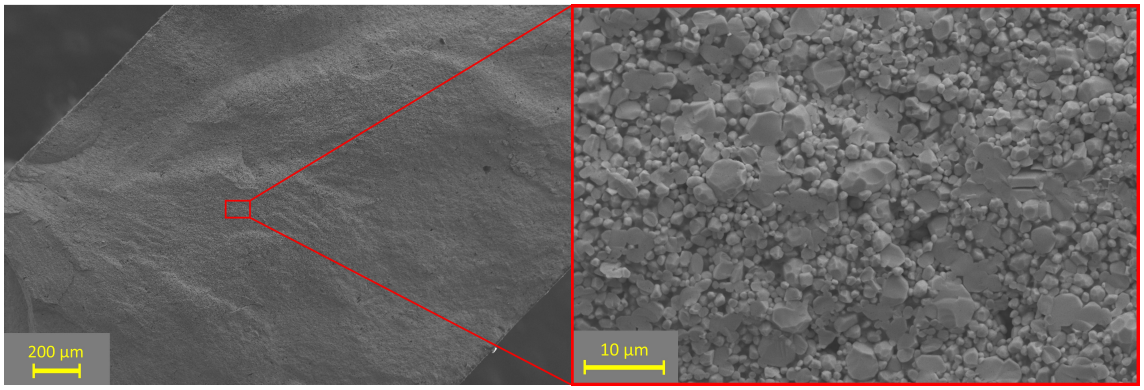


**(e)** 5MgO, 1150 °C @ 1 h, Low magnification **(f)** 5MgO, 1150 °C @ 1 h, High magnification

**Figure 4.6:** Secondary electron micrographs of pristine fracture surfaces of the different stoichiometries sintered at 1150 °C for 1 h (M-1150 °C@1h/M).

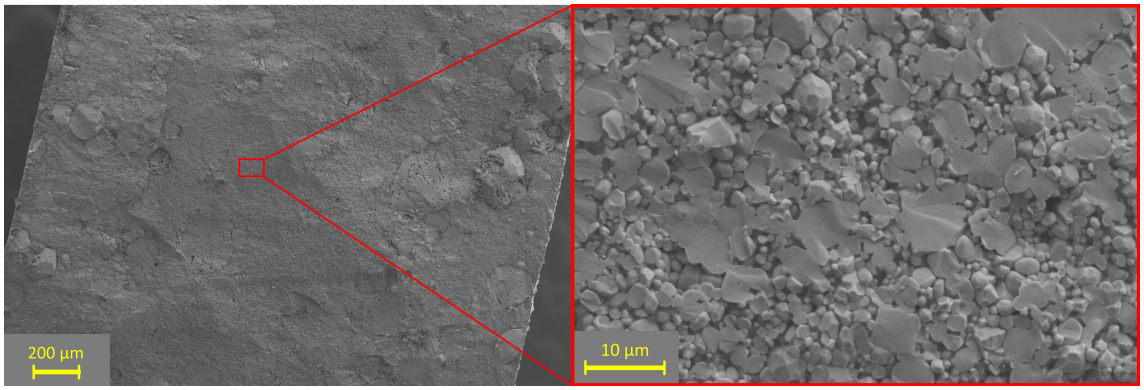


**(a)** 0MgO, 1150 °C @ 6 h, Low magnification **(b)** 0MgO, 1150 °C @ 6 h, High magnification

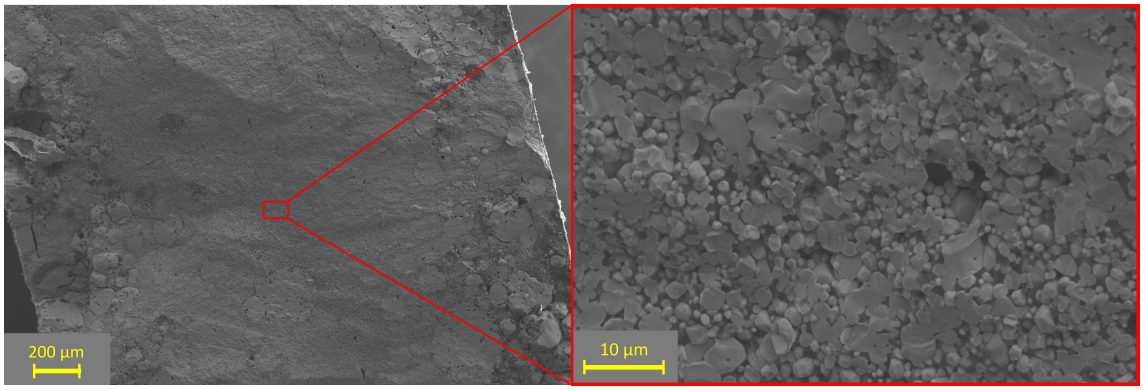


**(c)** 1MgO, 1150 °C @ 6 h, Low magnification **(d)** 1MgO, 1150 °C @ 6 h, High magnification

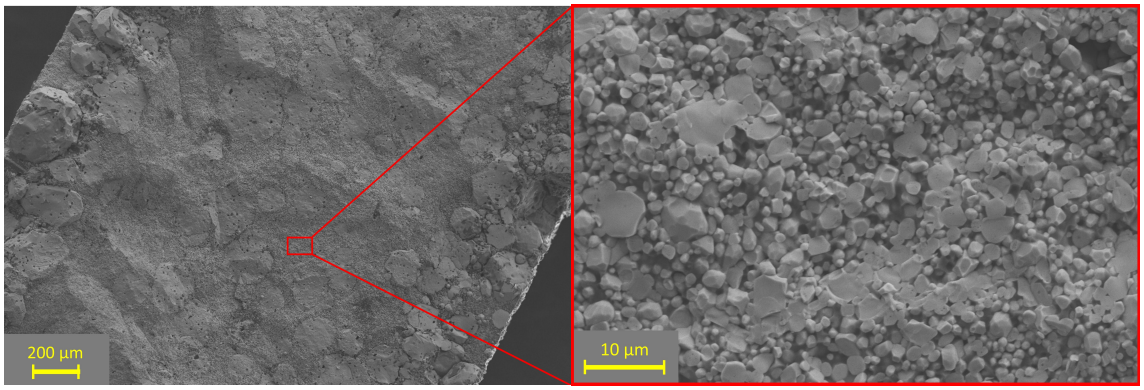


**(e)** 5MgO, 1150 °C @ 6 h, Low magnification **(f)** 5MgO, 1150 °C @ 6 h, High magnification

**Figure 4.7:** Secondary electron micrographs of pristine fracture surfaces of the different stoichiometries sintered at 1150 °C for 6 h (M-1150 °C@6h/M).

A more detailed look at the AGG phenomenon in shown Figure 4.8, for the 5 MgO – LALZO sample sintered at 1150 °C for 6 h (M-1150 °C@6h/M). The same also applies for the other pellet compositions as well. Large grains tend to be accumulated near the edges of the pellet surface, but a few large grain can also be observed in the bulk, as evident from the cross sectional image. The large grains are very dense, with some small pores entrapped within. This is also clearly visible from the "as received" pellet surfaces shown in Figure 4.9. Even on the pristine surfaces, small grains can be observed for the 1h-samples and abnormally large grains can be observed for the 6h-samples.

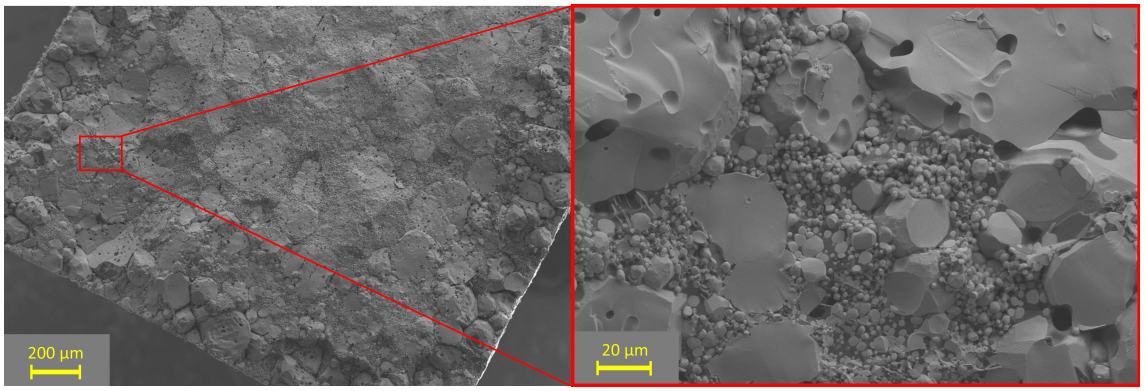


**(a)** 5MgO, M-1150 °C@6h/M, Low magnification **(b)** 5MgO, M-1150 °C@6h/M, High magnification

**Figure 4.8:** Secondary electron micrographs of pristine fracture surfaces of the 5 MgO – LALZO sample sintered at 1150 °C for 6 h (M-1150 °C@6h/M), that experienced abnormal grain growth.

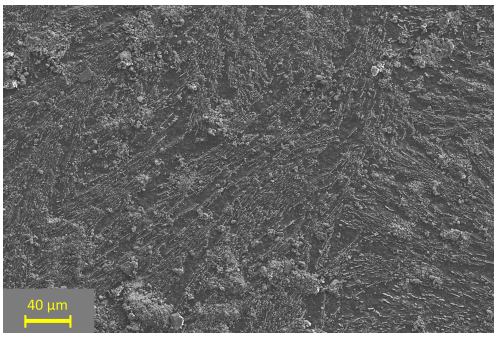


**(a)** 5MgO, M-1150 °C@1h/M, Low magnification

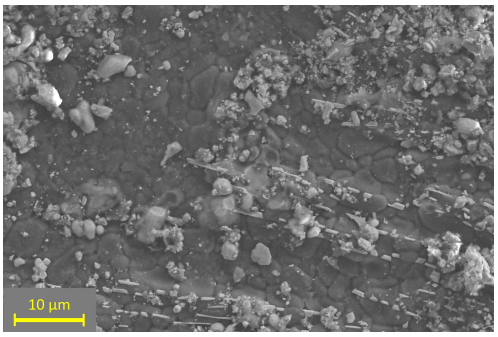


**(b)** 5MgO, M-1150 °C@1h/M, High magnification

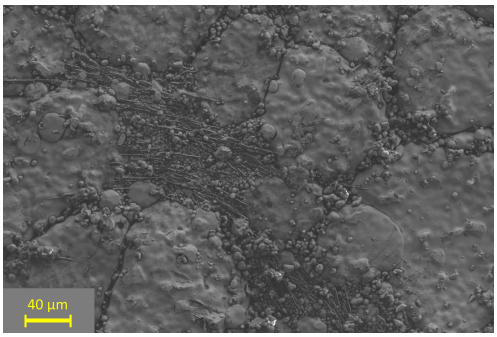


**(c)** 5MgO, M-1150 °C@6h/M, Low magnification

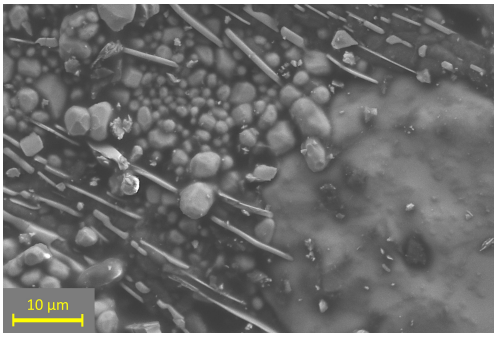


**(d)** 5MgO, M-1150 °C@6h/M, High magnification

**Figure 4.9:** Secondary electron micrographs of the "as received" surfaces of 5 MgO – LALZO pellets sintered at (a) and (b): 1150 °C for 1 h (M-1150 °C@1h/M) and (c) and (d): 1150 °C for 6 h (M-1150 °C@6h/M).

Figure 4.10 reveal the fracture behaviour and crack propagation of samples that have experienced AGG. In Figure 4.10a, a crack can be observed and appears to have propagated along the weak grain boundaries of the large grains. Figure 4.10b reveal the same trend, showing the fracture edge of the broken pellet.

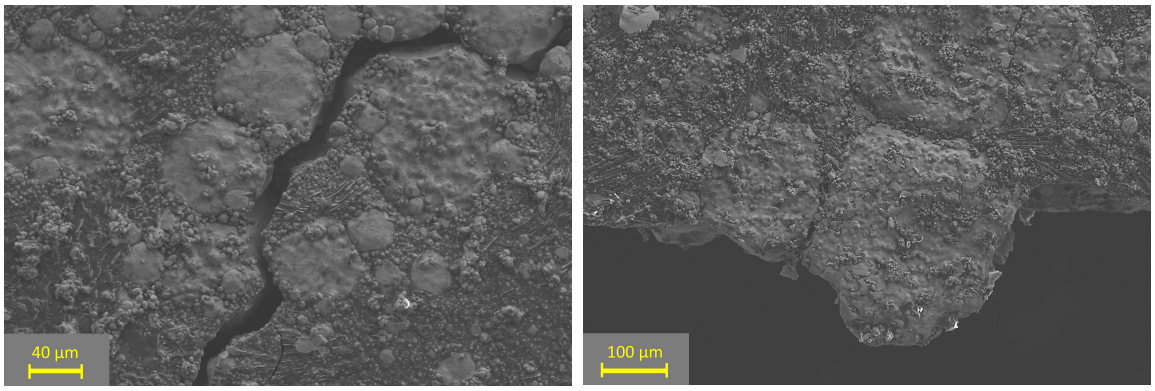


**(a)** 1MgO, M-1150 °C@6h/M **(b)** 5MgO, M-1150 °C@6h/M

**Figure 4.10:** Secondary electron micrographs of the "as received" surfaces of 1 MgO – LALZO and 5 MgO – LALZO pellets sintered at 1150 °C for 6 h (M-1150 °C@6h/M), that experienced abnormal grain growth.

### 4.4.4 Pellet composition and c-LALZO lattice parameters

A quantitative analysis of the composition of the sintered pellets (polished surfaces) was done via Rietveld refinement. The results are summarized in Table 4.1. The results reinforces the argument that the $Li_4SiO_4$-impurity phase and the LALO-intermediate phase only exist in small amounts. The analysis also confirmed the increasing pyrochlore content upon increased Mg-content in the samples sintered at 1150 °C for 6 h (M-1150 °C@6h/M). It should, however, be noted that the $R_{wp}$-value is rather high. $R_{wp}$ should ideally be lower than 5%. This indicates that there are uncertainties in the quantification, though some systems are expected to be more complex than others [119].

**Table 4.1:** Pellet composition of samples from the main sintering experiments, based on Rietveld refinement analysis.

| Sintering program | Sample | c-LALZO [wt %] | LALO [wt %] | $Li_4SiO_4$ [wt %] | Pyrochlore [wt %] | $R_{wp}$ [%] |
|---|---|---|---|---|---|---|
| M-1150 °C@1h/M | 0 MgO – LALZO | 95.3 | 0.8 | 3.6 | - | 19.8 |
| | 1 MgO – LALZO | 94.4 | 1.5 | 4.1 | - | 19.2 |
| | 5 MgO – LALZO | 93.8 | 1.5 | 4.7 | - | 19.3 |
| M-1150 °C@6h/M | 0 MgO – LALZO | 97.7 | 0.9 | 1.4 | 0.03 | 19.0 |
| | 1 MgO – LALZO | 94.4 | 0.4 | 2.8 | 2.4 | 20.8 |
| | 5 MgO – LALZO | 84.5 | 1.4 | 3.1 | 11.0 | 19.4 |

The Rietveld refinement also gives an estimation of the lattice parameters of the different phases. The lattice parameter of interest in this work is $a$ for c-LALZO, which is listed along with the corresponding $R_{wp}$-value in Table 4.2. The lattice parameter for pure LALZO ($Li_{6.25}Al_{0.25}La_3Zr_2O_{12}$) is reported to be 12.9633 Å in the PDF-4+ database [118], which is larger than the values reported in this work (Table 4.2). The lattice parameters remain relatively unchanged upon introducing Mg-doping. While the 1 h-samples display no clear trend, a declining lattice parameter can be observed with increasing Mg-content for the 6 h-samples.

**Table 4.2:** The lattice parameter, $a$, of the samples sintered during the main sintering experiments, based on Rietveld refinement analysis. The theoretical lattice parameter for pure LALZO is 12.9633 Å [118].

| Sintering program | Sample | $a$ [Å] | $R_{wp}$ [%] |
|---|---|---|---|
| M-1150 °C@1h/M | 0 MgO – LALZO | 12.9485 | 19.8 |
| | 1 MgO – LALZO | 12.9562 | 19.2 |
| | 5 MgO – LALZO | 12.9471 | 19.3 |
| M-1150 °C@6h/M | 0 MgO – LALZO | 12.9487 | 19.8 |
| | 1 MgO – LALZO | 12.9476 | 20.8 |
| | 5 MgO – LALZO | 12.9473 | 19.4 |

### 4.4.5 EDS mapping

Due to no observations being made of MgO or any other Mg-containing species in the XRD diffraction patterns, an attempt to produce a quantification of the Mg-content proved to be difficult. The EDS analysis done in this work was not sufficient to give a good indication of the distribution of the Mg. Thus, EDS mapping was used to semi-quantitatively characterize the Mg-content of the various pellet samples. The produced EDS-spectra from EDS mapping of the sintered pellets were used determine the presence, or lack there of, of Mg in the samples. The obtained spectra for the 0 MgO – LALZO, 1 MgO – LALZO and 5 MgO – LALZO samples sintered at 1150 °C for 6 h (M-1150 °C@6h/M) is shown in Figure 4.11, Figure 4.12 and Figure 4.13, respectively. In these samples, mapping was conducted in one of the large grains observed in these samples. SEM micrographs of the polished samples are shown in Figure D.1, where the scanning area is marked. The inset on the right hand side of the EDS-spectra highlights the area corresponding to the ionization energy of Mg. For 0 MgO – LALZO, no "Mg-shoulder" was observed in the spectrum. A small "Mg-shoulder" was observed for 1 MgO – LALZO, while a significantly larger "shoulder" was observed for 5 MgO – LALZO. This is to be expected, as the Mg-content has increased. Samples sintered at 1150 °C for 1 h (M-1150 °C@1h/M) was not analysed due to time constraints.

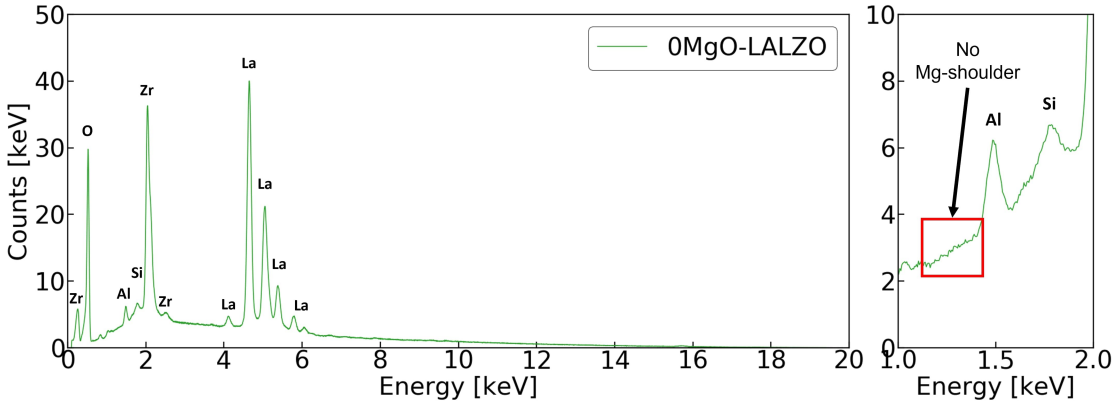


**Figure 4.11:** EDS-spectra obtained from EDS-mapping of the 0 MgO – LALZO sample sintered at 1150 °C for 6 h (M-1150 °C@6h/M). No "Mg-shoulder" was observed, as seen in the inset.

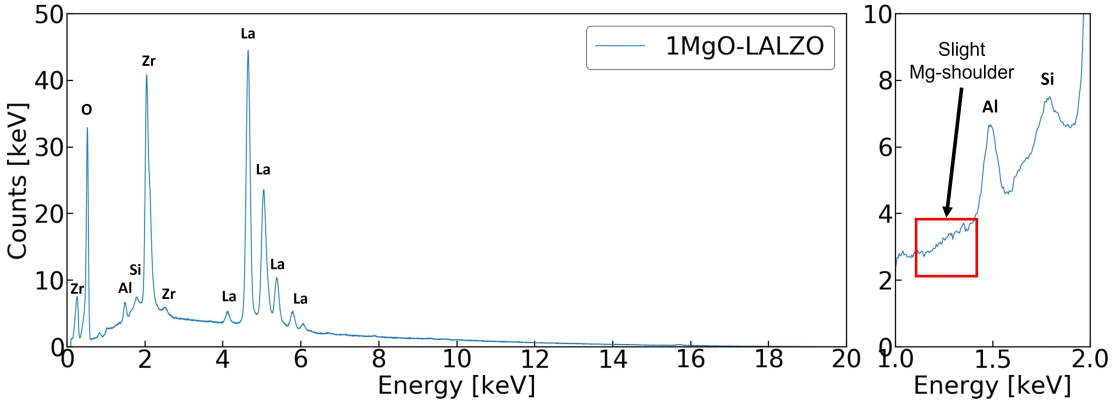


**Figure 4.12:** EDS-spectra obtained from EDS-mapping of the 1 MgO – LALZO sample sintered at 1150 °C for 6 h (M-1150 °C@6h/M). A slight "Mg-shoulder" was observed, as seen in the inset.

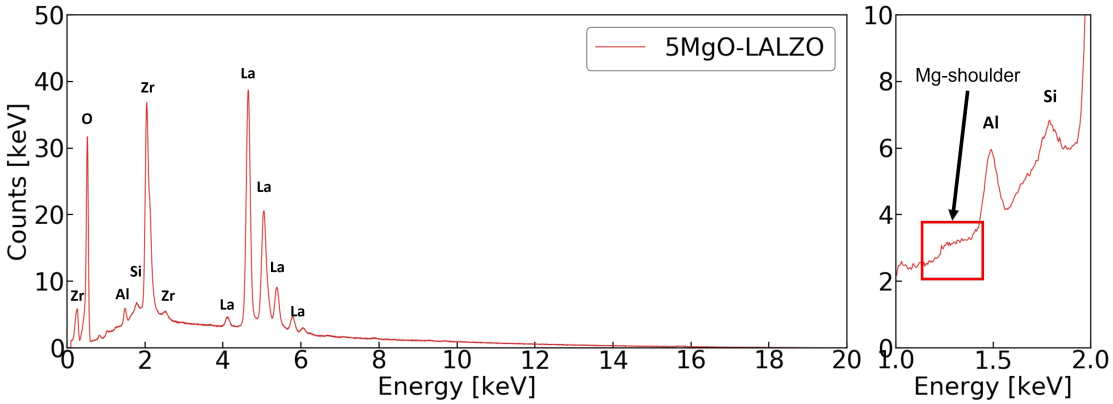


**Figure 4.13:** EDS-spectra obtained from EDS-mapping of the 5 MgO – LALZO sample sintered at 1150 °C for 6 h (M-1150 °C@6h/M). A "Mg-shoulder" was observed, as seen in the inset.

## 4.5 Ionic conductivity measurements

Impedance spectroscopy was used to study the $Li^+$-conductivity of pellets sintered in the main sintering experiments. For the purpose of making area calculations a bit easier, new samples sintered with the same sintering conditions as the main sintering experiments. The two parallels are: E-1150 °C@1h/M and E-1150 °C@6h/M. The corresponding Nyquist diagrams from the RT EIS-experiments are shown in Figure 4.14. The curves have been normalized, meaning the dimensions of the pellets have been taken into account in order to allow for comparison of samples with different surfaces.

The Nyquist plots reveal different electrical relaxation processes. For the samples sintered for 1 h, there are three regions: A high-frequency semicircle, a slightly lower frequency semicircle and a low-frequency inclined spike/tail. For the samples sintered for 6 h, there are only two regions: A high-frequency semicircle and a low-frequency inclined spike/tail. Each semicircle can be fitted using equivalent circuits consisting of a constant phase element (CPE) and a resistance element (R), connected in parallel. The corresponding equivalent circuits for the different sintering programs are shown as an insert in Figure 4.14, where the indices "b", "GB" and "BE" denote bulk, grain boundary and blocking electrodes, respectively. The spike can be attributed to the polarization response of the blocking electrodes. For the samples sintered for 1 h, the two semicircles can be assigned to bulk contributions and grain boundary contributions. However, the bulk- and grain boundary contributions can not be separated and only one semicircle can be seen in the Nyquist plots for the samples sintered for 6 h. Therefore, a model corresponding to the total bulk+grain boundary response must be evaluated.

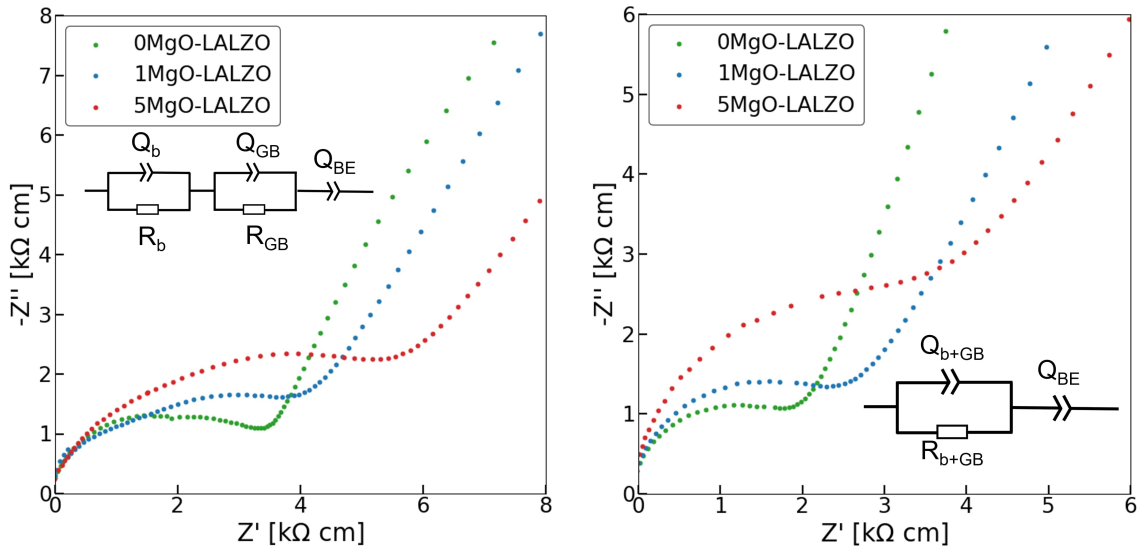


**(a)** E-1150 °C@1h/M

**(b)** E-1150 °C@6h/M

**Figure 4.14:** Normalized Nyquist diagrams for samples sintered at (a) 1150 °C for 1 h (E-1150 °C@1h/M) and (b) 1150 °C for 6 h (E-1150 °C@6h/M). Z' is the real part of the impedance, while Z" is the imaginary part of the impedance. Q = Constant phase element, R = Resistance element, b = Bulk, GB = Grain boundary and BE = Blocking electrode.

The total ionic conductivity, $\sigma_{tot}$, was determined by fitting the Nyquist plots to their equivalent circuits. From this, an estimation of the bulk resistance and grain boundary resistance, or the bulk+grain boundary resistance was done. This corresponds to the point of intersection between the high frequency semicircle and the Z'-axis, or the width of the semicircle. The Nyquist plots with the best fit for all samples are shown in Figure E.1. Additional information including relevant equations, the best fit parameters, and resistances and pellet dimensions are also given in Appendix E. Likewise, the resistances can also be determined from the plateau/inflection point in the corresponding Bode plots of the samples. The Bode plots for the samples sintered at 1150 °C for both 1 h and 6 h (E-1150 °C@1h/M and E-1150 °C@6h/M, respectively) is shown in Figure F.1. The Bode plots for each individual sample, with the various plateaus marked with horizontal dotted lines, are shown in Appendix F.

The total ionic conductivities of the 1 h-samples and the 6 h-samples were calculated using Equation E.1 and Equation E.2, respectively. The results are shown in Figure 4.15, with the exact values listed in Table 4.3. The table also lists the bulk conductivity, $\sigma_b$ of the samples where the bulk and grain boundary contributions were distinguishable. In general, the samples sintered for 6 h have higher total ionic conductivities than the 1 h-samples. Furthermore, the conductivity was observed to decreases with increasing Mg-content. This results in the 0 MgO – LALZO samples having the highest values. The highest achieved total ionic conductivity value was $1.46 \times 10^{-4}$ S/cm, which was measured for the 0 MgO – LALZO samples sintered at 1150 °C for 6 h (E-1150 °C@6h/M).

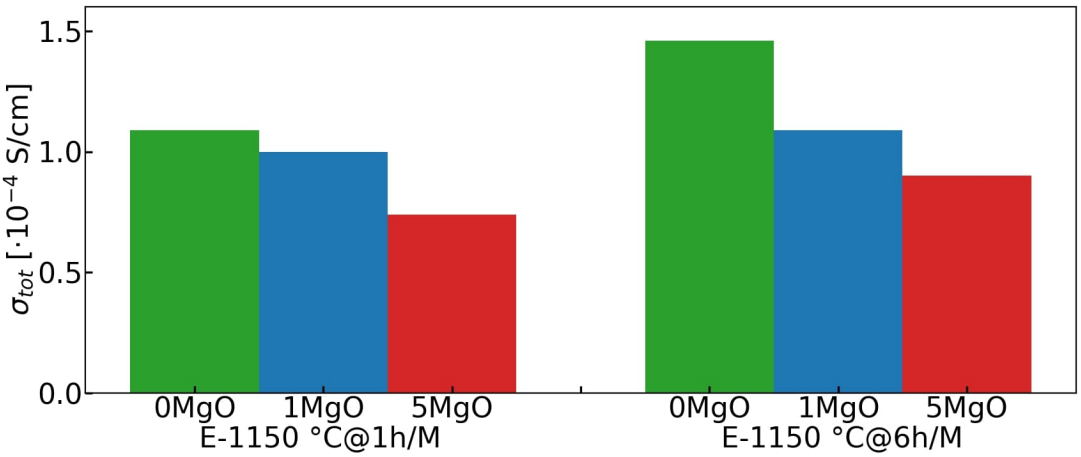


**Figure 4.15:** Histogram displaying the trend of the total ionic conductivities, $\sigma_{tot}$, of pellets sintered at 1150 °C @ 1h and 1150 °C @ 6h, using BP-ratio = 2 and MgO-crucibles. The values were calculated based on the fitted Nyquist diagrams of the different pellet compositions.

**Table 4.3:** The bulk conductivity, $\sigma_b$, and the total ionic conductivities, $\sigma_{tot}$, of pellets sintered at 1150 °C for 1 h (E-1150 °C@1h/M) and for 6 h (E-1150 °C@6h/M). The values were calculated based on the fitted Nyquist diagrams of the different pellet compositions.

| Sintering program | Sample | $\sigma_b$ [$\times 10^{-4}$ S/cm] | $\sigma_{tot}$ [$\times 10^{-4}$ S/cm] |
|---|---|---|---|
| E-1150 °C@1h/M | 0 MgO–LALZO | 1.93 | 1.09 |
| | 1 MgO–LALZO | 2.97 | 1.00 |
| | 5 MgO–LALZO | 2.35 | 0.74 |
| E-1150 °C@6h/M | 0 MgO–LALZO | - | 1.46 |
| | 1 MgO–LALZO | - | 1.09 |
| | 5 MgO–LALZO | - | 0.90 |

The diffraction patterns of the polished pellet samples used in the EIS measurements are shown for samples sintered for 1 h and 6 h in Figure 4.16 and Figure 4.17, respectively. For all samples and both sintering programs, the main peaks belong to c-LALZO. While the samples sintered for 6h consist of pure c-LALZO, the samples sintered for 1h show minor reflections corresponding to the impurity phase $Li_4SiO_4$ and the intermediate phase $Li_{0.5}Al_{0.5}La_2O_4$.

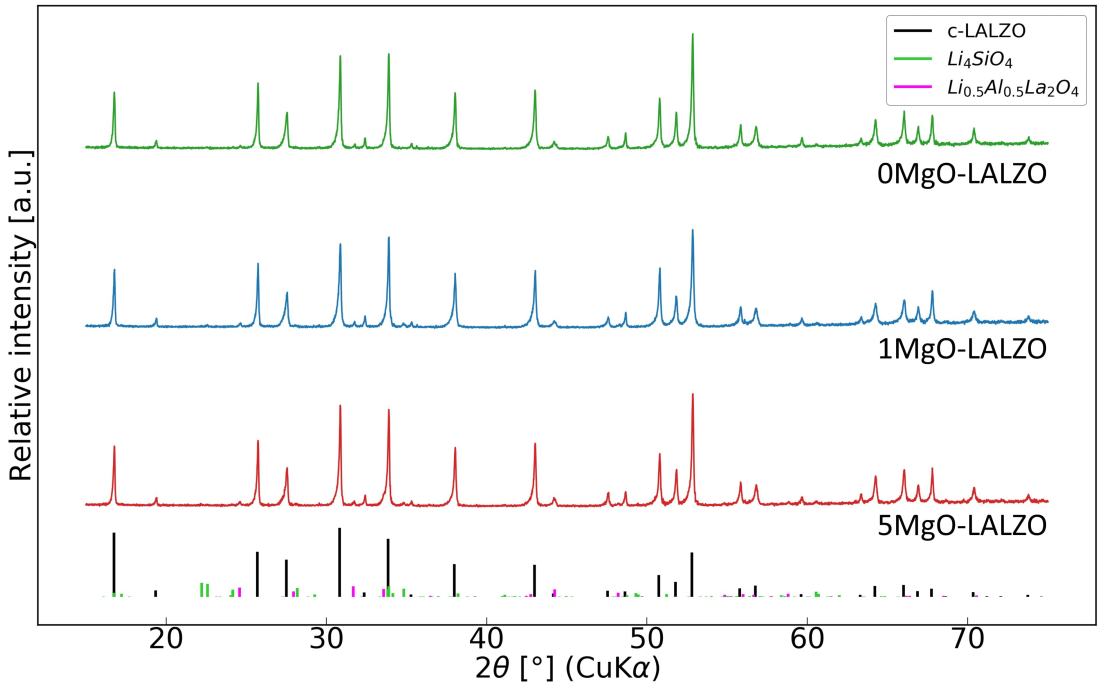


**Figure 4.16:** Samples sintered at 1150 °C for 1 h (E-1150 °C@1h/M). The main peaks belong to c-LALZO, in addition to some low-intensity peaks belonging to the $Li_4SiO_4$-impurity phase and the LALO-intermediate phase.

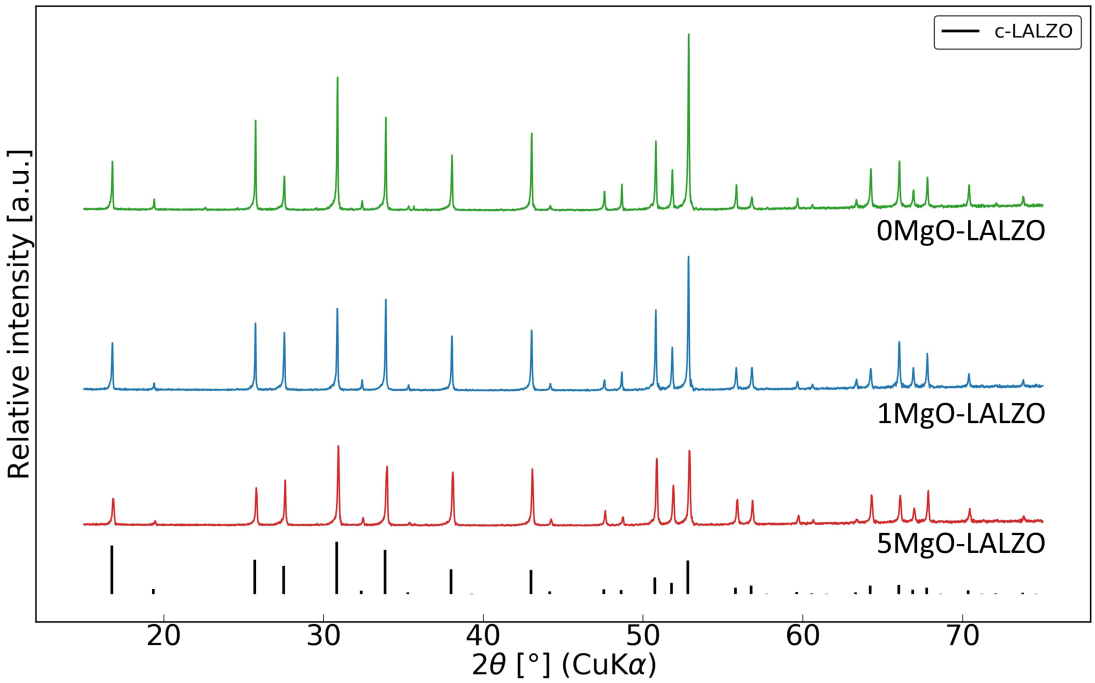


**Figure 4.17:** Samples sintered at 1150 °C for 6 h (E-1150 °C@6h/M). All peaks belong to c-LALZO and no other secondary phases can be observed.

# 5 Discussion

## 5.1 Heat treatment and phase composition by XRD

### 5.1.1 Dilatometry analysis

The dilatometry curves, as shown in Figure 4.2, indicate a reasonable choice of sintering at 1150 °C. This is approximately 50 °C above the maximum rate of densification. The choice of temperature also aligns well with temperatures reported in the literature (Table 2.3). Furthermore, the curves shows that the different sample stoichiometries exhibit very similar densification behaviors. No obvious correlation can be observed between the densification and the MgO-content.

As evident from the XRD-analysis, formation of pyrochlore has occured after sintering. This was prevalent both at the surface of the "as received" pellets and in the bulk of the polished pellets (Figure B.6). The formation of pyrochlore can be attributed to use of high temperatures and a flow of synthetic air during the experiments. As a consequence of the high volatility of Li, the flow will cause serious Li-loss. This will then lead to a reversion of c-LALZO to pyrochlore. In addition, no bedpowder was utilized during the experiments and will therefore not contribute to supplying excess Li and suppressing Li-loss. The observation of anomalous "humps" around 1150-1250 °C in the dilatometry curves are likely caused by the precipitation of pyrochlore.

### 5.1.2 Calcination

The diffraction patterns of the precursor powders are shown in Figure B.1. Precursor powders were calcined in batch sizes of ∼4 g at 750 °C for 12 h, using MgO-crucibles. As shown in Figure 4.1, calcination has successfully produced a single phase c-LALZO powder without any secondary phases. The absence of peak splitting indicates that no t-LALZO is present.

The choice of this calcination program was based on observations of the decomposition behaviour of the $Li_2CO_3$-intermediate phase, identified by Nybrodahl [13]. $Li_2CO_3$ has a melting point of 723 °C and decomposes according to Equation 2.3. By assuming that $Li_2CO_3$ needs to decompose to $Li_2O$ before it can react with pyrochlore and form c-LALZO, the $CO_2$ partial pressure was found to play an important role in the rate of decomposition. At moderate temperatures and when calcining larger batch sizes, the $CO_2$-equilibrium pressure is low and the $CO_2$-transport out of the charge is slow. The rate of decomposition can thus be increased by increasing the temperature and reducing the batch size [13].

However, both the crucible material and dimension of the crucibles were changed in this work. MgO-crucibles were implemented due to being inert with respect to Li. This means that no reactions with the crucible material are expected, as opposed to $Al_2O_3$-crucibles. To verify the

phase purity of the calcined powders, a calcination study comparing the effect of crucible material and calcination holding time was carried out. When using batch sizes of ∼4 g in the MgO-crucibles, calcination at 750 °C for 12 h gave phase pure c-LALZO without pyrochlore. This indicates that the decomposition of $Li_2CO_3$ and subsequent c-LALZO formation is complete.

### 5.1.3 Sintered samples

The preliminary sintering study revealed how variables like sintering temperature, sintering holding time, BP-ratio and crucible material affected the final sintered phase composition. Using a BP-ratio=0.5 resulted in residual pyrochlore after sintering, as evident from the diffraction patterns (Figure C.1 and Figure C.2). This is a result of severe Li-loss from the pellet surfaces that were not covered in bedpowder. Hence, BP-ratio of 2 or even higher should be implemented to supply excess Li. The next observation was that AGG occurs for the samples sintered at 1200 °C. The reasoning for this will be discussed in Section 5.3.3. Therefore, sintering at this temperature was avoided. Lastly, the influence of using $Al_2O_3$-crucible were investigated. The sintering experiments produced satisfactory phase compositions (Figure C.3 and Figure C.4), but using an inert crucible material like MgO was chosen in order to avoid any potential reactions between the pellets and the crucible.

A common feature in all the pellets sintered in this work, independent of compositions, is that the main phase is c-LALZO. This was valid for both the main sintering experiments (Figure 4.4 and Figure 4.5) and the preliminary sintering experiments (Appendix C). No t-LALZO was detected, as apparent from the absence of peak splitting. This is also an indication that the Li-excess is not too high, as a surplus of Li would cause formation of the tetragonal phase. Another common feature is the presence of small amounts of secondary phases. The phases were indexed to be pyrochlore, $Li_{0.5}Al_{0.5}La_2O_4$ (LALO) and $Li_4SiO_4$. The phase compositions of the pellets were verified by Rietveld refinement (Table 4.1). The secondary phases will be further discussed in Section 5.1.4.

As apparent from the diffraction patterns for all the samples studied in this work, whether calcined powders or sintered pellets, no secondary MgO phase or any other Mg-containing compounds have been observed. This could mean that the MgO is amorphous or that the crystallites are too small to be detected, as theorized by Huang et al. [59], making them undetectable by XRD. This was the case for shorter sintering durations (1-40 min), before the crystallite size increased after prolonged sintering (360 min) and MgO was observed by XRD. In this work, sintering durations of as high as 6 h were used, which would allow enough time to develop sufficiently large MgO crystallites. The absence of observed MgO indicates that Mg may occupy some lattice sites in the garnet, which will be discussed in Section 5.2.

Despite limited articles surrounding MgO-addition in the Al-doped LLZO system, the literature does report successful formation of grain growth inhibiting MgO for Ta- and Nb-doped LLZO. But the choice of dopant is likely not the attributing factor as to why MgO-formation was unsuccessful. More promising results might be linked to the preparation of the precursor powders. In the literature, MgO usually have been added to calcined LLZO powders and mixed together by ball milling. In this way, a mixed composite system is achieved, with small, homogeneous particle sizes [53]–[59].

### 5.1.4 Secondary phases

**Pyrochlore**: Formation of this phase is due to Li-loss and is a common observation in Li-deficient systems. Pyrochlore is present in the as received powder from spray pyrolysis (Figure B.1), which is to be expected. Upon calcination at 750 °C @ 12 h, pyrochlore has fully reacted. As shown in Figure 4.1, no residual pyrochlore was observed after calcination. The absence of pyrochlore peaks indicates low Li-loss from the garnet phase and no cubic-to-pyrochlore transformation having occured. Pyrochlore was observed for the experiments with BP-ratios = 0.5 and in the Mg-containing samples sintered at 1150 °C for 6 h (M-1150 °C@6h/M) during the main sintering study. The high Li-loss explains the first scenario, while in the case where sufficient amounts of bedpowders were applied (BP-ratio=2) is left unexplained. Pyrochlore was however not observed in the samples sintered for the EIS-measurements (E-1150 °C@6h/M, Figure 4.17), where exactly the same sintering conditions were utilized. The same applies for the samples sintered at the same conditions using $Al_2O_3$-crucibles (P-1150 °C@6h/A, Figure C.4). The variation in observed phases for presumably identical experiments indicate some challenges with reproducibility.

**LALO**: Formation of this phase is also an indication of Li-loss. To limit the formation of this phase, measures that enhances the Li-retention or similarly reduces the Li-loss should be taken. This includes using lower sintering temperatures and shorter sintering time, in addition to using larger amounts of Li-rich bedpowder. The occurrence of LALO is also related to the high Al-content, in which Al-substitution on Li-sites have caused a depletion of Li. This means that changing the dopant element to for instance Ta or Nb would eliminate the presence of the LALO phase, while still allowing for stabilization of c-LLZO via substitution on Zr-sites.

**$Li_4SiO_4$**: The appearance of this phase was unexpected and can be classified as an impurity phase. Although precautions were taken to avoid any contamination from the environment, some unknown Si-source has been present. No silicates or other Si-containing compounds were introduced during powder synthesis, meaning the contaminations likely stem from further processing. Potential sources of contaminations could include: (i) Impurities introduced from poorly cleaned agate mortars and sieves and (ii) Contamination of refractory material in the furnace after evaporation and condensation of Si-containing species. The last effect should however be limited as a result of using closed lids on the crucibles during sintering.

The amounts of secondary phases were evaluated according to Rietveld refinement (Table 4.1) and was determined to be small compared to c-LALZO. Furthermore, as evident from the comparison of the "as received" vs polished pellet surfaces presented in Appendix B.6, the concentration of $Li_4SiO_4$ and LALO is higher on the pristine surfaces compared to the polished surfaces. The impurities are enriched at the surface and will be removed by gentle polishing. This is ideal, as secondary phases tend to restrict $Li^+$-conduction.

## 5.2 Mg-substituted LALZO

### 5.2.1 Confirming the Mg-substitution

The lack of any observed Mg-phases by XRD suggests that secondary MgO have not been formed despite the formation being thermodynamically possible during the high-temperature spray pyrolysis process. The reason as to why this has not occured is not clear at the time. Instead, this suggests that Mg occupies some lattice sites in the garnet. This substitution could cause formation of secondary phases. For instance if Mg occupy Zr-sites, secondary Zr-rich compounds like pyrochlore ($La_2Zr_2O_7$) or $Li_2ZrO_3$ will be expected.

EDS analysis was conducted to semi-quantitatively study the Mg-content in the sintered pellets. The EDS analysis was, however, not sufficient to produce any conclusive quantification of the Mg-content or give a good indication of the distribution of Mg. The presence of Mg could however be confirmed by the observation of "Mg-shoulders" in the obtained EDS-spectra after mapping. No peak can be found for 0 MgO – LALZO (Figure 4.11), while the peak intensity increases with increasing Mg-content for the 1 MgO – LALZO and 5 MgO – LALZO samples (Figure 4.12 and Figure 4.13). It can therefore be concluded that Mg can be observed in LALZO where MgO have been intentionally added.

With Mg being introduced at some lattice site, a change in the cell parameter would be expected. This is verified via Rietveld refinement (Table 4.2), where at least the samples sintered for 6 h (M-1150 °C@6h/M) display a clear trend of reduced unit cell parameter with increasing Mg-content. This is a good indication that Mg does occupy a lattice site in the garnet.

### 5.2.2 Potential lattice sites hosting $Mg^{2+}$

Two different lattice sites are considered: (i) Mg-substitution on Zr-sites or (ii) Mg-substitution on Li-sites. Both scenarios are feasible, as the ionic radii are very similar. 6-coordinated $Zr^{4+}$ and $Mg^{2+}$ have identical ionic radii of 0.72 Å, while the ionic radii for 4-coordinated $Li^+$ and $Mg^{2+}$ are 0.59 Å and 0.57 Å, respectively [50].

If **Mg substitutes on Zr-sites**, the native Zr-ions are replaced and causes a disruption of the charge neutrality. Since Mg has a lower valency (2+) compared to Zr (4+), formation of Li-vacancies are suppressed. Instead, 2 free $Li^+$-ions per Mg will enter interstitial lattice sites or enter existing Li-vacancies. This will have a negative impact on the ionic conductivity, due to the loss of Li-vacancies. However, Mg-substitution on Zr-sites avoids obstructions of the $Li^+$-diffusion pathways.

Another potential explanation of how the charge neutrality is sustained was proposed by Jiang et al, who also studied Mg-substitution on Zr-sites [48]. The authors claim that more than one $Mg^{2+}$ can enter the Zr-sites, as supported by an observation of a peak shift in the XRD diffractograms of pure LLZO vs. Mg-doped LLZO. This was caused by an expansion of the lattice. This can be explained by strong coulombic forces between the $Mg^{2+}$-ions of equal charge, where repulsive interactions will cause lattice strain. The likelihood of this occurring is fairly low, meaning that the filling of Li-vacancies or increase in number of interstitial Li-atoms seems more plausible. Since the substitution "kicks out" Zr, there is a possibility that Zr-secondary phases gets formed.

If **Mg substitutes on Li-sites**, the native Li-ions are replaced and also causes a disruption of the charge neutrality. Opposed to what happens for the case of Mg-substitution on Zr-sites, this substitution would require that each Li-atom needs to form one Li vacancy. This is similar to the mechanism of Al-doping, however this substitution only introduces one Li-vacancy compared to two per Al-ion. No distinct Li-containing secondary phases is expected to form as a result of this substitution, as Li is volatile and will be released as VLCs. Despite forming favorable Li-vacancies, this substitution is also expected to reduce the $Li^+$ conductivity. This is due to the Mg hindering $Li^+$ mobility, through obstructions of the $Li^+$-diffusion pathways in the lattice.

Deciding which of the two potential substitutions is most likely to have occurred, is hard to conclude. Both options appears to be possible with respect to ionic radii. However, the Mg-substitution on Zr-sites is the most commonly reported occurrence in the literature, based on both experimental- and computational findings [48], [49], [51].

## 5.3 Microstructure of sintered samples

### 5.3.1 The effect of green density

Usually there is a correlation between the green density and the sintered density, where higher green densities are expected to give higher final sintered densities. This correlation can also be observed in the densities achieved in this work, where samples with higher green densities produced higher sintered densities. The obtained green densities and sintered densities are listed in Table A.1. A trend of reduced green density can be observed for increasing MgO-concentration, although the highest sintered density obtained in this work was achieved for the 5 MgO – LALZO

sample sintered at 1150 °C for 1 h (P-1150 °C@1h/M). This hints towards some inconsistencies in the proposed correlation, which can be contributed to challenges with reproducibility. Finding strategies that increases the green density is crucial in order to increase the sintered density. This can be achieved by instance avoiding agglomerations or using a broader particle size distribution (bimodal mixtures), which would allow for a higher degree of packing.

### 5.3.2 Relative densities and microstructure

As listed in Table A.2, all samples across all sintering experiments experience similar relative densities. The values ranges from 84.6-90.9%. This is lower than what was expected from the literature (Table 2.3) and indicates a significant degree of porosity. This is also visible from the high-magnification SEM micrographs shown in Figure 4.6 and Figure 4.7.

It is hard to identify any specific effect of altering the different variables, though a few trends emerge. Increasing the temperature from 1150 °C to 1200 °C gives slightly higher densities, which is also expected from the theory. Increasing the BP-ratio and switching crucible materials from $Al_2O_3$ to MgO both causes lower density values, though some exceptions can be observed. The presence of secondary phases does not appear to have a major impact on the final density, but is challenging to conclude due to the small amounts present in each sample.

The most obvious change in the microstructure and density occurs when altering the sintering time. Increasing the sintering time from 1 h to 6 h causes an increase in the relative densities for the 0 MgO – LALZO samples, but gives decreasing values for the Mg-containing samples. The trend is observed across all sintering programs. The decrease in the relative density with increasing Mg-content is evident from the high degree of porosity. This is also evident from the observation of a reduced number of "large" (non-AGG prone) grains observed upon increasing the Mg-content, as shown in the high-magnification SEM micrographs (Figure 4.6 and Figure 4.7). The smaller grains are not as strongly bonded as the large grains, which gives rise to porosity and lower densities.

It should however be noted that there are uncertainties to the calculated relative density values reported in this work. This includes uncertainties relating the the measurement equipment. To ensure reproducible density values, repeated measurements should ideally be done. This included doing multiple weight measurements of the same samples and making new pellets with identical sintering conditions, to verify the obtained densities. The variation in the obtained densities of the various sintering experiments indicate some challenges with reproducibility combined with a sensitivity to variation in sample preparation.

### 5.3.3 AGG

Based on the conclusion that MgO is not formed as a separate phase, the mechanism of MgO at the grain boundaries hindering grain growth is not expected. This is evident from the observation of AGG, which was observed for samples sintered at:

- 1150 °C for 6 h (M-1150 °C@6h/M), as shown in Figure 4.7 and Figure 4.8
- 1200 °C for 1 h (P-1200 °C@1h/M), as shown in Figure C.6a and Figure C.6b
- 1150 °C for 6 h (P-1150 °C@6h/A), as shown in Figure C.6c and Figure C.6d

There is a tendency of bimodal grain size distribution, where transgranular fracture is observed for the large grains and intergranular fracture for the small grains (Figure 4.6 and Figure 4.7). As a result of the formation and growth of these large grains, a reduction in mechanical strength is expected. This was confirmed by the observation of cracks propagating along the grain boundaries of the large grains, as shown in Figure 4.10a and Figure 4.10b. As the grains growth to a certain size, the grain becomes prone to both transgranular and intergranular fractures, as evident from Figure C.6d. Furthermore, lithium metal dendrites prefer to propagate along grain boundaries. This means that dendrites will form and grow more easily compared to dense microstructures with small, tightly bound grains.

AGG has occured as a result of using high temperatures (1200 °C) and longer sintering holding times (6 h). AGG was avoided for samples sintered at lower temperatures (1150 °C) and shorter sintering holding times (1 h), as shown in Figure 4.6 and Figure 4.9a. The choice of crucible material does not appear to influence whether AGG occurs or not. The BP-ratio did not have any observable effect either. The literature does however report enhanced AGG with increasing BP-ratios [80], [112].

The AGG-phenomenon appears to be related to the formation of a secondary $Li_2O$-$Al_2O_3$ (Li-Al-O) phase at elevated temperature. As evident from the SEM micrographs of the samples where AGG have occured (Figure 4.8 and Figure C.6), large grains tend to accumulate near the surface of the pellet and continues to grow inward. As reported by Huang et al. [81], high levels of VLC causes AGG to occur as a result of condensation of VLCs on the the surface of the pellet. With a melting point of 1055 °C, the Li-Al-O phase is a liquid at the applied sintering temperature and enables liquid phase sintering. Wetting of the ceramic particles and viscous flow allows for enhanced densification and improved diffusion rates. The liquid phase is located at the interface between the large grains and the smaller grains, as observed by Eriksen [10]. Dissolution of smaller grains in the liquid phase and a subsequent re-precipitation on the surface of the large grains causes high growth rates of these large grains. This causes extensive growth of the large particles at the expense of the smaller grains.

AGG is therefore believed to be avoidable by preventing the formation of liquid Li-Al-O phase, which can be achieved by lowering the sintering temperature (below 1055 °C) or avoiding the eutectic composition. Tian et al. found that samples with high Al-contents (0.15-0.25 Al per formula unit) sintered at 1180 °C for 15 h experienced AGG [8]. This is comparable to this work, but altering the Al-content would not be feasible as a solubility limit of around 0.21 Al per formula unit is required for the stabilization of the cubic LALZO phase at room temperature [25]. Furthermore, the results obtained in this work also illustrates that AGG can be avoided by lowering the sintering temperature and duration. This could, however, result in lower densities. Other options to avoid AGG includes testing alternative sintering inhibitors or using a two-step sintering program, where densification can occur at lower temperatures where AGG is inactive and the high growth rates associated with elevated temperatures can be limited [9], [113].

## 5.4 Ionic conductivity of sintered samples

### 5.4.1 Observed trends from the Nyquist diagrams

As shown in Figure 4.14, the two different sintering programs yields different spectra with either one or two semicircles. For the sample sintered for 1150 °C for 1 h (E-1150 °C@1h/M), one high-frequency semicircle and one slightly lower frequency semicircle can be observed. The first semicircle (high frequency) can be attributed to the bulk resistivity, which corresponds to resistivity of the grains. The other semicircle (lower frequency) can be attributed to the grain boundary resistivity. This case is commonly associated with LLZO, since the bulk ionic resistivity is normally lower than the grain boundary resistivity as a result of the high $Li^+$ conductivity of the cubic polymorph [115]. For the sample sintered at 1150 °C for 6 h (E-1150 °C@6h/M), there is only one semicircle. For this case, the bulk and grain boundary contributions are not separable, meaning the semicircle represents the combined effect. This would be the case for systems where the grain boundary resistivity is negligible [74]. For both cases, a low-frequency inclined spike/tail can be observed and occurs due to polarization of the blocking electrodes. These features corresponds to two different equivalent circuits, as shown in Figure 3.7 and in the insets in Figure 4.14.

The results of the EIS experiments show that the samples sintered for 6 h exhibit a higher ionic conductivity, for all pellet stoichiometries, compared to the samples sintered for 1 h. This is shown in Figure 4.15 and Table 4.3. The reasoning for this is not directly evident based on the phase composition of the two samples. As discussed previously, the two sintering programs results in similar phase purity: Mainly c-LALZO + small amounts of $Li_4SiO_4$ and LALO. The presence of pyrochlore for the 6 h-sample would hint towards a lower ionic conductivity, due to the Li-loss associated with the formation of this phase. This is however not the case based on the experiments, which further supports the argument that the occurrence of pyrochlore might be related to the lack of reproducibility. The effect of pyrochlore is expected to depend on both concentration and

location of precipitation. If pyrochlore is mainly formed at the triple points between the grains, it is less critical compared to pyrochlore formation at the grain boundaries. Any potential effects of these secondary phases are challenging to address, due to the small amounts present in each sample. Despite $Li_4SiO_4$ being reported to enhance the conductivity when being used as a sintering additive [74], any potential impact can not be identified in this work.

The obvious reasoning for the enhanced conductivity of the 6 h samples is that these samples have experienced AGG. As the large, dense grains continued to grow, the smaller grains were consumed. This caused the number of grains to be significantly reduced, giving rise to a reduction in the grain boundary density of the samples. This is evident when comparing Figure 4.9a and Figure 4.9c. The extended duration at high temperatures gives good bonding between the grains and thus reduces the grain boundary resistance, allowing enhanced ionic conductivity. For the 1 h-samples, the microstructure is dominated by small grains and a high grain boundary density, which results in higher grain boundary resistances, two separable semicircles and lower ionic conductivities.

Despite the higher ionic conductivities associated with the samples that have experienced AGG, this is not an ideal method of increasing the ionic conductivity. This is due to the lowered mechanical strength, making the material prone to Li-metal dendrite growth and a poor candidate for solid-electrolyte purposes. A microstructure with small and strongly bound grains combined with high density is preferred, as it offers both high conductivity and high mechanical strength. Furthermore, it is hard to draw a conclusion regarding the reproducibility of the results achieved in this work. This is due to the low number of parallels. Measurements were only conducted once on one set of samples from the main sintering program.

### 5.4.2 The effect of Mg-substitution

There is a clear correlation between the Mg-content and the ionic conductivity. For both sintering programs, the conductivity decreases with increasing Mg-content. This can be explained by Mg acting as a dopant, entering some lattice sites in LALZO. Regardless of whether Mg have substituted Zr-sites or Li-sites, the ionic conductivity is expected to decrease. Mg-substitution on Zr-sites causes a consumption of Li-vacancies and formation of Zr-rich secondary phases, while Mg-substitution on Li-sites causes obstruction of the $Li^+$ conduction pathways. These effects are therefore expected to increase with increasing Mg-content.

The highest total ionic conductivity measured in this work was $1.46 \times 10^{-4}$ S/cm, which was achieved for the 0 MgO – LALZO sample sintered at 1150 °C for 6 h (E-1150 °C@6h/M). This value is in the lower end of what has been reported for LALZO produced by ambient air sintering (Table 2.3) and for LLZO systems where MgO has been added as a sintering additive (Table 2.4). The values obtained in this work is, however, not expected to be directly comparable to those reported in the literature. This is due to the difference in synthesis method (spray pyrolysis),

varying Li-excess values and due to secondary MgO not being formed. Since we conclude that our samples are most likely doped with Mg, it is interesting to compare with ionic conductivities reported in the literature for Mg-doped LLZO (Table 5.1).

**Table 5.1:** The total ionic conductivities, $\sigma_{tot}$, achieved for Mg-doped LLZO, as reported in the literature. ASS = Ambient air sintering.

| Composition | Sintering conditions | $\sigma_{tot}$ [$\times 10^{-4}$ S/cm] | Author |
|---|---|---|---|
| $Li_{7.1}La_3Zr_{1.95}Mg_{0.05}O_{12}$ | AAS, 1230 °C @ 16 h | 4.32 | Song et al. [51] |
| $Li_7La_3Zr_{1.95}Mg_{0.1}O_{12}$ | AAS, 1075 °C @ 12 h | 2.91 | Jiang et al. [48] |
| $Li_7La_3Zr_{1.9}Mg_{0.2}O_{12}$ | AAS, 1075 °C @ 12 h | 0.98 | Jiang et al. [48] |

A trend of decreasing ionic conductivity can be observed with increasing Mg-contents, which corresponds well with the observations made in this work. The obtained Li-ion conductivities for the 1 MgO – LALZO samples (1.00 and $1.09 \times 10^{-4}$ S/cm for samples sintered at 1150 °C for 1 h and 6 h, respectively) aligns well with the reported value in the literature for the sample with a similar Mg-content ($0.98 \times 10^{-4}$ S/cm). The increased MgO-concentration in the 5 MgO – LALZO samples would explain the reduced conductivities (0.74 and $0.90 \times 10^{-4}$ S/cm for the 1 h-sample and the 6 h-samples, respectively).

# 6 Conclusion

Calcination of ∼4 g of precursor powders at 750 °C for 12 h using MgO-crucibles resulted in a phase pure material, consisting of single phase cubic LALZO. A preliminary sintering study concluded that low BP-ratios resulted in residual pyrochlore due to high Li-loss.

Pellets sintered at 1150 °C for 1 h and 6 h, using BP-ratio=2 and MgO-crucibles were basically cubic LALZO with small amounts of secondary phases ($Li_4SiO_4$, $Li_{0.5}Al_{0.5}La_2O_4$ and $La_2Zr_2O_7$), as confirmed by XRD and Rietveld analysis. However, no Mg-containing compounds were identified by XRD in any of the sintered samples. Combined with the observation of large grains in samples sintered at high temperatures (1200 °C) and extended sintering times (6 h), this indicated that the MgO-addition did not have the intended effect of reducing AGG.

EDS-analysis combined with a reduced cubic cell parameter with increasing content of MgO were interpereted in terms of Mg entering specific lattice sites in LALZO, either Zr- or Li-sites. Both types of substitutions were hypothesized to reduce Li-ionic conductivity, due to loss of Li-vacancies and obstruction of the $Li^+$ conduction pathways, respectively. The assumption was confirmed by EIS-analysis, showing a reduced ionic conductivity with increasing concentration of Mg. Samples sintered for 6 hours exhibited higher Li-ion conductivities compared to the 1 hour samples. This was a result of the reduced grain boundary resistance due to AGG significantly reducing the density of grain boundaries. The highest total ionic conductivity was $1.46 \times 10^{-4}$ S/cm, achieved for the 0 MgO − LALZO sample sintered at 1150 °C for 6 hours, while the lowest ionic conductivity was observed for the 5 MgO − LALZO sample sintered at 1150 °C for 1 hours and was measured to be $0.74 \times 10^{-4}$ S/cm.

Finally, since Mg substitutes lattice sites and reduce the Li-ionic conductivity, other strategies must be chosen to suppress AGG.

# 7 Further Work

Future efforts should address the AGG observed after sintering and find ways to avoid it, combined with increasing the relative densities even further. The aim is to achieve a high-density material with a microstructure dominated by small and strongly bound grains. Higher densities can be achieved by using novel sintering strategies such as two-step sintering techniques, hot-pressing or spark plasma sintering.

Alterations in the production and further processing of the precursor powders should be considered, to ensure a phase pure c-LALZO material without secondary phases and Si-contaminations. The actual composition of the powders/pellets could be determined by using techniques such as inductively coupled plasma mass spectroscopy (ICP-MS), in order to verify the stoichiometry. Wavelength-dispersive spectroscopy (WDS) could potentially be a better alternative to EDS when it comes to the quantification and distribution of each element. Alternatively, point scans in areas free of porosity and secondary phases could give more reliable results compared to EDS-mapping of a large area.

To verify the reproducibility of the measured ionic conductivities, multiple parallels of sintered samples should be analyzed. Moreover, it would be beneficial to perform EIS-measurements over a variety of temperatures to obtain a more reliable separation of the ionic conductivity contribution from bulk and grain boundaries, respectively. Enhanced conductivities could also be obtained by introducing alternative dopants. Using dopants such as Ta, Nb and Ga are associated with ionic conductivites of $\geq 1.0\,\mathrm{mS/cm}$.

Another interesting challenge is the decomposition behavior of the intermediate phase $Li_2CO_3$. As identified by Nybrodahl [13], the decomposition of $Li_2CO_3$ impedes the formation of phase pure c-LLZO. Future studies could therefore be focused on developing and advising alternative precursor solutions that minimizes/avoids carbonate formation during spray pyrolysis.

# Acknowledgements

In addition to my supervisors, I would also like to thank all the laboratory engineers and the technical staff at IMA for their guidance and support in the lab. I also want to thank Florian Flatscher for his tremendous help with the EIS-measurements, and to Assoc. Prof. Daniel Rettenwander and Hung Quoc Nguyen for their help with the experimental fitting of the data. Furthermore, thank you to Senior Engineer Yingda Yu and Frode Håskjold Fagerli for their guidance during the EDS-analysis. Finally, I would like to thank all the members of the FACET battery group for their feedback and interesting conversations during our weekly meetings.

# References


[1] Q. Wang, P. Ping, X. Zhao, G. Chu, J. Sun and C. Chen, 'Thermal runaway caused fire and explosion of lithium ion battery', *Journal of Power Sources*, vol. 208, pp. 210–224, Jun. 2012. DOI: 10.1016/j.jpowsour.2012.02.038.

[2] J. Awaka, N. Kijima, H. Hayakawa and J. Akimoto, 'Synthesis and structure analysis of tetragonal $Li_7La_3Zr_2O_{12}$ with the garnet-related type structure', *Journal of Solid State Chemistry*, vol. 182, no. 8, pp. 2046–2052, Aug. 2009. DOI: 10.1016/j.jssc.2009.05.020.

[3] M. Kotobuki, H. Munakata, K. Kanamura, Y. Sato and T. Yoshida, 'Compatibility of $Li_7La_3Zr_2O_{12}$ Solid Electrolyte to All-Solid-State Battery Using Li Metal Anode', *Journal of The Electrochemical Society*, vol. 157, no. 10, A1076, 2010. DOI: 10.1149/1.3474232.

[4] A. Bhide, J. Hofmann, A. Katharina Dürr, J. Janek and P. Adelhelm, 'Electrochemical stability of non-aqueous electrolytes for sodium-ion batteries and their compatibility with $Na_{0.7}CoO_2$', *Physical Chemistry Chemical Physics*, vol. 16, no. 5, pp. 1987–1998, Jan. 2014. DOI: 10.1039/C3CP53077A. [Online]. Available: https://pubs.rsc.org/en/content/articlehtml/2014/cp/c3cp53077a%20https://pubs.rsc.org/en/content/articlelanding/2014/cp/c3cp53077a.

[5] J. Lu, Z. Chen, F. Pan, Y. Cui and K. Amine, 'High-Performance Anode Materials for Rechargeable Lithium-Ion Batteries', *Electrochemical Energy Reviews*, vol. 1, no. 1, pp. 35–53, Mar. 2018. DOI: 10.1007/s41918-018-0001-4.

[6] M. Golozar, A. Paolella, H. Demers, S. Savoie, G. Girard, N. Delaporte, R. Gauvin, A. Guerfi, H. Lorrmann and K. Zaghib, 'Direct observation of lithium metal dendrites with ceramic solid electrolyte', *Scientific Reports*, vol. 10, no. 1, Dec. 2020. DOI: 10.1038/s41598-020-75456-0.

[7] C. Monroe and J. Newman, 'The Impact of Elastic Deformation on Deposition Kinetics at Lithium/Polymer Interfaces', *Journal of The Electrochemical Society*, vol. 152, no. 2, A396, 2005. DOI: 10.1149/1.1850854.

[8] Y. Tian, Y. Zhou, Y. Liu, C. Zhao, W. Wang and Y. Zhou, 'Formation mechanism of sol-gel synthesized $Li_{7-3x}Al_xLa_3Zr_2O_{12}$ and the influence of abnormal grain growth on ionic conductivity', *Solid State Ionics*, vol. 354, Oct. 2020. DOI: 10.1016/j.ssi.2020.115407.

[9] J. Su, X. Huang, Z. Song, T. Xiu, M. E. Badding, J. Jin and Z. Wen, 'Overcoming the abnormal grain growth in Ga-doped $Li_7La_3Zr_2O_{12}$ to enhance the electrochemical stability against Li metal', *Ceramics International*, vol. 45, no. 12, pp. 14 991–14 996, Aug. 2019. DOI: 10.1016/j.ceramint.2019.04.236.

[10] U. A. Eriksen, 'Sintering and transport properties of Al-LLZO ceramic electrolytes for use in solid-state Li-ion batteries', Tech. Rep., 2021.

[11] J. Leng, Z. Wang, J. Wang, H. H. Wu, G. Yan, X. Li, H. Guo, Y. Liu, Q. Zhang and Z. Guo, 'Advances in nanostructures fabricated: Via spray pyrolysis and their applications in energy storage and conversion', *Chemical Society Reviews*, vol. 48, no. 11, pp. 3015–3072, Jun. 2019. DOI: 10.1039/c8cs00904j.

[12] R. Djenadic, M. Botros, C. Benel, O. Clemens, S. Indris, A. Choudhary, T. Bergfeldt and H. Hahn, 'Nebulized spray pyrolysis of Al-doped $Li_7La_3Zr_2O_{12}$ solid electrolyte for battery applications', *Solid State Ionics*, vol. 263, pp. 49–56, Oct. 2014. DOI: 10.1016/j.ssi.2014.05.007.

[13] M. Nybrodahl, 'The effect of MgO addition on the phase stability of garnet structured solid-state electrolytes with composition $Li_{6.25}Al_{0.25}La_3Zr_2O_{12}$', Tech. Rep., 2021.

[14] R. Murugan, V. Thangadurai and W. Weppner, 'Fast lithium ion conduction in garnet-type $Li_7La_3Zr_2O_{12}$', *Angewandte Chemie - International Edition*, vol. 46, no. 41, pp. 7778–7781, 2007. DOI: 10.1002/anie.200701144.

[15] C. A. Geiger, E. Alekseev, B. Lazic, M. Fisch, T. Armbruster, R. Langner, M. Fechtelkord, N. Kim, T. Pettke and W. Weppner, 'Crystal chemistry and stability of "$Li_7La_3Zr_2O_{12}$" garnet: A fast lithium-ion conductor', *Inorganic Chemistry*, vol. 50, no. 3, pp. 1089–1097, Feb. 2011. DOI: 10.1021/ic101914e.

[16] D. Rettenwander, R. Wagner, J. Langer, M. E. Maier, M. Wilkening and G. Amthauer, 'Crystal chemistry of "$Li_7La_3Zr_2O_{12}$" garnet doped with Al, Ga, and Fe: a short review on local structures as revealed by NMR and Mößbauer spectroscopy studies', *European Journal of Mineralogy*, vol. 28, no. 3, pp. 619–629, Sep. 2016. DOI: 10.1127/ejm/2016/0028-2543.

[17] R. Wagner, G. J. Redhammer, D. Rettenwander, A. Senyshyn, W. Schmidt, M. Wilkening and G. Amthauer, 'Crystal Structure of Garnet-Related Li-Ion Conductor $Li_{7-3x}Ga_xLa_3Zr_2O_{12}$: Fast Li-Ion Conduction Caused by a Different Cubic Modification?', *Chemistry of Materials*, vol. 28, no. 6, pp. 1861–1871, Mar. 2016. DOI: 10.1021/acs.chemmater.6b00038.

[18] S. R. Yeandel, B. J. Chapman, P. R. Slater and P. Goddard, 'Structure and Lithium-Ion Dynamics in Fluoride-Doped Cubic $Li_7La_3Zr_2O_{12}$ (LLZO) Garnet for Li Solid-State Battery Applications', *Journal of Physical Chemistry C*, vol. 122, no. 49, pp. 27 811–27 819, Dec. 2018. DOI: 10.1021/acs.jpcc.8b07704.

[19] M. M. Raju, F. Altayran, M. Johnson, D. Wang and Q. Zhang, 'Crystal Structure and Preparation of $Li_7La_3Zr_2O_{12}$ (LLZO) Solid-State Electrolyte and Doping Impacts on the Conductivity: An Overview', *Electrochem*, vol. 2, no. 3, pp. 390–414, Jul. 2021. DOI: 10.3390/electrochem2030026.

[20] H. Buschmann, J. Dölle, S. Berendts, A. Kuhn, P. Bottke, M. Wilkening, P. Heitjans, A. Senyshyn, H. Ehrenberg, A. Lotnyk, V. Duppel, L. Kienle and J. Janek, 'Structure and dynamics of the fast lithium ion conductor "$Li_7La_3Zr_2O_{12}$"', *Physical Chemistry Chemical Physics*, vol. 13, no. 43, pp. 19 378–19 392, Nov. 2011. DOI: 10.1039/c1cp22108f.

[21] V. Thangadurai, S. Narayanan and D. Pinzaru, 'Garnet-type solid-state fast Li ion conductors for Li batteries: Critical review', *Chemical Society Reviews*, vol. 43, no. 13, pp. 4714–4727, Jul. 2014. DOI: 10.1039/c4cs00020j.

[22] S. Yu, R. D. Schmidt, R. Garcia-Mendez, E. Herbert, N. J. Dudney, J. B. Wolfenstine, J. Sakamoto and D. J. Siegel, 'Elastic Properties of the Solid Electrolyte $Li_7La_3Zr_2O_{12}$ (LLZO)', *Chemistry of Materials*, vol. 28, no. 1, pp. 197–206, Jan. 2016. DOI: 10.1021/acs.chemmater.5b03854.

[23] A. Kim, S. Woo, M. Kang, H. Park and B. Kang, 'Research Progresses of Garnet-Type Solid Electrolytes for Developing All-Solid-State Li Batteries', *Frontiers in Chemistry*, vol. 8, Jun. 2020. DOI: 10.3389/fchem.2020.00468.

[24] Y. Wang and W. Lai, 'Phase transition in lithium garnet oxide ionic conductors $Li_7La_3Zr_2O_{12}$: The role of Ta substitution and $H_2O/CO_2$ exposure', *Journal of Power Sources*, vol. 275, pp. 612–620, Feb. 2015. DOI: 10.1016/j.jpowsour.2014.11.062.

[25] Y. Matsuda, K. Sakamoto, M. Matsui, O. Yamamoto, Y. Takeda and N. Imanishi, 'Phase formation of a garnet-type lithium-ion conductor $Li_{7-3x}Al_xLa_3Zr_2O_{12}$', *Solid State Ionics*, vol. 277, pp. 23–29, Aug. 2015. DOI: 10.1016/j.ssi.2015.04.011.

[26] C. Shao, H. Liu, Z. Yu, Z. Zheng, N. Sun and C. Diao, 'Structure and ionic conductivity of cubic $Li_7La_3Zr_2O_{12}$ solid electrolyte prepared by chemical co-precipitation method', *Solid State Ionics*, vol. 287, pp. 13–16, Apr. 2016. DOI: 10.1016/j.ssi.2016.01.042.

[27] N. Bernstein, M. D. Johannes and K. Hoang, 'Origin of the structural phase transition in $Li_7La_3Zr_2O_{12}$', *Physical Review Letters*, vol. 109, no. 20, Nov. 2012. DOI: 10.1103/PhysRevLett.109.205702.

[28] G. Larraz, A. Orera and M. L. Sanjuán, 'Cubic phases of garnet-type $Li_7La_3Zr_2O_{12}$: The role of hydration', *Journal of Materials Chemistry A*, vol. 1, no. 37, pp. 11 419–11 428, Oct. 2013. DOI: 10.1039/c3ta11996c.

[29] J. Li, Z. Liu, W. Ma, H. Dong, K. Zhang and R. Wang, 'Low-temperature synthesis of cubic phase $Li_7La_3Zr_2O_{12}$ via sol-gel and ball milling induced phase transition', *Journal of Power Sources*, vol. 412, pp. 189–196, Feb. 2019. DOI: 10.1016/j.jpowsour.2018.11.040.

[30] M. Matsui, K. Takahashi, K. Sakamoto, A. Hirano, Y. Takeda, O. Yamamoto and N. Imanishi, 'Phase stability of a garnet-type lithium ion conductor $Li_7La_3Zr_2O_{12}$', *Dalton Transactions*, vol. 43, no. 3, pp. 1019–1024, Jan. 2014. DOI: 10.1039/c3dt52024b.

[31] Y. Chen, E. Rangasamy, C. R. Dela Cruz, C. Liang and K. An, 'A study of suppressed formation of low-conductivity phases in doped $Li_7La_3Zr_2O_{12}$ garnets by in situ neutron diffraction', *Journal of Materials Chemistry A*, vol. 3, no. 45, pp. 22 868–22 876, 2015. DOI: 10.1039/c5ta04902d.

[32] M. R. Bonilla, F. A. García Daza, J. Carrasco and E. Akhmatskaya, 'Exploring Li-ion conductivity in cubic, tetragonal and mixed-phase Al-substituted $Li_7La_3Zr_2O_{12}$ using atomistic simulations and effective medium theory', *Acta Materialia*, vol. 175, pp. 426–435, Aug. 2019. DOI: 10.1016/j.actamat.2019.06.033.

[33] E. Rangasamy, J. Wolfenstine, J. Allen and J. Sakamoto, 'The effect of 24c-site (A) cation substitution on the tetragonal-cubic phase transition in $Li_{7-x}La_{3-x}A_xZr_2O_{12}$ garnet-based ceramic electrolyte', *Journal of Power Sources*, vol. 230, pp. 261–266, 2013. DOI: 10.1016/j.jpowsour.2012.12.076.

[34] W. Xia, B. Xu, H. Duan, Y. Guo, H. Kang, H. Li and H. Liu, 'Ionic Conductivity and Air Stability of Al-Doped $Li_7La_3Zr_2O_{12}$ Sintered in Alumina and Pt Crucibles', *ACS Applied Materials and Interfaces*, vol. 8, no. 8, pp. 5335–5342, Mar. 2016. DOI: 10.1021/acsami.5b12186.

[35] Y. Jin and P. J. McGinn, 'Al-doped $Li_7La_3Zr_2O_{12}$ synthesized by a polymerized complex method', *Journal of Power Sources*, vol. 196, no. 20, pp. 8683–8687, Oct. 2011. DOI: 10.1016/j.jpowsour.2011.05.065.

[36] M. Kotobuki, K. Kanamura, Y. Sato and T. Yoshida, 'Fabrication of all-solid-state lithium battery with lithium metal anode using $Al_2O_3$-added $Li_7La_3Zr_2O_{12}$ solid electrolyte', *Journal of Power Sources*, vol. 196, no. 18, pp. 7750–7754, Sep. 2011. DOI: 10.1016/j.jpowsour.2011.04.047.

[37] E. Rangasamy, J. Wolfenstine and J. Sakamoto, 'The role of Al and Li concentration on the formation of cubic garnet solid electrolyte of nominal composition $Li_7La_3Zr_2O_{12}$', *Solid State Ionics*, vol. 206, pp. 28–32, Jan. 2012. DOI: 10.1016/j.ssi.2011.10.022.

[38] A. G. Squires, D. O. Scanlon and B. J. Morgan, 'Native defects and their doping response in the lithium solid electrolyte $Li_7La_3Zr_2O_{12}$', *ChemRxiv*, 2019. DOI: 10.26434/chemrxiv.9031346.v3.

[39] S. Kim, M. Hirayama, S. Taminato and R. Kanno, 'Epitaxial growth and lithium ion conductivity of lithium-oxide garnet for an all solid-state battery electrolyte', *Dalton Transactions*, vol. 42, no. 36, pp. 13 112–13 117, Sep. 2013. DOI: 10.1039/c3dt51795k.

[40] S. Chen, X. Hu, W. Bao, Z. Wang, Q. Yang, L. Nie, X. Zhang, J. Zhang, Y. Jiang, Y. Han, C. Wan, J. Xie, Y. Yu and W. Liu, 'Low-sintering-temperature garnet oxides by conformal sintering-aid coating', *Cell Reports Physical Science*, vol. 2, no. 9, p. 100 569, Sep. 2021. DOI: 10.1016/j.xcrp.2021.100569.

[41] S. Kumazaki, Y. Iriyama, K. H. Kim, R. Murugan, K. Tanabe, K. Yamamoto, T. Hirayama and Z. Ogumi, 'High lithium ion conductive $Li_7La_3Zr_2O_{12}$ by inclusion of both Al and Si', *Electrochemistry Communications*, vol. 13, no. 5, pp. 509–512, May 2011. DOI: 10.1016/j.elecom.2011.02.035.

[42] H. Xie, J. A. Alonso, Y. Li, M. T. Fernández-Díaz and J. B. Goodenough, 'Lithium distribution in aluminum-free cubic $Li_7La_3Zr_2O_{12}$', *Chemistry of Materials*, vol. 23, no. 16, pp. 3587–3589, Aug. 2011. DOI: 10.1021/cm201671k.

[43] S.-J. L. Kang, *ABNORMAL GRAIN GROWTH*. 2005, pp. 117–135. DOI: https://doi.org/10.1016/B978-075066385-4/50009-1.

[44] C. Zheng, J. Su, Z. Song, T. Xiu, J. Jin, M. E. Badding and Z. Wen, 'Improvement of density and electrochemical performance of garnet-type $Li_7La_3Zr_2O_{12}$ for solid-state lithium metal batteries enabled by W and Ta co-doping strategy', *Materials Today Energy*, p. 101 034, May 2022. DOI: 10.1016/J.MTENER.2022.101034.

[45] S. Sumita, 'Effects of Inorganic Additives on the Isotropic Grain Growth Law of High Purity Alumina', *Journal of the Society of Materials Engineering for Resources of Japan*, vol. 8, no. 1, pp. 71–89, 1995. DOI: https://doi.org/10.5188/jsmerj.8.71.

[46] L. Radonjic and V. Srdic, 'Effect of magnesia on the densification behavior and grain growth of nucleated gel alumina', *Materials Chemistry and Physics*, vol. 47, no. 1, pp. 78–84, 1997. DOI: https://doi.org/10.1016/S0254-0584(97)80032-6.

[47] L. O. Jøsang, *Oral communication: According to M. Tucker via L. O. Jøsang.*

[48] Y. Jiang, X. Zhu, S. Qin, M. Ling and J. Zhu, 'Investigation of $Mg^{2+}$, $Sc^{3+}$ and $Zn^{2+}$ doping effects on densification and ionic conductivity of low-temperature sintered $Li_7La_3Zr_2O_{12}$ garnets', *Solid State Ionics*, vol. 300, 2017. DOI: 10.1016/j.ssi.2016.12.005.

[49] L. J. Miara, W. D. Richards, Y. E. Wang and G. Ceder, 'First-Principles Studies on Cation Dopants and Electrolyte|Cathode Interphases for Lithium Garnets', *Chemistry of Materials*, vol. 27, no. 11, pp. 4040–4047, Jun. 2015. DOI: 10.1021/acs.chemmater.5b01023.

[50] R. D. Shannon, 'Revised effective ionic radii and systematic studies of interatomic distances in halides and chalcogenides', *Acta Crystallographica Section A*, vol. 32, no. 5, pp. 751–767, 1976. DOI: 10.1107/S0567739476001551.

[51] S. Song, M. Kotobuki, F. Zheng, C. Xu, Y. Wang, W. Z. Dong Li, N. Hu, L. Lu, S. Song, C. Xu, N. Hu, M. Kotobuki, F. Zheng, L. Lu, Y. Wang and W. D. Z Li, 'Roles of Alkaline Earth Ions in Garnet-Type Superionic Conductors', *ChemElectroChem*, vol. 4, no. 2, pp. 266–271, Feb. 2017. DOI: 10.1002/CELC.201600639. [Online]. Available: https://onlinelibrary.wiley.com/doi/full/10.1002/celc.201600639%20https://onlinelibrary.wiley.com/doi/abs/10.1002/celc.201600639%20https://chemistry-europe.onlinelibrary.wiley.com/doi/10.1002/celc.201600639.

[52] X. Yang, D. Kong, Z. Chen, Y. Sun and Y. Liu, 'Low-temperature fabrication for transparency Mg doping $Li_7La_3Zr_2O_{12}$ solid state electrolyte', *Journal of Materials Science: Materials in Electronics*, vol. 29, no. 2, pp. 1523–1529, Jan. 2018. DOI: 10.1007/s10854-017-8062-4.

[53] R. A. Jonson, E. Yi, F. Shen and M. C. Tucker, 'Optimization of Tape Casting for Fabrication of $Li_{6.25}Al_{0.25}La_3Zr_2O_{12}$ Sheets', *Energy and Fuels*, vol. 35, no. 10, pp. 8982–8990, May 2021. DOI: 10.1021/acs.energyfuels.1c00566.

[54] X. Huang, Y. Lu, Z. Song, T. Xiu, M. E. Badding and Z. Wen, 'Preparation of dense Ta-LLZO/MgO composite Li-ion solid electrolyte: Sintering, microstructure, performance and the role of MgO', *Journal of Energy Chemistry*, vol. 39, pp. 8–16, Dec. 2019. DOI: 10.1016/j.jechem.2019.01.013.

[55] X. Huang, C. Liu, Y. Lu, T. Xiu, J. Jin, M. E. Badding and Z. Wen, 'A Li-Garnet composite ceramic electrolyte and its solid-state Li-S battery', *Journal of Power Sources*, vol. 382, pp. 190–197, Apr. 2018. DOI: 10.1016/j.jpowsour.2017.11.074.

[56] X. Huang, Y. Lu, J. Jin, S. Gu, T. Xiu, Z. Song, M. E. Badding and Z. Wen, 'Method Using Water-Based Solvent to Prepare $Li_7La_3Zr_2O_{12}$ Solid Electrolytes', *ACS Applied Materials and Interfaces*, vol. 10, no. 20, pp. 17 147–17 155, May 2018. DOI: 10.1021/acsami.8b01961.

[57] J. Lin, L. Wu, Z. Huang, X. Xu and J. Liu, '$La_2zr_2o_7$ and mgo co-doped composite li-garnet solid electrolyte', *Journal of Energy Chemistry*, vol. 40, pp. 132–136, Jan. 2020. DOI: 10.1016/j.jechem.2019.02.003.

[58] H. Guo, J. Su, W. Zha, T. Xiu, Z. Song, M. E. Badding, J. Jin and Z. Wen, 'Achieving high critical current density in Ta-doped $Li_7La_3Zr_2O_{12}$/MgO composite electrolytes', *Journal of Alloys and Compounds*, vol. 856, Mar. 2021. DOI: 10.1016/j.jallcom.2020.157222.

[59] X. Huang, Z. Song, T. Xiu, M. E. Badding and Z. Wen, 'Sintering, micro-structure and $Li^+$ conductivity of $Li_{7x}La_3Zr_{2x}Nb_xO_{12}$/MgO (x=0.2–0.7) Li-Garnet composite ceramics', *Ceramics International*, vol. 45, no. 1, pp. 56–63, Jan. 2019. DOI: 10.1016/j.ceramint.2018.09.133.

[60] K. Ganesh Kumar, P. Balaji Bhargav, C. Balaji, A. Nafis, K. Aravinth and P. Ramasamy, 'Effect of Sintering on Structural Modification and Phase Transition of Al-Substituted LLZO Electrolytes for Solid State Battery Applications', *Journal of Electrochemical Energy Conversion and Storage*, vol. 18, no. 3, Aug. 2021. DOI: 10.1115/1.4049573.

[61] J. M. Weller and C. K. Chan, 'Pyrochlore nanocrystals as versatile quasi-single-source precursors to lithium conducting garnets', *Journal of Materials Chemistry A*, vol. 8, no. 34, pp. 17 405–17 410, Sep. 2020. DOI: 10.1039/d0ta05842d.

[62] C. Deviannapoorani, S. Ramakumar, N. Janani and R. Murugan, 'Synthesis of lithium garnets from $La_2Zr_2O_7$ pyrochlore', *Solid State Ionics*, vol. 283, pp. 123–130, Dec. 2015. DOI: 10.1016/j.ssi.2015.10.006.

[63] U. A. Eriksen, 'Phase stability of LLZO produced by spray pyrolysis for use in solid-state battery technology', Tech. Rep., 2020.

[64] Allan Blackman and Lawrence Gahan, *Aylward and Findlay's SI Chemical data/Allan Blackman; Lawrence Gahan*, 7th ed. John Wiley & Sons Australia, Ltd, 2014.

[65] H. Huo, J. Luo, V. Thangadurai, X. Guo, C. W. Nan and X. Sun, '$Li_2co_3$: a critical issue for developing solid garnet batteries', *ACS Energy Letters*, vol. 5, no. 1, pp. 252–262, Jan. 2020. DOI: 10.1021/acsenergylett.9b02401.

[66] G. Liu, T. Li, Y. Xing and W. Pan, 'Synthesis of $Li_7La_3Zr_2O_{12}$ Solid Electrolyte by Solid Phase Sintering Method', in *IOP Conference Series: Materials Science and Engineering*, vol. 678, IOP Publishing Ltd, Nov. 2019. DOI: 10.1088/1757-899X/678/1/012150.

[67] A. Skokan, 'PHASE STABILITY INVESTIGATIONS IN THE CERAMIC BREEDER SYSTEMS $Li_2O$-$Al_2O_3$ and $Li_2O$-$ZrO_2$', *Fusion Technology 1990*, pp. 772–776, Sep. 1991. DOI: 10.1016/b978-0-444-88508-1.50139-0.

[68] B. P. Dubey, A. Sahoo, V. Thangadurai and Y. Sharma, 'Morphological, dielectric and transport properties of garnet-type $Li_{6.25+y}Al_{0.25}La_3Zr_{2-y}Mn_yO_{12}$ (y = 0, 0.05, 0.1, and 0.2)', *Solid State Ionics*, vol. 351, Aug. 2020. DOI: 10.1016/j.ssi.2020.115339.

[69] V. Avila, B. Yoon, S. Ghose, R. Raj and L. M. Jesus, 'Phase evolution during reactive flash sintering of $Li_{6.25}Al_{0.25}La_3Zr_2O_{12}$ starting from a chemically prepared powder', *Journal of the European Ceramic Society*, vol. 41, no. 8, pp. 4552–4557, Jul. 2021. DOI: 10.1016/j.jeurceramsoc.2021.02.054.

[70] A. I. Waidha, V. Vanita and O. Clemens, 'PEO Infiltration of Porous Garnet-Type Lithium-Conducting Solid Electrolyte Thin Films', *Ceramics*, vol. 4, no. 3, pp. 421–436, Jul. 2021. DOI: 10.3390/ceramics4030031.

[71] A. A. Raskovalov, E. A. Il'Ina and B. D. Antonov, 'Short communication Structure and transport properties of $Li_7La_3Zr_{2-0.75x}Al_xO_{12}$ superionic solid electrolytes', *Journal of Power Sources*, vol. 238, pp. 48–52, 2013. DOI: 10.1016/j.jpowsour.2013.03.049.

[72] E. A. Il'ina, S. V. Pershina, B. D. Antonov, A. A. Pankratov and E. G. Vovkotrub, 'The influence of the glass additive $Li_2O$-$B_2O_3$-$SiO_2$ on the phase composition, conductivity, and microstructure of the $Li_7La_3Zr_2O_{12}$', *Journal of Alloys and Compounds*, vol. 765, pp. 841–847, Oct. 2018. DOI: 10.1016/j.jallcom.2018.06.154.

[73] P. Wakudkar and A. V. Deshpande, 'Effect of $Li_4SiO_4$ addition in $Li_{6.22}Al_{0.16}La_3Zr_{1.7}Ta_{0.3}O_{12}$ garnet type solid electrolyte for lithium ion battery application', *Ceramics International*, vol. 45, no. 16, pp. 20 113–20 120, Nov. 2019. DOI: 10.1016/j.ceramint.2019.06.276.

[74] N. Janani, C. Deviannapoorani, L. Dhivya and R. Murugan, 'Influence of sintering additives on densification and $Li^+$ conductivity of Al doped $Li_7La_3Zr_2O_{12}$ lithium garnet', *RSC Advances*, vol. 4, no. 93, pp. 51 228–51 238, Oct. 2014. DOI: 10.1039/c4ra08674k.

[75] S. Palakkathodi Kammampata and V. Thangadurai, 'Cruising in ceramics—discovering new structures for all-solid-state batteries—fundamentals, materials, and performances', *Ionics*, vol. 24, no. 3, pp. 639–660, Mar. 2018. DOI: 10.1007/s11581-017-2372-7.

[76] S. Kobi, Amardeep, A. Vyas, P. Bhargava and A. Mukhopadhyay, 'Al and Mg Co-Doping Towards Development of Air-Stable and Li-Ion Conducting Li-La-Zirconate Based Solid Electrolyte Exhibiting Low Electrode/Electrolyte Interfacial Resistance', *Journal of The Electrochemical Society*, vol. 167, no. 12, p. 120 519, Aug. 2020. DOI: 10.1149/1945-7111/abad66.

[77] M. A. Braulio, M. Rigaud, A. Buhr, C. Parr and V. C. Pandolfelli, 'Spinel-containing alumina-based refractory castables', *Ceramics International*, vol. 37, no. 6, pp. 1705–1724, Apr. 2011. DOI: 10.1016/j.ceramint.2011.03.049.

[78] X. Huang, Z. Song, T. Xiu, M. E. Badding and Z. Wen, 'Searching for low-cost $Li_xMO_y$ compounds for compensating Li-loss in sintering of Li-Garnet solid electrolyte', *Journal of Materiomics*, vol. 5, no. 2, pp. 221–228, Jun. 2019. DOI: 10.1016/j.jmat.2018.09.004.

[79] Y. Jiang, Y. Zhou, Z. Hu, Y. Huang and X. Zhu, 'MgO or $Al_2O_3$ crucible: Which is better for the preparation of LLZ-based solid electrolytes?', *Ceramics International*, vol. 46, no. 3, pp. 3367–3373, Feb. 2020. DOI: 10.1016/j.ceramint.2019.10.046.

[80] X. Huang, Y. Lu, H. Guo, Z. Song, T. Xiu, M. E. Badding and Z. Wen, 'None-Mother-Powder Method to Prepare Dense Li-Garnet Solid Electrolytes with High Critical Current Density', *ACS Applied Energy Materials*, vol. 1, no. 10, pp. 5355–5365, Oct. 2018. DOI: 10.1021/acsaem.8b00976.

[81] X. Huang, Y. Lu, Z. Song, K. Rui, Q. Wang, T. Xiu, M. E. Badding and Z. Wen, 'Manipulating $Li_2O$ atmosphere for sintering dense $Li_7La_3Zr_2O_{12}$ solid electrolyte', *Energy Storage Materials*, vol. 22, pp. 207–217, Nov. 2019. DOI: 10.1016/j.ensm.2019.01.018.

[82] Y. Ikeda, H. Ito, G. Matsumoto and S. Nasu, 'A Mass Spectrometric Study of Vaporization of $Li_2O$ with Some Refractory Metal Cells', *Journal of the Mass Spectrometry Society of Japan*, vol. 27, no. 4, pp. 263–273, 1979. DOI: https://doi.org/10.5702/massspec1953.27.263.

[83] H. Kudo, C. H. Wu and H. R. Ihle, 'Mass-spectrometric study of the vaporization of $Li_2O$(s) and thermochemistry of gaseous LiO, $Li_2O$, $Li_3O$, and $Li_2O_2$', *Journal of Nuclear Materials*, vol. 78, no. 2, pp. 380–389, 1978. DOI: https://doi.org/10.1016/0022-3115(78)90460-9.

[84] S. Ramakumar, C. Deviannapoorani, L. Dhivya, L. S. Shankar and R. Murugan, 'Lithium garnets: Synthesis, structure, $Li^+$ conductivity, $Li^+$ dynamics and applications', *Progress in Materials Science*, vol. 88, pp. 325–411, Jul. 2017. DOI: 10.1016/j.pmatsci.2017.04.007.

[85] Y. Chen, E. Rangasamy, C. Liang and K. An, 'Origin of High $Li^+$ Conduction in Doped $Li_7La_3Zr_2O_{12}$ Garnets', *Chemistry of Materials*, vol. 27, no. 16, pp. 5491–5494, Aug. 2015. DOI: 10.1021/acs.chemmater.5b02521.

[86] R. Jalem, M. J. Rushton, W. Manalastas, M. Nakayama, T. Kasuga, J. A. Kilner and R. W. Grimes, 'Effects of gallium doping in garnet-type $Li_7La_3Zr_2O_{12}$ solid electrolytes', *Chemistry of Materials*, vol. 27, no. 8, pp. 2821–2831, Apr. 2015. DOI: 10.1021/cm5045122.

[87] J. L. Allen, J. Wolfenstine, E. Rangasamy and J. Sakamoto, 'Effect of substitution (Ta, Al, Ga) on the conductivity of $Li_7La_3Zr_2O_{12}$', *Journal of Power Sources*, vol. 206, pp. 315–319, May 2012. DOI: 10.1016/j.jpowsour.2012.01.131.

[88] S. Ramakumar, N. Janani and R. Murugan, 'Influence of lithium concentration on the structure and $Li^+$ transport properties of cubic phase lithium garnets', *Dalton Transactions*, vol. 44, no. 2, pp. 539–552, Jan. 2015. DOI: 10.1039/c4dt02861a.

[89] D. Gao, R. Wu, P. Chen, T. Hong and J. Cheng, 'Microwave assisted reactive sintering for Al doped $Li_7La_3Zr_2O_{12}$ lithium ion solid state electrolyte', *Materials Research Express*, vol. 6, no. 12, 2019. DOI: 10.1088/2053-1591/ab62ef.

[90] Y. Li, J. T. Han, C. A. Wang, S. C. Vogel, H. Xie, M. Xu and J. B. Goodenough, 'Ionic distribution and conductivity in lithium garnet $Li_7La_3Zr_2O_{12}$', *Journal of Power Sources*, vol. 209, pp. 278–281, Jul. 2012. DOI: 10.1016/j.jpowsour.2012.02.100.

[91] C. Chen, Y. Sun, L. He, M. Kotobuki, E. Hanc, Y. Chen, K. Zeng and L. Lu, 'Microstructural and Electrochemical Properties of Al- And Ga-Doped $Li_7La_3Zr_2O_{12}$ Garnet Solid Electrolytes', *ACS Applied Energy Materials*, vol. 3, no. 5, pp. 4708–4719, May 2020. DOI: 10.1021/acsaem.0c00347.

[92] C. Liu, Z. Y. Wen and K. Rui, 'High ion conductivity in garnet-type F-doped $Li_7La_3Zr_2O_{12}$', *Wuji Cailiao Xuebao/Journal of Inorganic Materials*, vol. 30, no. 9, pp. 995–1001, Sep. 2015. DOI: 10.15541/jim20150163.

[93] Z. Hu, H. Liu, H. Ruan, R. Hu, Y. Su and L. Zhang, 'High Li-ion conductivity of Al-doped $Li_7La_3Zr_2O_{12}$ synthesized by solid-state reaction', *Ceramics International*, vol. 42, no. 10, pp. 12 156–12 160, Aug. 2016. DOI: 10.1016/j.ceramint.2016.04.149.

[94] R. J. Chen, M. Huang, W. Z. Huang, Y. Shen, Y. H. Lin and C. W. Nan, 'Effect of calcining and Al doping on structure and conductivity of $Li_7La_3Zr_2O_{12}$', *Solid State Ionics*, vol. 265, pp. 7–12, Nov. 2014. DOI: 10.1016/j.ssi.2014.07.004.

[95] Y. Kim, H. Jo, J. L. Allen, H. Choe, J. Wolfenstine and J. Sakamoto, 'The Effect of Relative Density on the Mechanical Properties of Hot-Pressed Cubic $Li_7La_3Zr_2O_{12}$', *Journal of the American Ceramic Society*, vol. 99, no. 4, pp. 1367–1374, Apr. 2016. DOI: 10.1111/jace.14084.

[96] H. Buschmann, S. Berendts, B. Mogwitz and J. Janek, 'Lithium metal electrode kinetics and ionic conductivity of the solid lithium ion conductors "$Li_7La_3Zr_2O_{12}$" and $Li_{7-x}La_3Zr_{2-x}Ta_xO_{12}$ with garnet-type structure', *Journal of Power Sources*, vol. 206, pp. 236–244, May 2012. DOI: 10.1016/j.jpowsour.2012.01.094.

[97] M. Huang, T. Liu, Y. Deng, H. Geng, Y. Shen, Y. Lin and C. W. Nan, 'Effect of sintering temperature on structure and ionic conductivity of $Li_{7-x}La_3Zr_2O_{12-0.5x}$ (x = 0.5 0.7) ceramics', *Solid State Ionics*, vol. 204-205, no. 1, pp. 41–45, 2011. DOI: 10.1016/j.ssi.2011.10.003.

[98] I. N. David, T. Thompson, J. Wolfenstine, J. L. Allen and J. Sakamoto, 'Microstructure and Li-ion Conductivity of Hot-Pressed Cubic $Li_7La_3Zr_2O_{12}$', *Journal of the American Ceramic Society*, vol. 98, no. 4, pp. 1209–1214, 2015. DOI: 10.1111/jace.13455.

[99] Y. Zhang, F. Chen, R. Tu, Q. Shen and L. Zhang, 'Field assisted sintering of dense Al-substituted cubic phase $Li_7La_3Zr_2O_{12}$ solid electrolytes', *Journal of Power Sources*, vol. 268, pp. 960–964, Dec. 2014. DOI: 10.1016/j.jpowsour.2014.03.148.

[100] S. Yu and D. J. Siegel, 'Grain Boundary Contributions to Li-Ion Transport in the Solid Electrolyte $Li_7La_3Zr_2O_{12}$ (LLZO)', *Chemistry of Materials*, vol. 29, no. 22, pp. 9639–9647, Nov. 2017. DOI: 10.1021/acs.chemmater.7b02805.

[101] T. Thompson, A. Sharafi, M. D. Johannes, A. Huq, J. L. Allen, J. Wolfenstine and J. Sakamoto, 'A tale of two sites: On defining the carrier concentration in Garnet-based ionic conductors for advanced Li batteries', *Advanced Energy Materials*, vol. 5, no. 11, Jun. 2015. DOI: 10.1002/aenm.201500096.

[102] S. A. Pervez, G. Kim, B. P. Vinayan, M. A. Cambaz, M. Kuenzel, M. Hekmatfar, M. Fichtner and S. Passerini, 'Overcoming the Interfacial Limitations Imposed by the Solid–Solid Interface in Solid-State Batteries Using Ionic Liquid-Based Interlayers', *Small*, vol. 16, no. 14, Apr. 2020. DOI: 10.1002/smll.202000279.

[103] S. I. Abdul Halim, C. H. Chan and J. Apotheker, 'Basics of teaching electrochemical impedance spectroscopy of electrolytes for ion-rechargeable batteries - Part 1: A good practice on estimation of bulk resistance of solid polymer electrolytes', *Chemistry Teacher International*, vol. 3, no. 2, pp. 105–115, Jun. 2021. DOI: 10.1515/cti-2020-0011.

[104] P. Vadhva, J. Hu, M. J. Johnson, R. Stocker, M. Braglia, D. J. Brett and A. J. Rettie, 'Electrochemical Impedance Spectroscopy for All-Solid-State Batteries: Theory, Methods and Future Outlook', *ChemElectroChem*, vol. 8, no. 11, pp. 1930–1947, Jun. 2021. DOI: 10.1002/celc.202100108.

[105] J. T. S. Irvine, D. C. Sinclair and A. R. West, 'Characterization by Impedance Spectroscopy', *Advanced materials*, vol. 2, no. 3, pp. 132–138, 1990.

[106] M. Joshi, 'Importance of Impedance Spectroscopy Technique in Materials Characterization: A Brief Review', *Mechanics, Materials Science Engineering MMSE Journal*, vol. 9, Apr. 2017. DOI: 10.2412/mmse.42.57.345.

[107] Gamry Instruments, 'Basics of Electrochemical Impedance Spectroscopy', (Application Note Rev. 1.0), Tech. Rep., Nov. 2016. [Online]. Available: https://www.gamry.com/application-notes/EIS/basics-of-electrochemical-impedance-spectroscopy/.

[108] P. Braun, C. Uhlmann, A. Weber, H. Störmer, D. Gerthsen and E. Ivers-Tiffée, 'Separation of the bulk and grain boundary contributions to the total conductivity of solid lithium-ion conducting electrolytes', *Journal of Electroceramics*, vol. 38, no. 2-4, pp. 157–167, Jun. 2017. DOI: 10.1007/s10832-016-0061-y.

[109] E. Kuhnert, L. Ladenstein, A. Jodlbauer, C. Slugovc, G. Trimmel, H. M. R. Wilkening and D. Rettenwander, 'Lowering the Interfacial Resistance in $Li_{6.4}La_3Zr_{1.4}Ta_{0.6}O_{12}$|Poly(Ethylene Oxide) Composite Electrolytes', *Cell Reports Physical Science*, vol. 1, no. 10, p. 100 214, Oct. 2020. DOI: 10.1016/J.XCRP.2020.100214.

[110] Y. Lu, X. Huang, Y. Ruan, Q. Wang, R. Kun, J. Yang and Z. Wen, 'An in situ element permeation constructed high endurance Li–LLZO interface at high current densities', *Journal of Materials Chemistry A*, vol. 6, no. 39, pp. 18 853–18 858, Oct. 2018. DOI: 10.1039/C8TA07241H. [Online]. Available: https://pubs.rsc.org/en/content/articlehtml/2018/ta/c8ta07241h%20https://pubs.rsc.org/en/content/articlelanding/2018/ta/c8ta07241h.

[111] F. Shen, M. B. Dixit, X. Xiao and K. B. Hatzell, 'Effect of Pore Connectivity on Li Dendrite Propagation within LLZO Electrolytes Observed with Synchrotron X-ray Tomography', *ACS Energy Letters*, vol. 3, no. 4, pp. 1056–1061, Apr. 2018. DOI: 10.1021/acsenergylett.8b00249.

[112] L. Yang, Q. Dai, L. Liu, D. Shao, K. Luo, S. Jamil, H. Liu, Z. Luo, B. Chang and X. Wang, 'Rapid sintering method for highly conductive $Li_7La_3Zr_2O_{12}$ ceramic electrolyte', *Ceramics International*, vol. 46, no. 8, pp. 10 917–10 924, Jun. 2020. DOI: 10.1016/j.ceramint.2020.01.106.

[113] X. Huang, T. Xiu, M. E. Badding and Z. Wen, 'Two-step sintering strategy to prepare dense Li-Garnet electrolyte ceramics with high $Li^+$ conductivity', *Ceramics International*, vol. 44, no. 5, pp. 5660–5667, Apr. 2018. DOI: 10.1016/j.ceramint.2017.12.217.

[114] Y. Zhang, W. Luo, D. Hu, Y. Deng, Y. Chen and J. Deng, 'Rapid fabrication of $Li_7La_3Zr_2O_{12}$ solid electrolyte with enhanced lithium ionic conductivity by microwave sintering', *International Journal of Electrochemical Science*, vol. 15, pp. 7163–7174, 2020. DOI: 10.20964/2020.08.67.

[115] X. Zeng, A. J. Martinolich, K. A. See and K. T. Faber, 'Dense garnet-type electrolyte with coarse grains for improved air stability and ionic conductivity', *Journal of Energy Storage*, vol. 27, Feb. 2020. DOI: 10.1016/j.est.2019.101128.

[116] Y. Tian, Y. Zhou, W. Wang and Y. Zhou, 'Effects of Ga–Ba Co-doping on the morphology and conductivity of $Li_7La_3Zr_2O_{12}$ electrolyte synthesized by sol-gel method', *Ceramics International*, vol. 48, no. 1, pp. 963–970, Jan. 2022. DOI: 10.1016/j.ceramint.2021.09.181.

[117] M. Hong, Q. Dong, H. Xie, X. Wang, A. H. Brozena, J. Gao, C. Wang, C. Chen, J. Rao, J. Luo and L. Hu, 'Tailoring grain growth and densification toward a high-performance solid-state electrolyte membrane', *Materials Today*, vol. 42, pp. 41–48, Jan. 2021. DOI: 10.1016/j.mattod.2020.10.002.

[118] S. Gates-Rector and T. Blanton, 'The Powder Diffraction File: a quality materials characterization database', *Powder Diffraction*, vol. 34, no. 4, pp. 352–360, Dec. 2019. DOI: 10.1017/S0885715619000812.

[119] B. H. Toby, ' R factors in Rietveld analysis: How good is good enough? ', *Powder Diffraction*, vol. 21, no. 1, pp. 67–70, Mar. 2006. DOI: 10.1154/1.2179804.

# Appendices

## A Pellet masses, dimensions and densities

The measured masses and dimensions of the green pellets and sintered pellets are given in Table A.1. The initial and final densities of the pellets are also listed, which were calculated using Equation A.1 and Equation A.2, respectively.

$$\rho_i = \frac{m_i}{V_i} = \frac{m_i}{\pi \cdot (\frac{d_i}{2})^2 \cdot t_i} \tag{A.1}$$

$$\rho_f = \frac{m_f}{V_f} = \frac{m_f}{\pi \cdot (\frac{d_f}{2})^2 \cdot t_f} \tag{A.2}$$

**Table A.1:** Masses, dimensions and densities of green pellets and sintered pellets. $m_i$ = Initial mass, $t_i$ = Initial thickness, $d_i$ = Initial diameter, $\rho_i$ = Initial green body density, $m_f$ = Final sintered mass, $t_f$ = Final sintered thickness, $d_f$ = Final sintered diameter, $\rho_f$ = Final sintered density.

| Parameter | Sample info | | |
|---|---|---|---|
| | P-1150 °C@1h/M | | |
| | 0 MgO – LALZO | 1 MgO – LALZO | 5 MgO – LALZO |
| $m_i$ [mg] | 596.7 | 620.5 | 589.4 |
| $t_i$ [mm] | 2.84 | 2.86 | 2.81 |
| $d_i$ [mm] | 9.87 | 9.92 | 9.82 |
| $\rho_\mathrm{i}$ [g/cm$^3$] | 2.75 | 2.81 | 2.77 |
| $m_f$ [mg] | 529.7 | 555.0 | 529.6 |
| $t_f$ [mm] | 2.30 | 2.39 | 2.27 |
| $d_f$ [mm] | 8.04 | 8.17 | 8.01 |
| $\rho_\mathrm{f}$ [g/cm$^3$] | 4.54 | 4.43 | 4.63 |
| | P-1200 °C@1h/M | | |
| | 0 MgO – LALZO | 1 MgO – LALZO | 5 MgO – LALZO |
| $m_i$ [mg] | 618.2 | 632.8 | 602.5 |
| $t_i$ [mm] | 2.92 | 2.93 | 2.86 |
| $d_i$ [mm] | 9.90 | 9.91 | 9.82 |
| $\rho_\mathrm{i}$ [g/cm$^3$] | 2.75 | 2.80 | 2.78 |
| $m_f$ [mg] | 547.3 | 561.0 | 538.2 |
| $t_f$ [mm] | 2.44 | 2.46 | 2.37 |
| $d_f$ [mm] | 8.10 | 8.24 | 8.05 |
| $\rho_\mathrm{f}$ [g/cm$^3$] | 4.35 | 4.28 | 4.46 |

| Parameter | Sample info | | |
|---|---|---|---|
| | P-1150 °C@1h/A | | |
| | 0 MgO – LALZO | 1 MgO – LALZO | 5 MgO – LALZO |
| $m_i$ [mg] | 592.2 | 603.1 | 569.3 |
| $t_i$ [mm] | 2.81 | 2.83 | 2.69 |
| $d_i$ [mm] | 9.88 | 9.84 | 9.86 |
| $\rho_{\mathrm{i}}$ [g/cm$^3$] | 2.75 | 2.80 | 2.77 |
| $m_f$ [mg] | 506.4 | 525.8 | 506.4 |
| $t_f$ [mm] | 2.24 | 2.34 | 2.24 |
| $d_f$ [mm] | 8.14 | 8.17 | 8.14 |
| $\rho_{\mathrm{f}}$ [g/cm$^3$] | 4.34 | 4.29 | 4.34 |
| | P-1150 °C@6h/A | | |
| | 0 MgO – LALZO | 1 MgO – LALZO | 5 MgO – LALZO |
| $m_i$ [mg] | 611.5 | 597.8 | 585.7 |
| $t_i$ [mm] | 2.86 | 2.80 | 2.82 |
| $d_i$ [mm] | 9.87 | 9.91 | 9.81 |
| $\rho_{\mathrm{i}}$ [g/cm$^3$] | 2.79 | 2.77 | 2.75 |
| $m_f$ [mg] | 543.4 | 534.9 | 514.6 |
| $t_f$ [mm] | 2.36 | 2.29 | 2.32 |
| $d_f$ [mm] | 8.13 | 8.20 | 8.16 |
| $\rho_{\mathrm{f}}$ [g/cm$^3$] | 4.44 | 4.42 | 4.24 |
| | M-1150 °C@1h/M | | |
| | 0 MgO – LALZO | 1 MgO – LALZO | 5 MgO – LALZO |
| $m_i$ [mg] | 661.8 | 608.9 | 606.4 |
| $t_i$ [mm] | 2.75 | 3.02 | 2.97 |
| $d_i$ [mm] | 9.94 | 9.92 | 9.90 |
| $\rho_{\mathrm{i}}$ [g/cm$^3$] | 2.87 | 2.61 | 2.65 |
| $m_f$ [mg] | 549.3 | 537.6 | 539.7 |
| $t_f$ [mm] | 2.31 | 2.47 | 2.42 |
| $d_f$ [mm] | 8.28 | 8.11 | 8.06 |
| $\rho_{\mathrm{f}}$ [g/cm$^3$] | 4.42 | 4.21 | 4.37 |

| Parameter | Sample info | | |
|---|---|---|---|
| | M-1150 °C@6h/M | | |
| | 0 MgO – LALZO | 1 MgO – LALZO | 5 MgO – LALZO |
| $m_i$ [mg] | 625.8 | 612.8 | 622.2 |
| $t_i$ [mm] | 2.80 | 3.06 | 3.01 |
| $d_i$ [mm] | 9.96 | 9.88 | 9.91 |
| $\rho_\mathrm{i}$ [g/cm$^3$] | 2.87 | 2.61 | 2.68 |
| $m_f$ [mg] | 558.5 | 524.5 | 522.3 |
| $t_f$ [mm] | 2.32 | 2.43 | 2.39 |
| $d_f$ [mm] | 8.25 | 7.95 | 7.92 |
| $\rho_\mathrm{f}$ [g/cm$^3$] | 4.50 | 4.35 | 4.44 |
| | E-1150 °C@1h/M | | |
| | 0 MgO – LALZO | 1 MgO – LALZO | 5 MgO – LALZO |
| $m_i$ [mg] | 603.1 | 601.4 | 592.9 |
| $t_i$ [mm] | 2.77 | 2.95 | 2.91 |
| $d_i$ [mm] | 9.88 | 9.92 | 9.94 |
| $\rho_\mathrm{i}$ [g/cm$^3$] | 2.84 | 2.64 | 2.63 |
| $m_f$ [mg] | 541.2 | 529.1 | 524.7 |
| $t_f$ [mm] | 2.31 | 2.41 | 2.35 |
| $d_f$ [mm] | 8.17 | 8.12 | 8.05 |
| $\rho_\mathrm{f}$ [g/cm$^3$] | 4.47 | 4.24 | 4.39 |
| | E-1150 °C@6h/M | | |
| | 0 MgO – LALZO | 1 MgO – LALZO | 5 MgO – LALZO |
| $m_i$ [mg] | 643.3 | 682.0 | 631.3 |
| $t_i$ [mm] | 2.99 | 3.15 | 2.98 |
| $d_i$ [mm] | 9.83 | 9.89 | 9.83 |
| $\rho_\mathrm{i}$ [g/cm$^3$] | 2.83 | 2.82 | 2.79 |
| $m_f$ [mg] | 544.0 | 571.1 | 524.2 |
| $t_f$ [mm] | 2.46 | 2.53 | 2.40 |
| $d_f$ [mm] | 8.00 | 8.05 | 7.97 |
| $\rho_\mathrm{f}$ [g/cm$^3$] | 4.40 | 4.44 | 4.38 |

The masses of the different pellets after sintering and during density measurements using Archimedes' method are given in Table A.2. The immersion liquid chosen for the density measurements was isopropanol, due to its inertness to LALZO.

The theoretical density of the different pellet stoichiometries was calculated using Equation A.3

$$\rho_{t,LALZO} = \frac{8M_{LALZO}}{N_A a^3} = 8\frac{6.25M_{Li} + 0.25M_{Al} + 3M_{La} + 2M_{Zr} + 12M_O + xM_{Mg}}{N_A(12.963285 \cdot 10^{-8})^3} \tag{A.3}$$

where $M_i$ is the molar mass of specie $i$, $N_A$ is Avagadro's number and $a$ is the lattice constant determined from the unit cell volume based on Rietveld refinement of LALZO from the PDF-database. $x$ is the number of moles of the MgO-addition, when assuming that MgO exists as a separate phase. The stoichiometries and the calculated theoretical densities of the MgO-added pellets, $Li_{6.25}Al_{0.25}La_3Zr_2O_{12}(MgO)_x$, are as follows:

$$0\,\text{MgO}-\text{LALZO} : Li_{6.25}Al_{0.25}La_3Zr_2O_{12} \Rightarrow \rho_{t,0MgO-LALZO} = 5.130\text{g/cm}^3$$
$$1\,\text{MgO}-\text{LALZO} : Li_{6.25}Al_{0.25}La_3Zr_2O_{12}(MgO)_{0.24} \Rightarrow \rho_{t,0MgO-LALZO} = 5.166\text{g/cm}^3$$
$$5\,\text{MgO}-\text{LALZO} : Li_{6.25}Al_{0.25}La_3Zr_2O_{12}(MgO)_{1.24} \Rightarrow \rho_{t,0MgO-LALZO} = 5.314\text{g/cm}^3$$

The bulk densities, $\rho_b$, are calculated by using Equation A.4. The relative density can be described as the ratio of the bulk density to the theoretical reference density.

$$\rho_b = \frac{m_{dry}}{m_{wet} - m_{sub}} \cdot (-0.0009T + 0.8018) \Rightarrow RD = \frac{\rho_b}{\rho_t} \tag{A.4}$$

where $m_{dry}$ is the dry pellet mass after sintering, $m_{sub}$ is the mass while submerged in isopropanol, $m_{wet}$ is the mass with isopropanol in open pores and $T_{iso}$ is the temperature of isopropanol. The obtained bulk densities and relative densities are also listed in Table A.2.

**Table A.2:** Measurements of various sintered pellet masses, during Archimedes' method. $m_{dry}$ = Dry mass after sintering, $m_{sub}$ = Mass while submerged in isopropanol, $m_{wet}$ = Mass with isopropanol in open pores and $T_{sub}$ = Temperature of isopropanol. The bulk density, $\rho_b$, and the relative density, $RD$, is also included.

| Parameter | Sample info | | |
|---|---|---|---|
| | P-1150 °C@1h/M | | |
| | 0 MgO – LALZO | 1 MgO – LALZO | 5 MgO – LALZO |
| $m_{dry}$ [mg] | 529.7 | 555.0 | 538.2 |
| $m_{sub}$ [mg] | 442.4 | 462.7 | 442.2 |
| $m_{wet}$ [mg] | 532.6 | 556.7 | 531.5 |
| $T_{iso}$ [°C] | 19.0 | 19.0 | 19.0 |
| $\rho_b$ [g/cm$^3$] | 4.61 | 4.63 | 4.65 |
| $RD$ [%] | 89.8 | 89.7 | 87.6 |

| Parameter | Sample info | | |
|---|---|---|---|
| | P-1200 °C@1h/M | | |
| | 0 MgO – LALZO | 1 MgO – LALZO | 5 MgO – LALZO |
| $m_{dry}$ [mg] | 547.3 | 561.0 | 538.2 |
| $m_{sub}$ [mg] | 445.6 | 467.6 | 448.7 |
| $m_{wet}$ [mg] | 547.9 | 561.5 | 539.5 |
| $T_{iso}$ [°C] | 17.5 | 17.5 | 17.8 |
| $\rho_b$ [g/cm$^3$] | 4.66 | 4.70 | 4.66 |
| $RD$ [%] | 90.9 | 90.9 | 87.6 |
| | P-1150 °C@1h/A | | |
| | 0 MgO – LALZO | 1 MgO – LALZO | 5 MgO – LALZO |
| $m_{dry}$ [mg] | 525.8 | 538.6 | 506.4 |
| $m_{sub}$ [mg] | 438.2 | 448.7 | 426.4 |
| $m_{wet}$ [mg] | 527.1 | 539.9 | 512.1 |
| $T_{iso}$ [°C] | 19.0 | 16.5 | 16.0 |
| $\rho_b$ [g/cm$^3$] | 4.64 | 4.65 | 4.64 |
| $RD$ [%] | 90.4 | 90.1 | 87.3 |
| | P-1150 °C@6h/A | | |
| | 0 MgO – LALZO | 1 MgO – LALZO | 5 MgO – LALZO |
| $m_{dry}$ [mg] | 543.4 | 534.9 | 514.6 |
| $m_{sub}$ [mg] | 452.9 | 445.6 | 431.6 |
| $m_{wet}$ [mg] | 544.4 | 536.9 | 519.8 |
| $T_{iso}$ [°C] | 17.0 | 17.0 | 17.0 |
| $\rho_b$ [g/cm$^3$] | 4.67 | 4.61 | 4.59 |
| $RD$ [%] | 91.0 | 89.2 | 86.4 |
| | M-1150 °C@1h/M | | |
| | 0 MgO – LALZO | 1 MgO – LALZO | 5 MgO – LALZO |
| $m_{dry}$ [mg] | 549.3 | 537.6 | 539.7 |
| $m_{sub}$ [mg] | 456.8 | 446.1 | 448.6 |
| $m_{wet}$ [mg] | 552.1 | 538.1 | 541.2 |
| $T_{iso}$ [°C] | 17.5 | 17.5 | 17.5 |
| $\rho_b$ [g/cm$^3$] | 4.53 | 4.59 | 4.58 |
| $RD$ [%] | 88.3 | 88.9 | 86.2 |

| Parameter | Sample info | | |
|---|---|---|---|
| | M-1150 °C@6h/M | | |
| | 0 MgO – LALZO | 1 MgO – LALZO | 5 MgO – LALZO |
| $m_{dry}$ [mg] | 558.5 | 524.5 | 522.3 |
| $m_{sub}$ [mg] | 465.8 | 437.7 | 437.4 |
| $m_{wet}$ [mg] | 561.6 | 528.3 | 527.2 |
| $T_{iso}$ [°C] | 19.0 | 18.7 | 18.7 |
| $\rho_b$ [g/cm$^3$] | 4.57 | 4.54 | 4.57 |
| $RD$ [%] | 89.2 | 87.9 | 85.9 |
| | E-1150 °C@1h/M | | |
| | 0 MgO – LALZO | 1 MgO – LALZO | 5 MgO – LALZO |
| $m_{dry}$ [mg] | 541.2 | 529.1 | 524.7 |
| $m_{sub}$ [mg] | 450.3 | 438.8 | 435.8 |
| $m_{wet}$ [mg] | 544.7 | 530.4 | 525.7 |
| $T_{iso}$ [°C] | 17.0 | 17.0 | 17.0 |
| $\rho_b$ [g/cm$^3$] | 4.51 | 4.54 | 4.59 |
| $RD$ [%] | 87.9 | 87.9 | 86.4 |
| | E-1150 °C@6h/M | | |
| | 0 MgO – LALZO | 1 MgO – LALZO | 5 MgO – LALZO |
| $m_{dry}$ [mg] | 544.0 | 571.1 | 524.2 |
| $m_{sub}$ [mg] | 456.8 | 479.1 | 441.3 |
| $m_{wet}$ [mg] | 550.8 | 578.3 | 532.8 |
| $T_{iso}$ [°C] | 18.0 | 18.5 | 18.5 |
| $\rho_b$ [g/cm$^3$] | 4.54 | 4.52 | 4.50 |
| $RD$ [%] | 88.5 | 87.5 | 84.6 |

# B XRD diffractograms

## B.1 Precursor powders + calcined powders

The XRD diffractograms for the as-sprayed precursor powders is shown in Figure B.1, and was measured via XRD by Nybrodahl [13]. From these plots, three phases were identified and indexed to be c-LALZO, pyrochlore ($La_2Zr_2O_7$) and $Li_2CO_3$. Calcination of 750 °C was applied in order to decompose the secondary phases and promote formation of phase pure c-LALZO.

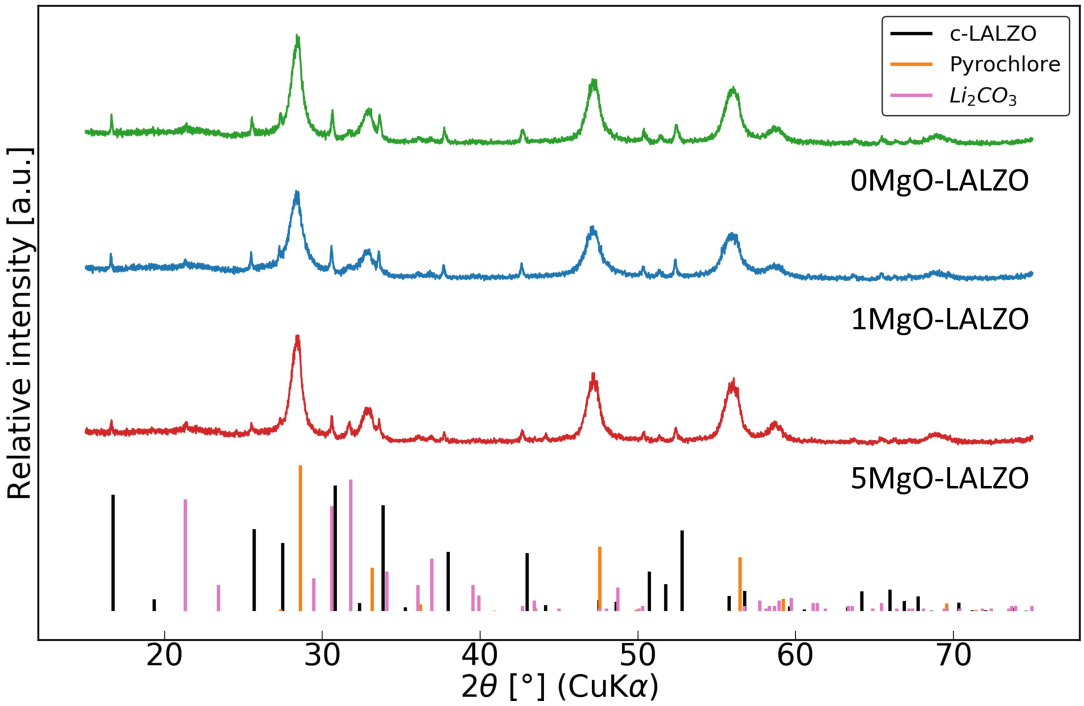


**Figure B.1:** Diffractograms of as-sprayed MgO-added LALZO precursor powders. All peaks belong to c-LALZO, pyrochlore or $Li_2CO_3$. Previously measured by Nybrodahl [13].

The XRD-patterns of the various calcined powder stoichiometries are shown in Figure B.2, and are derived from previous measurements conducted in the specialization project by Nybrodahl [13]. Calcinations were carried out at 750 °C for 6 h, using $Al_2O_3$-crucibles (same dimensions as described in Table 3.3) and batch sizes of 0.2 g. The patters show that the calcined powders consists of purely c-LALZO. No peak splitting splitting can be observed, meaning no t-LALZO is present. No reflections can be found for any intermediate phases. This means that the pyrochlore and $Li_2CO_3$ observed in the precursor powders have fully reacted.

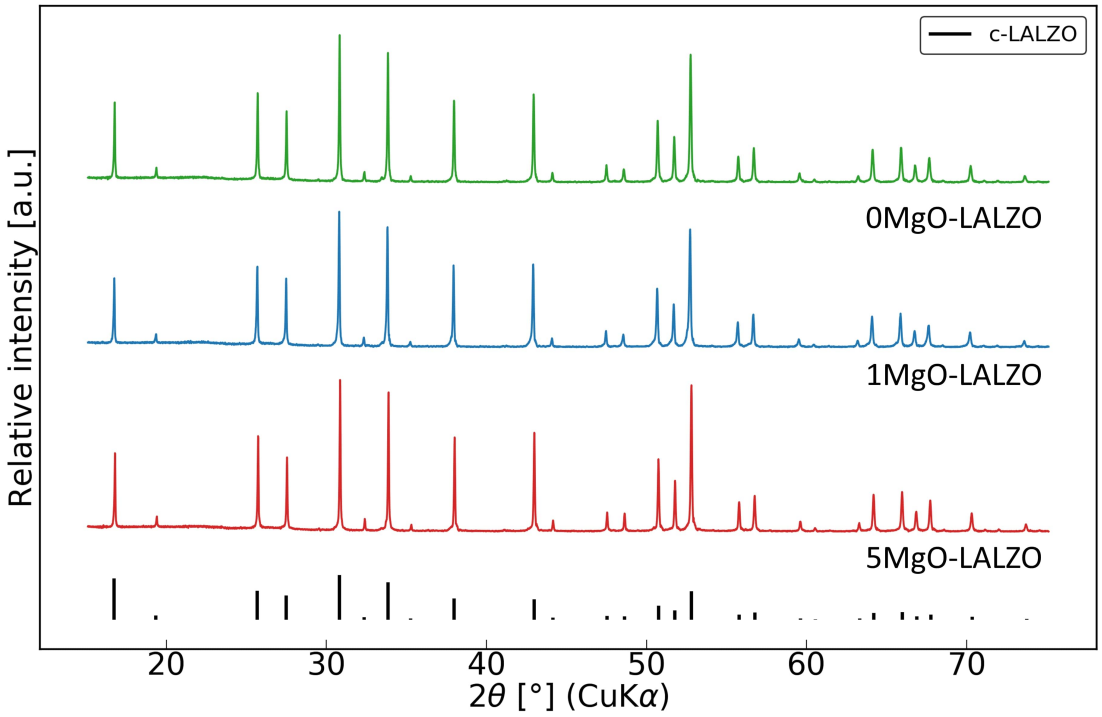


**Figure B.2:** Diffraction patterns of MgO-added LALZO powders calcined at 750 °C for 6 h. All peaks belong to c-LALZO and no intermediate phases can be detected, indicating a single phase c-LALZO powder. As previously measured by Nybrodahl [13].

## B.2 Crucible comparison study

In order to study the effect of crucible material and calcination holding time on the phase purity of calcined powders, 5 MgO–LALZO powders were calcined at 750 °C using different crucible materials ($Al_2O_3$ and MgO) and calcination holding times (6 h and 12 h). Information regarding the crucibles are summarized in Table 3.3. The batch sizes calcined in the $Al_2O_3$ was ∼0.2 g, while the batch sizes calcined in the MgO was ∼4 g. Figure B.3 shows the resulting XRD diffractograms of the different calcined powders. In terms of the phase purity, 6 h is sufficient to achieve single-phase c-LALZO when using the $Al_2O_3$-crucibles. A holding time of 12 h results in a mixture of t-LALZO and c-LALZO. When using the MgO-crucibles, 12 h was necessary in order to obtain single-phase c-LALZO.

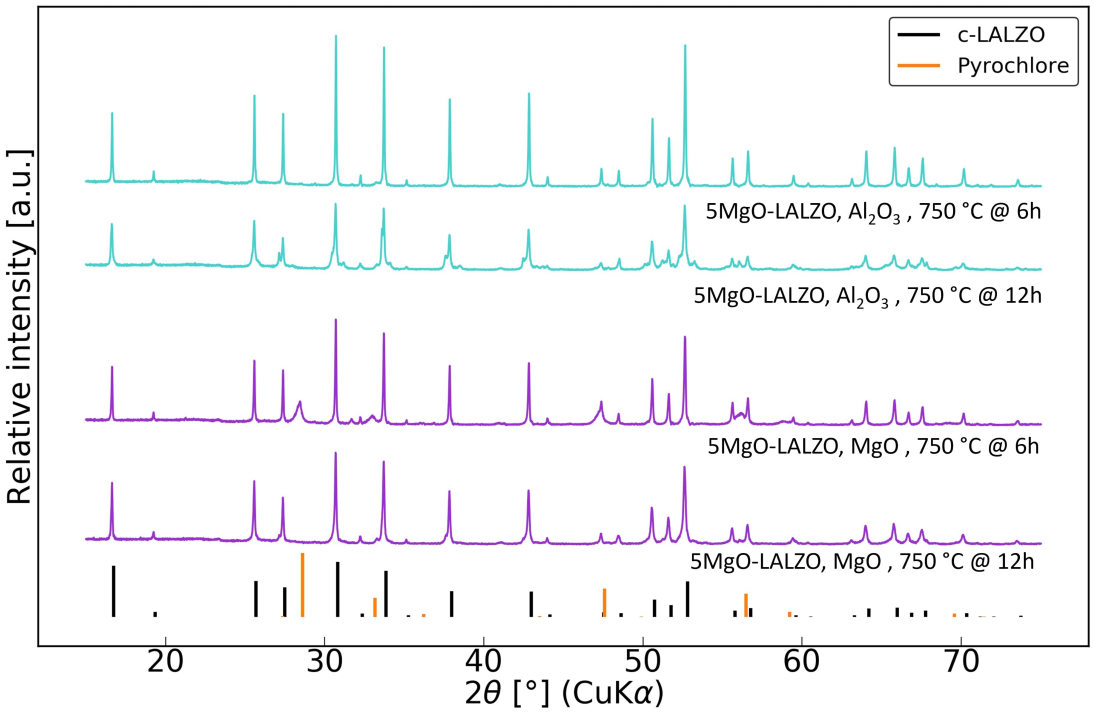


**Figure B.3:** Diffractograms of 5 MgO–LALZO-powders calcined at 750 °C using different crucible materials ($Al_2O_3$ and MgO) and calcination durations (6 h and 12 h).

## B.3 Bedpowders

The XRD diffractogram for the 0 MgO – LALZO bedpowder, calcined at 800 °C for 12 h using a MgO-crucible, is shown in Figure B.4. The diffractogram represents one of the calcined bedpowders, but is representative for all bedpowders produced in this work. The final powders consisted of a mixture of c-LALZO and t-LALZO, as evident from the peak splitting. The choice of this temperature was done in order to produce a c-LALZO/t-LALZO mixed bedpowder, since t-LALZO will provide additional Li and thus further limit the Li-loss. The 0 MgO – LALZO stoichiometry was chosen for the bedpowders, in order to avoid Mg-contamination of Mg-free samples.

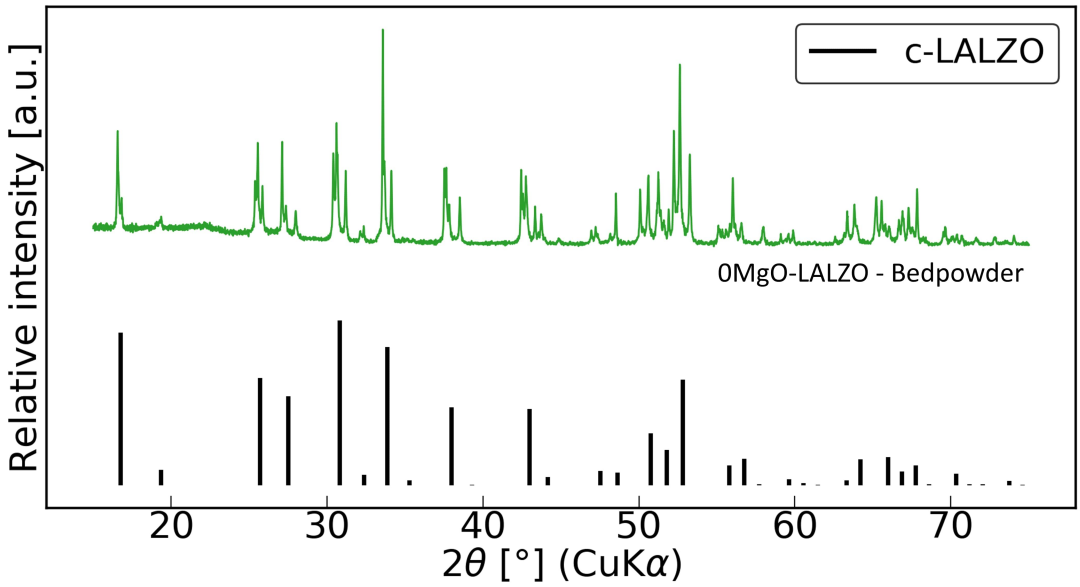


**Figure B.4:** Diffractogram of 0 MgO – LALZO bedpowders calcined at 800 °C for 12 h. The powder consists of a mixture of c-LALZO and t-LALZO, as evident from the peak splitting.

## B.4 Dilatometry

The XRD diffractograms for powders calcined at 750 °C for 6 h in $Al_2O_3$-crucibles, that was used to produce pellets for the dilatometry experiments, are shown in Figure B.5. The powders consists of a mix of c-LALZO and t-LALZO, as evident from the peak splitting. This is however not the case for the 5 MgO – LALZO powder, which show no peak splitting and consists of purely c-LALZO. Other intermediate phases, such as pyrochlore, was not detected and have thus fully reacted. The XRD diffractograms for the pellets after the dilatometry experiments are shown in Figure B.6. The annotations "as received" refer to the pristine pellet surface after sintering. "Polished" refer to the surface of the pellet after being polished, giving a representation of the bulk of the pellet.

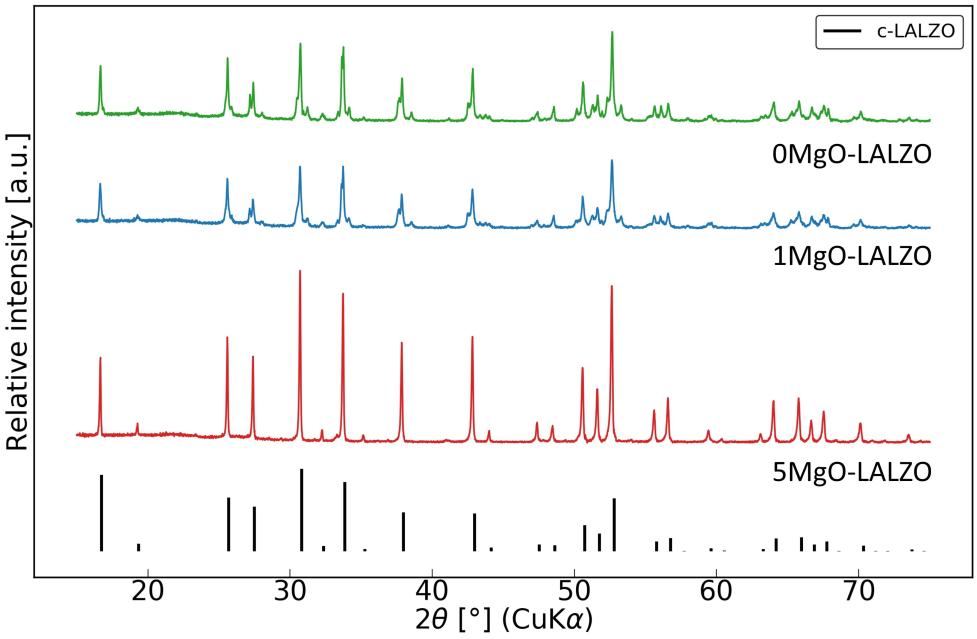


**Figure B.5:** Diffractograms of powders calcined at 750 °C for 6 h, used to make pellets for the dilatometry experiments.

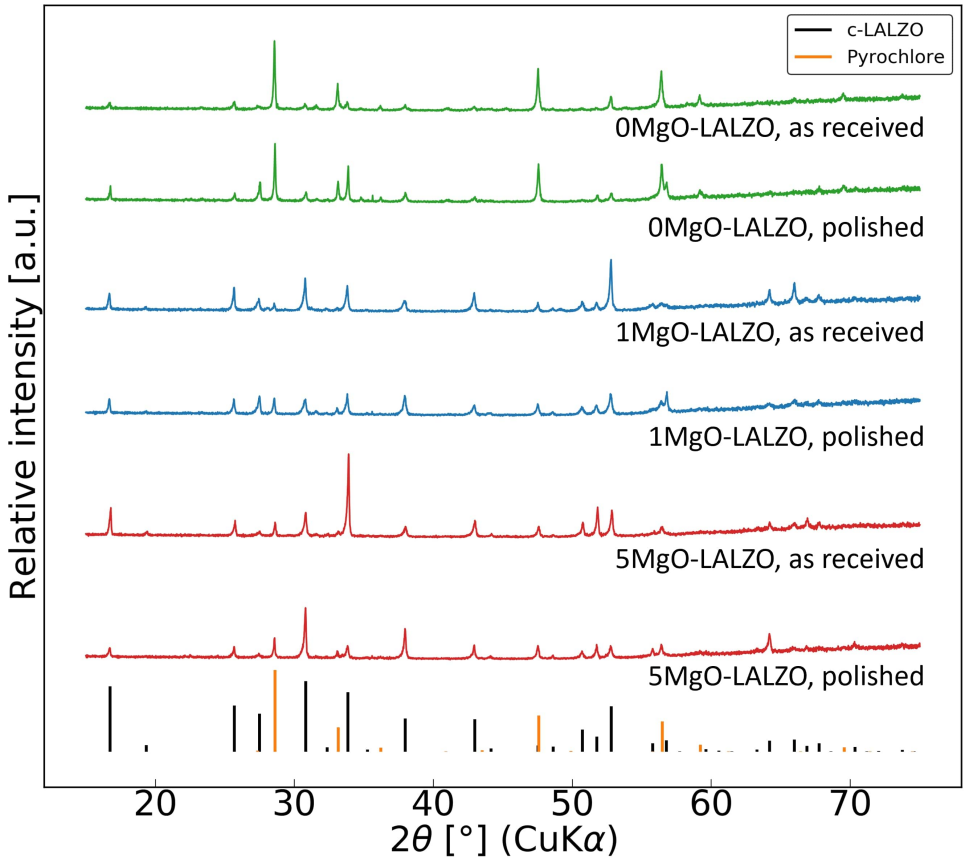


**Figure B.6:** Diffractograms of powders pellets after dilatometry experiments, consisting of dynamic heating to 1250 °C, followed by a 1 h isothermal step. "As received" refer to the pristine pellet surface after sintering, while "Polished" refer to the surface of the pellet after being polished.

## B.5 Intermediate phases

Figure B.7 and Figure B.8 shows the diffraction patterns of the samples sintered during the main sintering experiments, with insets displaying a magnified section of some of the main peaks belonging to the $Li_4SiO_4$-impurity phase and LALO-intermediate phase.

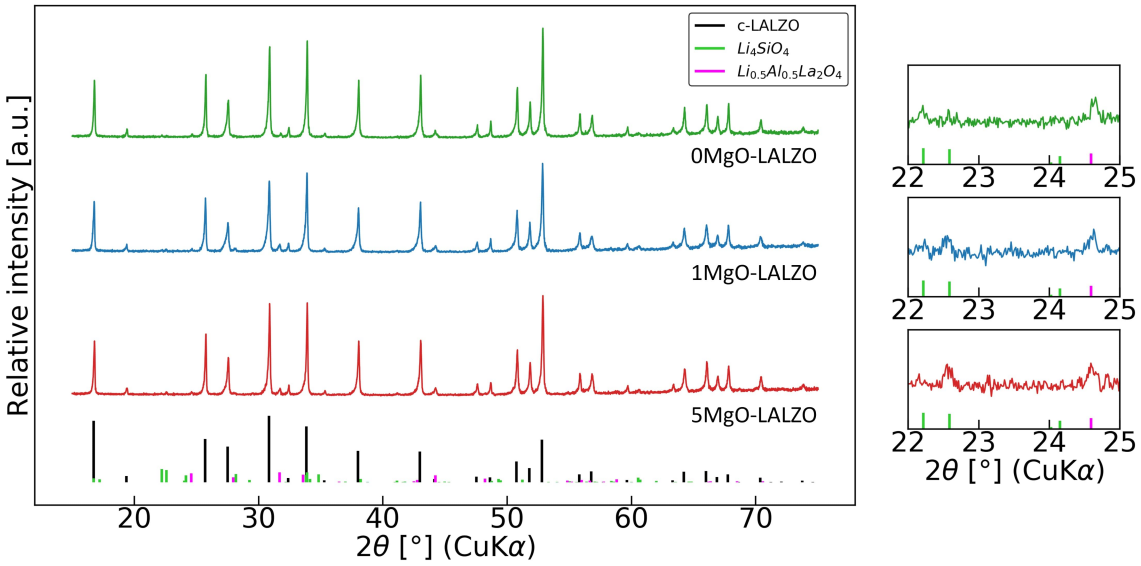


**Figure B.7:** Bulk representative diffractograms of the samples sintered at 1150 °C for 1 h (M-1150 °C@1h/M). The insets on the right displays a magnification of some of the main peaks for the $Li_4SiO_4$-impurity phase and the LALO-intermediate phase.

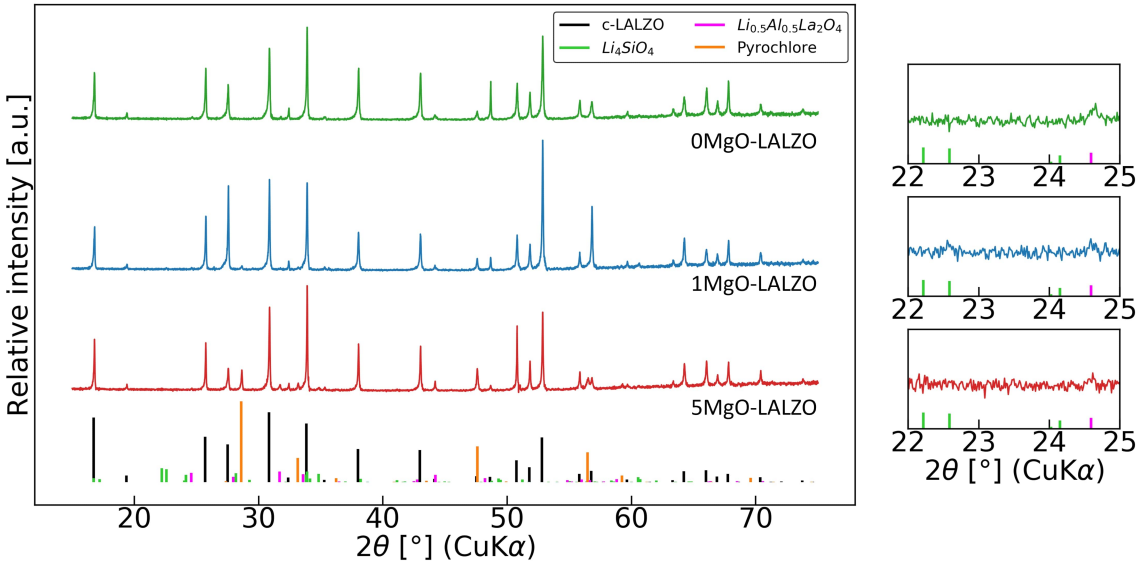


**Figure B.8:** Bulk representative diffractograms of the samples sintered at 1150 °C for 6 h (M-1150 °C@6h/M). The insets on the right displays a magnification of some of the main peaks for the $Li_4SiO_4$-impurity phase and the LALO-intermediate phase.

### B.6 As received vs. polished surfaces

Figure B.9 and Figure B.10 shows a comparison of the diffraction pattern of the as received pellet surface vs. the polished pellet surface of the 5 MgO – LALZO pellet sintered at 1150 °C for 1 h (M-1150 °C@1h/M) and 6 h (M-1150 °C@6h/M), respectively. This figure illustrates how the phase purity at the surface differs slightly from the bulk, with a decrease in peak intensity being observed for the secondary phases. The appearance of the pyrochlore-intermediate phase was also observed upon polishing for the samples sintered with M-1150 °C@6h/M.

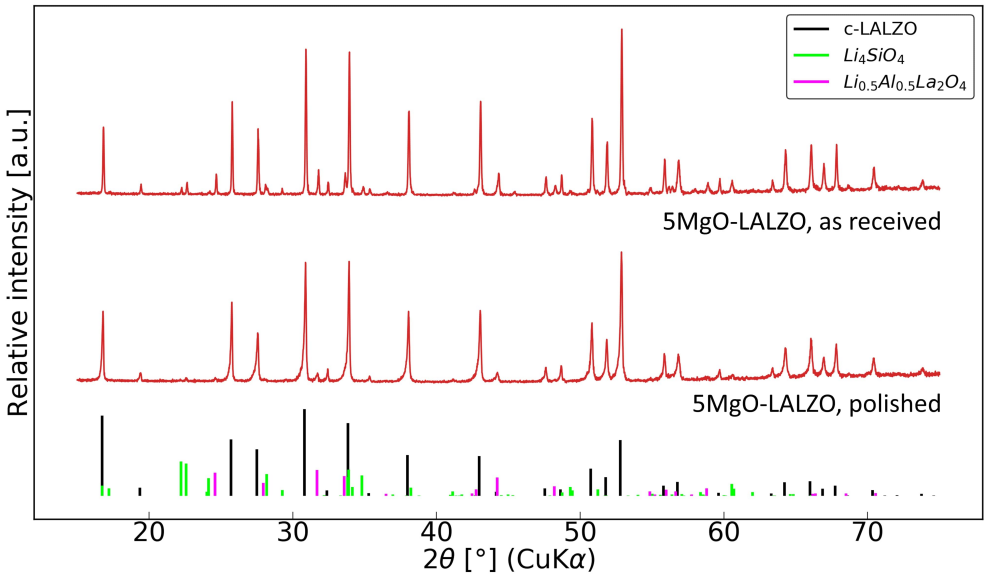


**Figure B.9:** Comparison of the diffraction patterns of the as received and polished pellet surfaces of 5 MgO – LALZO pellets sintered at 1150 °C for 1h (M-1150 °C@1h/M).

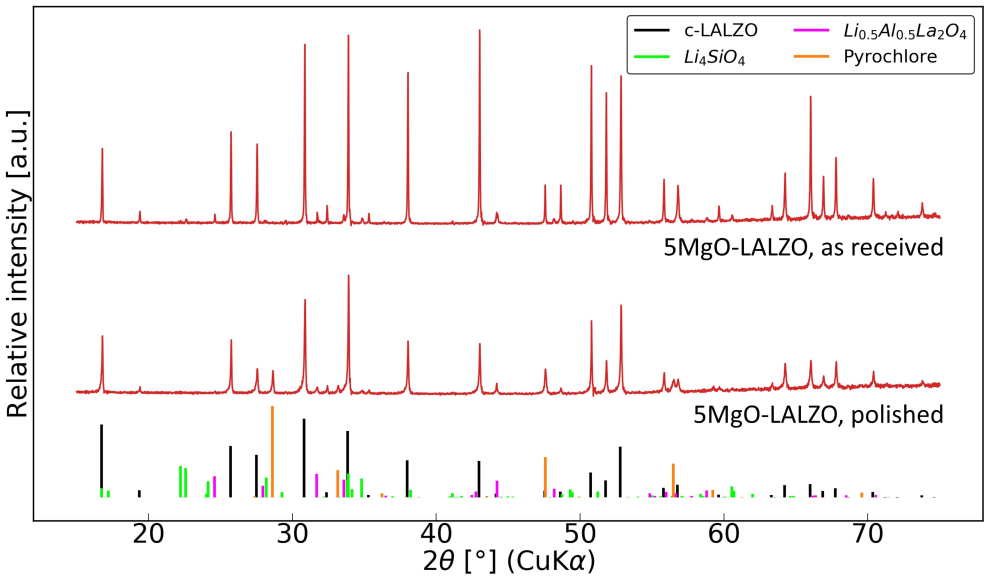


**Figure B.10:** Comparison of the diffraction patterns of the as received and polished pellet surfaces of 5 MgO – LALZO pellets sintered at 1150 °C for 6h (M-1150 °C@6h/M).

# C Preliminary sintering experiments

The preliminary sintering experiments consisted of four different sintering programs:

- P-1150 °C@1h/M
- P-1200 °C@1h/M
- P-1150 °C@1h/A
- P-1150 °C@6h/A

The sintering programs are described in detail in Table 3.5, including sintering temperature and time, BP-ratio and crucible material.

The diffraction patterns for all powder compositions, for the given sintering programs are shown in Figure C.1, Figure C.2, Figure C.3 and Figure C.4, respectively.

As evident from Figure C.1 and Figure C.2, using a BP-ratio = 0.5 results in residual pyrochlore. In addition, low intensity peaks belonging to the $Li_4SiO_4$-impurity phase and LALO-intermediate phase are also present for both sintering programs. The results illustrates the importance of utilizing enough bedpowder, in order to suppress Li-loss.

Figure C.3 and Figure C.4 show that both sintering programs produce near-phase pure c-LALZO. Pyrochlore formation have been avoided, as a result of the utilization of a sufficient BP-ratios. The presence of low intensity peaks belonging to the $Li_4SiO_4$-impurity phase and LALO-intermediate phase is also the case for these sintering programs. Using $Al_2O_3$-crucibles was ultimately ruled out, as using inert crucibles like MgO is more desirable in order to avoid reactions with the crucible.

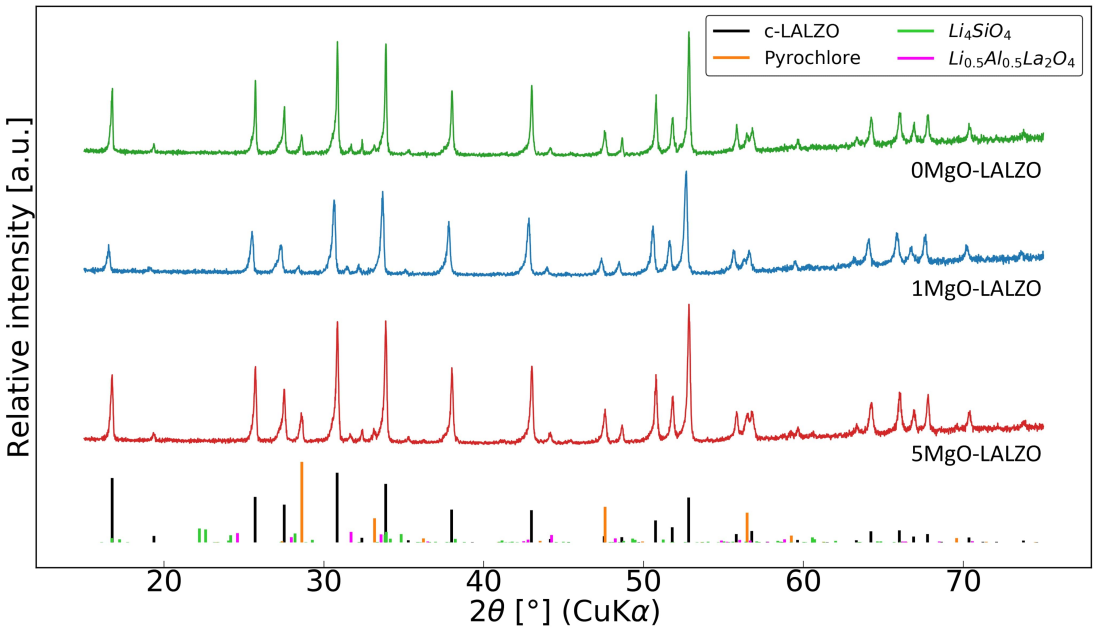


**Figure C.1:** Bulk representative diffraction patterns of pellets sintered at 1150 °C for 1h (P-1150 °C@1h/M).

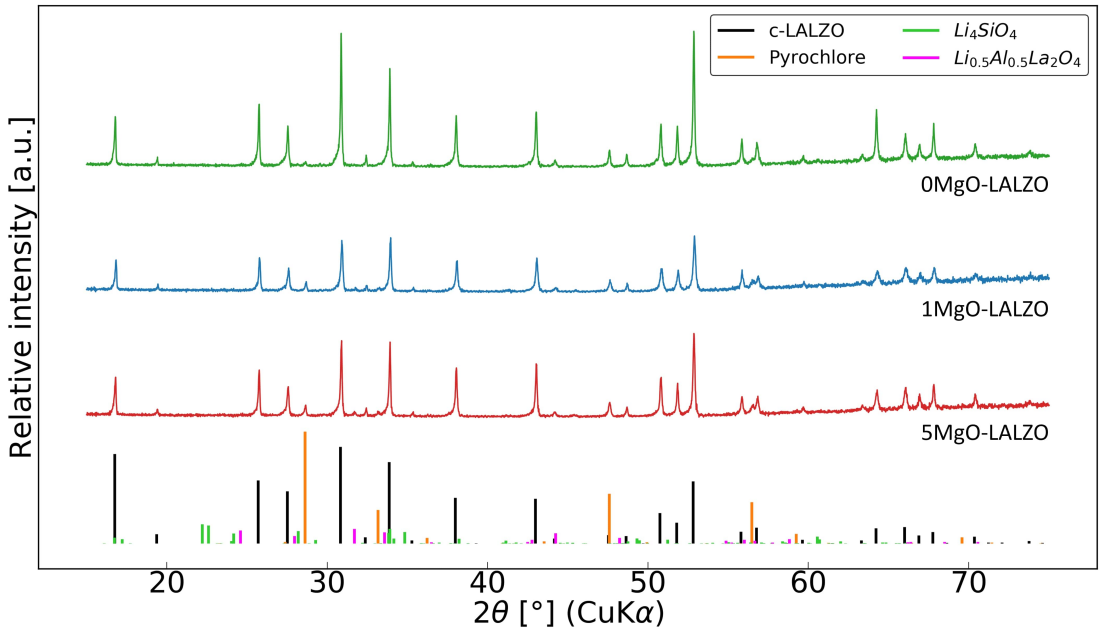


**Figure C.2:** Bulk representative diffraction patterns of pellets sintered at 1200 °C for 1h (P-1200 °C@1h/M).

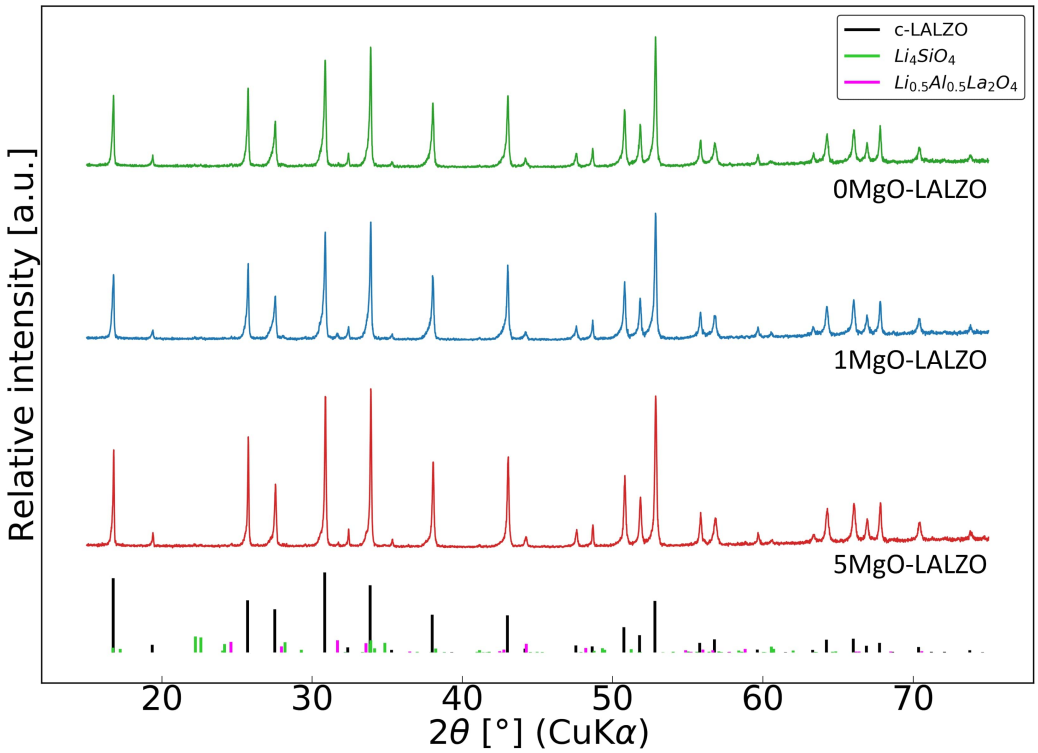


**Figure C.3:** Bulk representative diffraction patterns of pellets sintered at 1150 °C for 1h (P-1150 °C@1h/A).

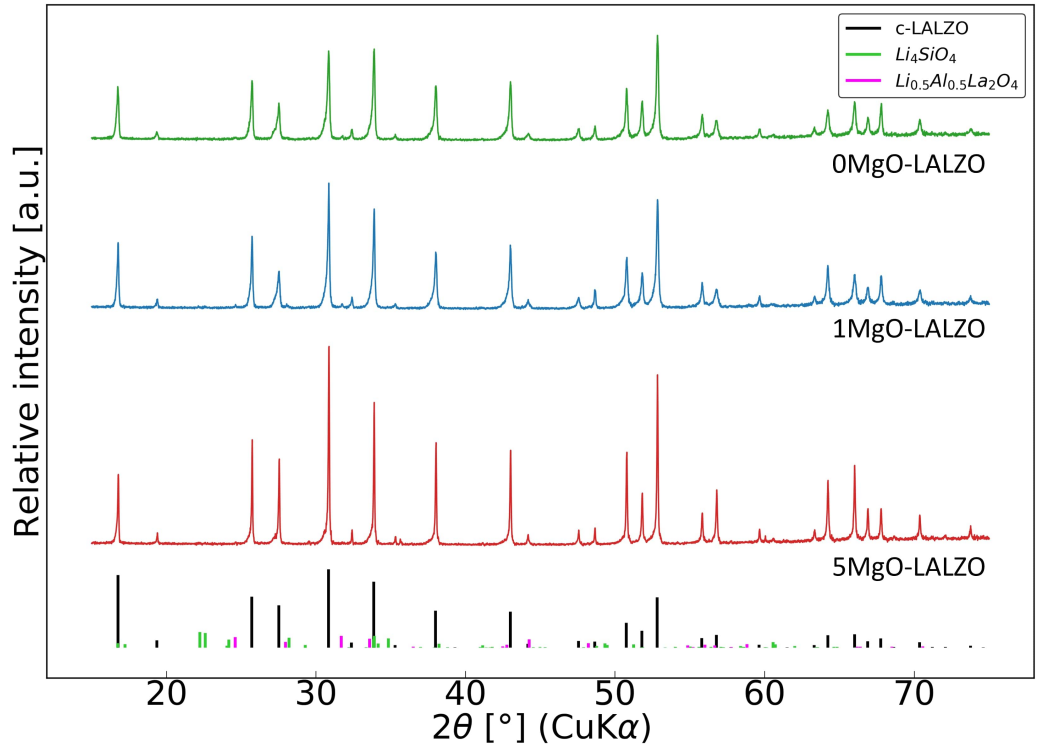


**Figure C.4:** Bulk representative diffraction patterns of pellets sintered at 1150 °C for 6h (P-1150 °C@6h/A).

SEM micrographs of the polished surfaces of pellets sintered at 1150 °C for 1 h (P-1150 °C@1h/M) are shown in Figure C.5. The images reveal the distribution of the pyrochlore ($La_2Zr_2O_7$) intermediate phase. Pyrochlore consists of heavy elements, meaning that it will appear as bright. Most of the microstructure is dominated by "gray" c-LALZO grains, with the pores being shown as black. However, the large black clusters observed in some of the samples is believed to be SiC-contamination from the sandpaper used during polishing. The polishing also left some significant stripes in the grains. The microstructure of 0 MgO – LALZO and 5 MgO – LALZO consists of a larger fraction pyrochlore, compared to 1 MgO – LALZO. This confirms what was observed in the diffractograms shown in Figure C.1, where the pyrochlore peak intensity is lower for 1 MgO – LALZO.

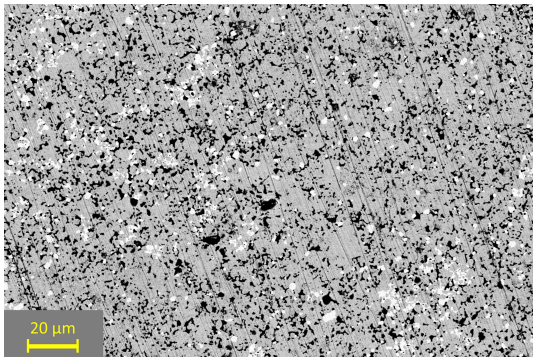


**(a)** 0MgO, P-1150 °C@1h/M, Low magnification

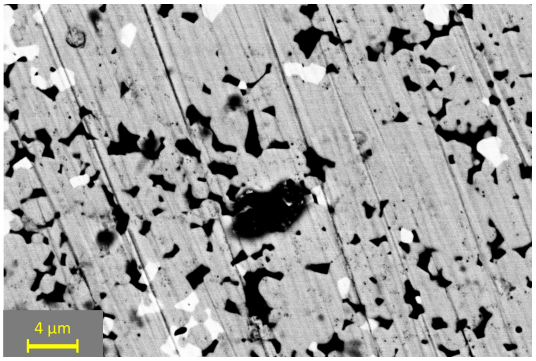


**(b)** 0MgO, P-1150 °C@1h/M, High magnification

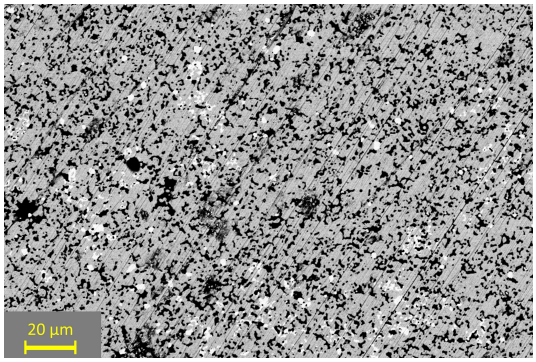


**(c)** 1MgO, P-1150 °C@1h/M, Low magnification

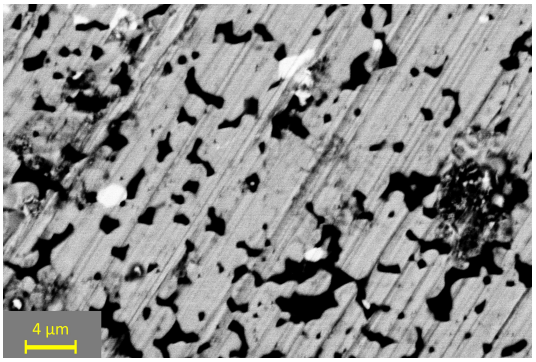


**(d)** 1MgO, P-1150 °C@1h/M, High magnification

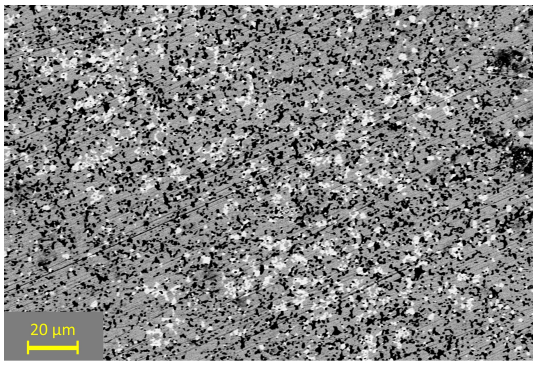


**(e)** 5MgO, P-1150 °C@1h/M, Low magnification

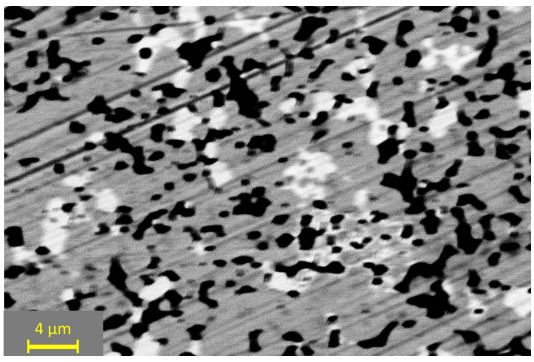


**(f)** 5MgO, P-1150 °C@1h/M, High magnification

**Figure C.5:** Backscatter electron micrographs of the polished surfaces of pellets sintered at 1150 °C for 1 h (P-1150 °C@1h/M).

Figure C.6 shows the microstructure of the 5 MgO – LALZO samples that experienced AGG, which was the case for samples sintered at (a) and (b): 1200 °C for 1 h (P-1200 °C@1h/M) and (c) and (d): 1150 °C for 6 h (P-1150 °C@6h/A). AGG also occurs for the other sample stoichiometries as well. Large grains have formed in an otherwise homogeneous, small-grained microstructure. The large grains are very dense, with some small pores entrapped within. Most of these grains are centered along the surface edges of the pellets, with only a few being observed near the center.

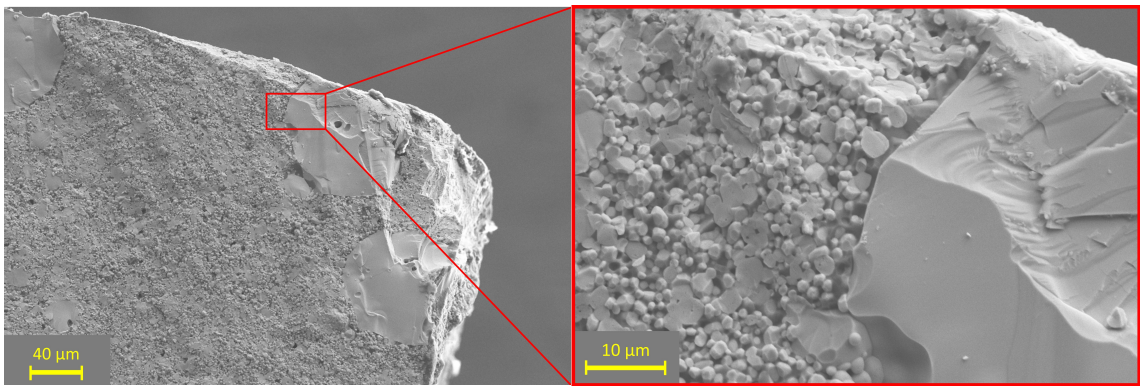


**(a)** 5MgO, P-1200 °C@1h/M, Low magnification **(b)** 5MgO, P-1200 °C@1h/M, High magnification

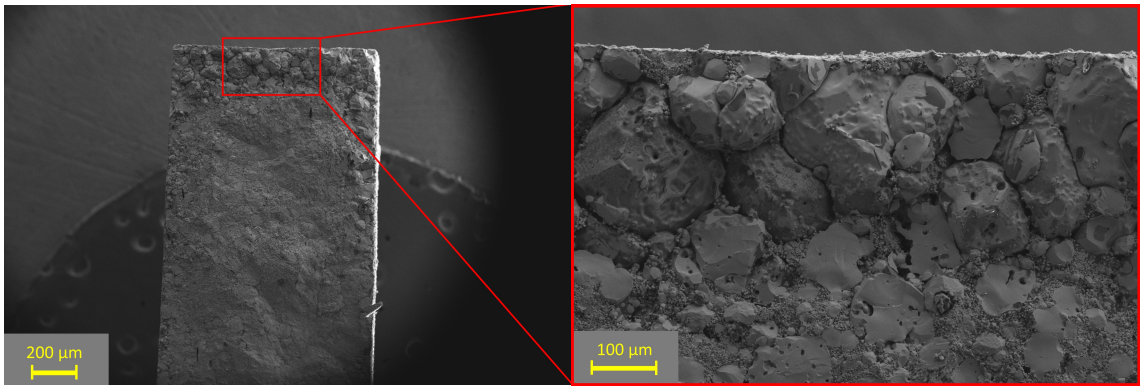


**(c)** 5MgO, P-1150 °C@6h/A, Low magnification **(d)** 5MgO, P-1150 °C@6h/A, High magnification

**Figure C.6:** Secondary electron micrographs of pristine fracture surfaces of 5 MgO – LALZO samples that experienced abnormal grain growth during the preliminary sintering study.

Similar to what was observed for the samples sintered for 6 h in the main sintering study, large grains can also be observed on the "as received" surfaces of the AGG-prone samples studied during the preliminary sintering experiments. This is shown in Figure C.7, for the 0 MgO–LALZO samples at 1200 °C for 1 h (P-1200 °C@1h/M, Figure C.7a) and at 1150 °C for 6 h (P-1150 °C@6h/A, Figure C.7b). This also applies for the other sample stoichiometries as well.

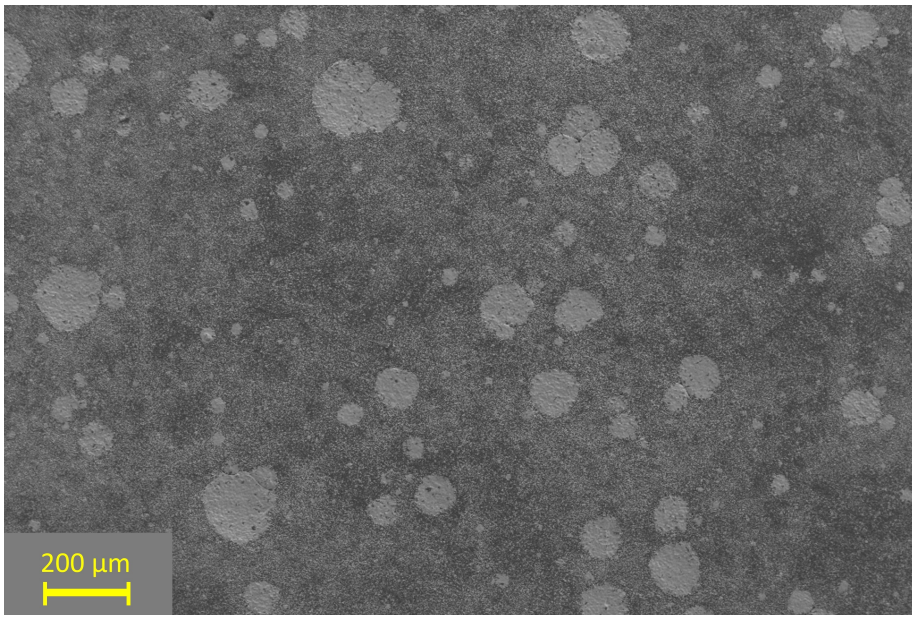


**(a)** 0MgO, P-1200 °C@1h/M

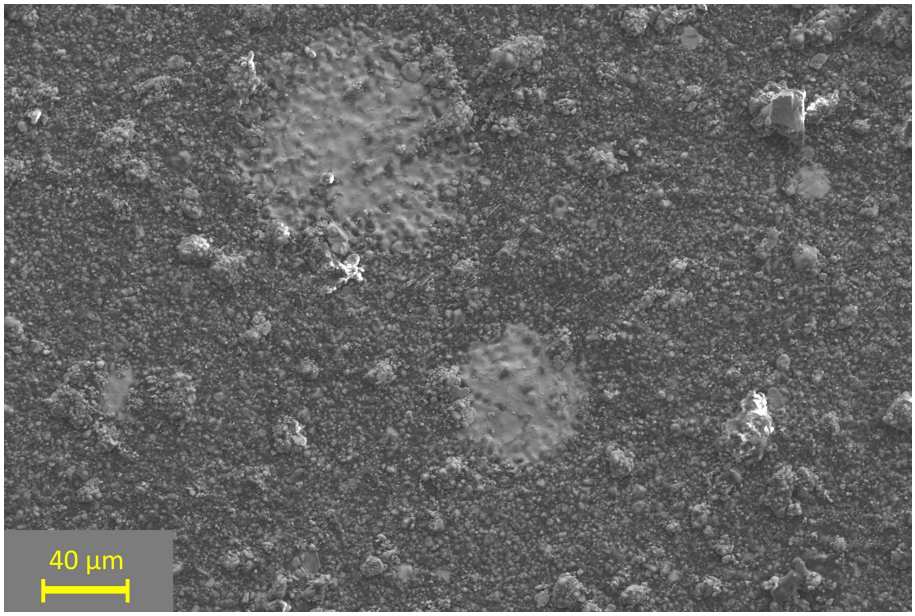


**(b)** 0MgO, P-1150 °C@6h/A

**Figure C.7:** Secondary electron micrographs of the "as received" surfaces of 0 MgO–LALZO pellets sintered at (a) 1200 °C for 1 h (P-1200 °C@1h/M) and (b) 1150 °C for 6 h (P-1150 °C@6h/A).

Figure C.8 shows both the "as received" pellet surface and the bulk of the pellet as observed in the cross sectional fracture surface for the AGG-prone 5 MgO – LALZO sample sintered at 1150 °C for 6 h (P-1150 °C@6h/A). The contrast between these two surfaces is evident from these images. Figure C.8a shows the accumulation of large grains along the surface edges of the pellet, while the fraction of large grains is smaller near the center of the pellet as shown in Figure C.8b. Similar observations were made during the main sintering study as well.

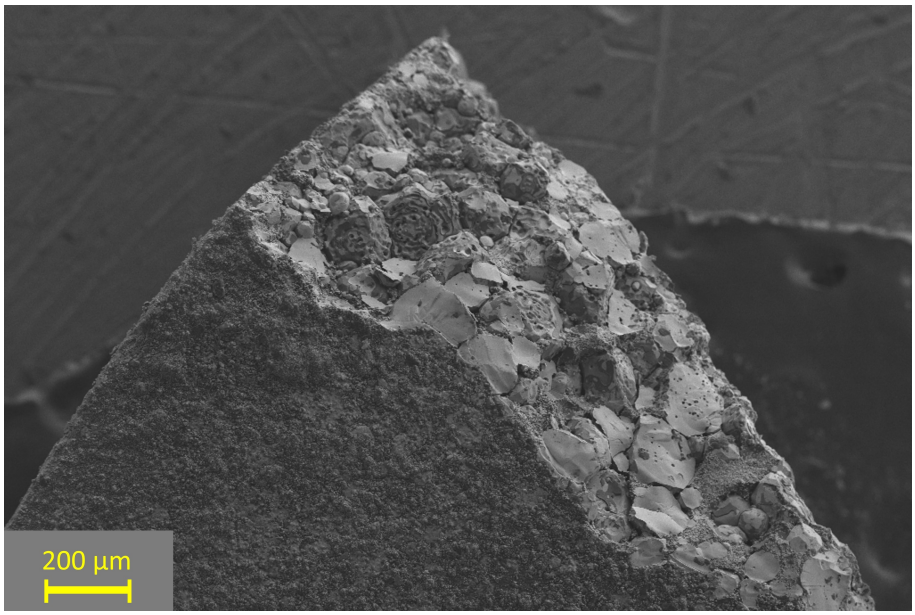


**(a)** 5MgO, P-1150 °C@6h/A, Near edge

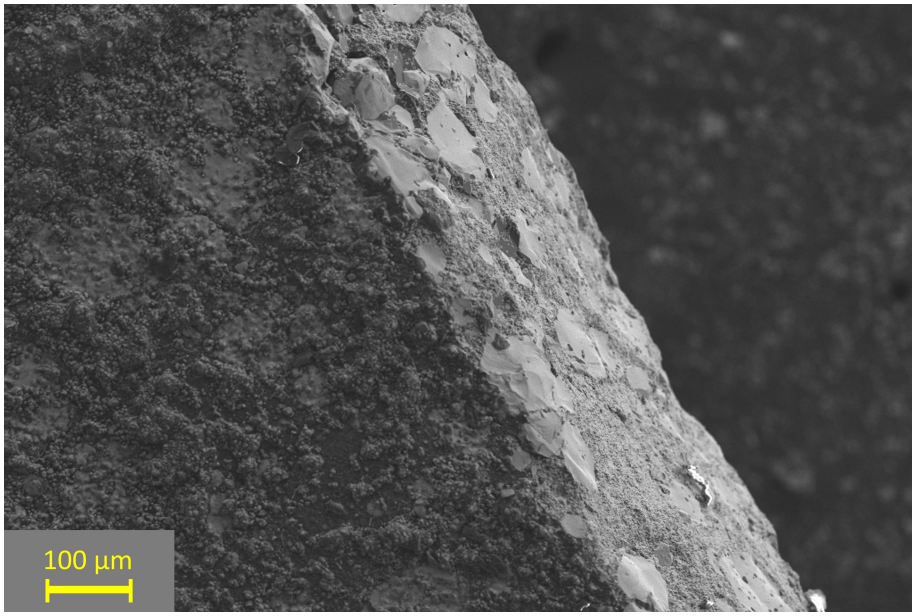


**(b)** 5MgO, P-1150 °C@6h/A, Near center

**Figure C.8:** Secondary electron micrographs showing both the "as received" surfaces and the fracture surface of the 5 MgO – LALZO pellets sintered at 1150 °C for 6 h (P-1150 °C@6h/A). Displaying the formation of large grains (a) Near edge of the pellet and (b) Near center of the pellet

# D EDS mapping

Figure D.1 shows the micrographs of the polished fracture surfaces of samples sintered at 1150 °C for 6 h (M-1150 °C@6h/M). The samples were casted in epoxy, followed by both dry- and diamond suspension polishing. In the high magnification images, the scanning area analysed during EDS mapping is marked with a green rectangle. Here, a 21 kV accelerating voltage and a 120 $\mu$m aperture was implemented.

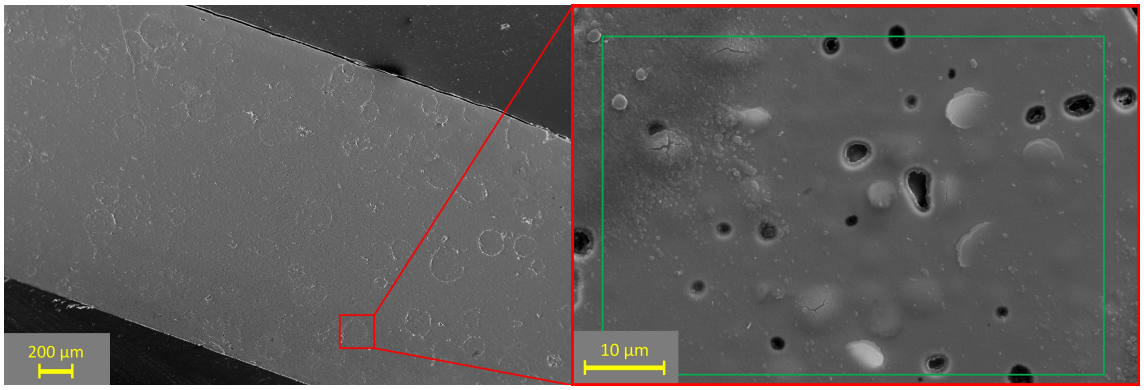


**(a)** 0MgO, M-1150 °C@6h/M, Low magnification **(b)** 0MgO, M-1150 °C@6h/M, High magnification

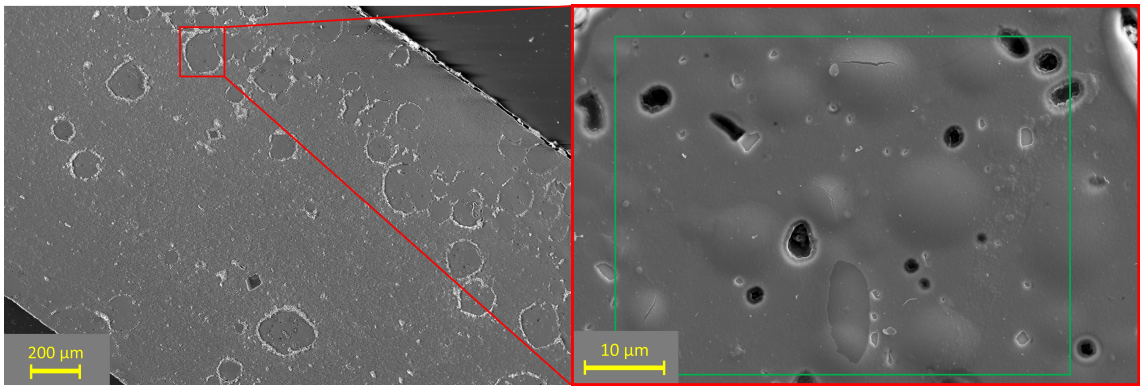


**(c)** 1MgO, M-1150 °C@6h/M, Low magnification **(d)** 1MgO, M-1150 °C@6h/M, High magnification

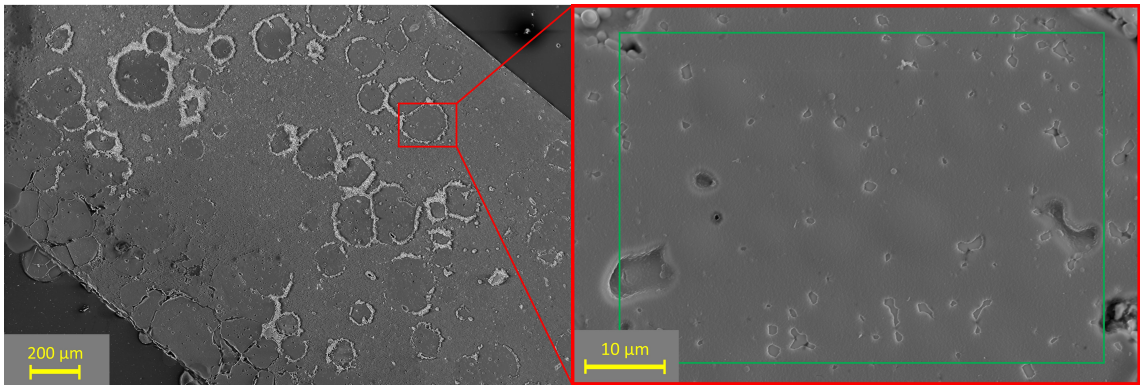


**(e)** 5MgO, M-1150 °C@6h/M, Low magnification **(f)** 5MgO, M-1150 °C@6h/M, High magnification

**Figure D.1:** Secondary electron micrographs of polished fracture surfaces of samples sintered at 1150 °C for 6 h (M-1150 °C@6h/M). The EDS mapping area for each sample is marked with a green rectangle.

## E Fitted Nyquist diagrams and related information

The results from the EIS-measurements are presented in Nyquist diagrams, as shown in Figure 4.14. The data was fitted using the ZFit-software from BioLogic, using one of the two equivalent circuits shown in Figure 3.7. The best fit for the Nyquist diagrams of each sample, along with the corresponding equivalent circuits, are shown in Figure E.1. The impedance and total ionic conductivity for the equivalent circuits shown in Figure 3.7a) and Figure 3.7b) is calculated using Equation E.1 and Equation E.2, respectively. The best fit parameters obtained when fitting the experimental data are listed in Table E.1 and was obtained from the ZFit BioLogic software. The values needed to calculate the total ionic conductivity are: The total resistance of the equivalent circuit, $R_{tot}$ (corresponds to $R_1$ or $(R_1+R_2)$ depending on the equivalent circuit), the thickness and the cross sectional area of the sintered pellets. The relevant values are listed in Table E.2.

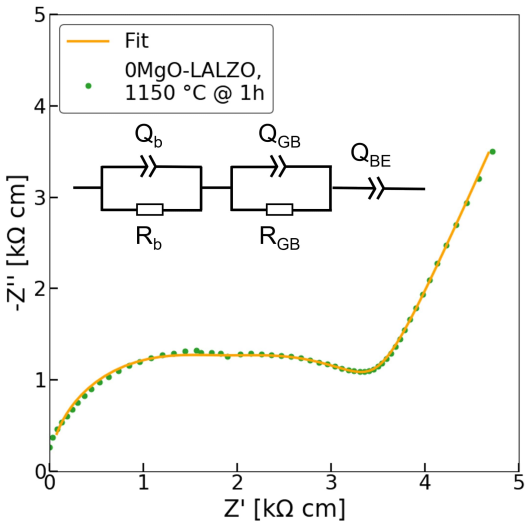


**(a)** 0 MgO–LALZO, E-1150 °C@1h/M

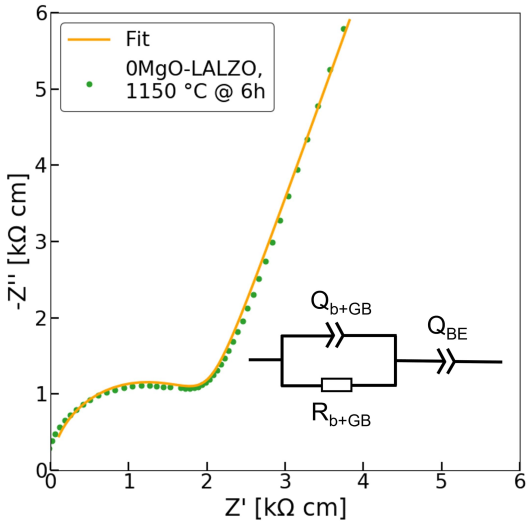


**(b)** 0 MgO–LALZO, E-1150 °C@6h/M

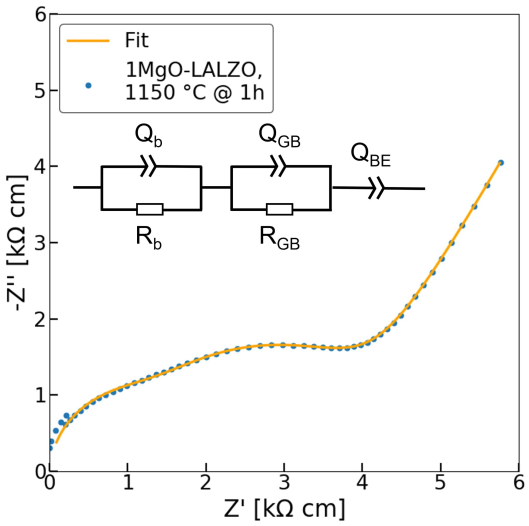


**(c)** 1 MgO–LALZO, E-1150 °C@1h/M

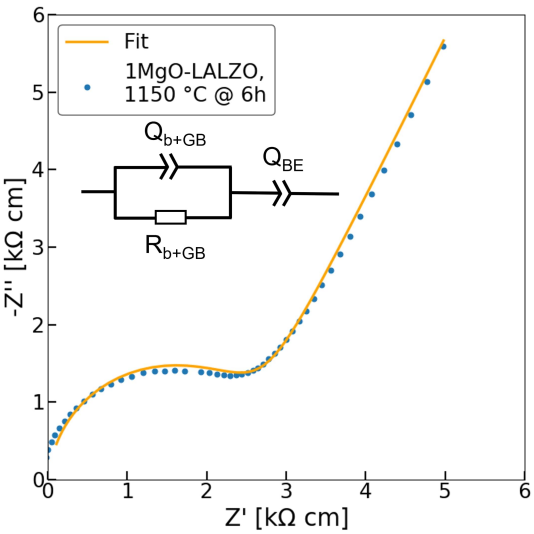


**(d)** 1 MgO–LALZO, E-1150 °C@6h/M

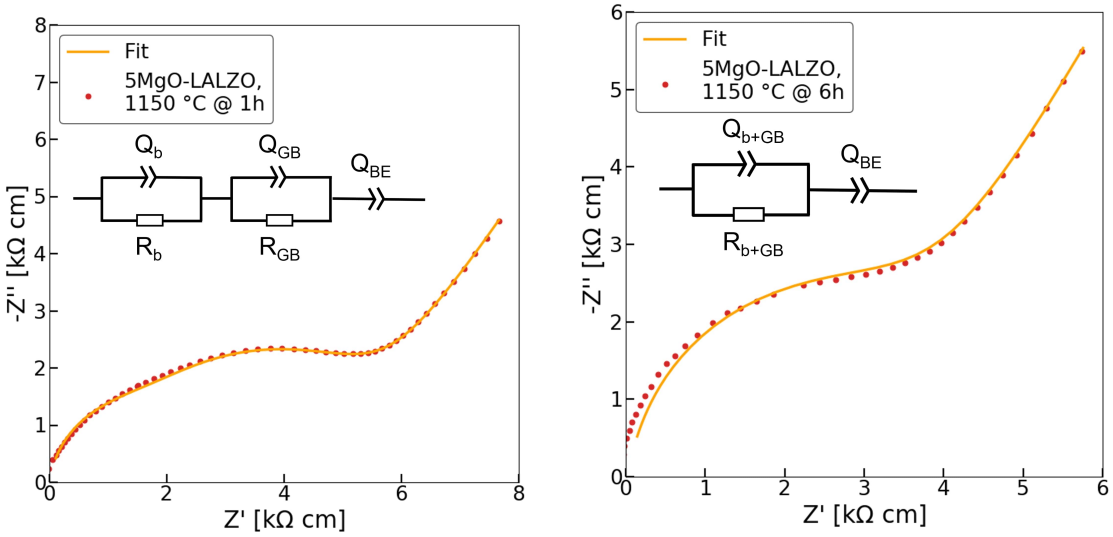


**(e)** 5 MgO–LALZO, E-1150 °C@1h/M **(f)** 5 MgO–LALZO, E-1150 °C@6h/M

**Figure E.1:** Normalized Nyquist diagrams for samples sintered for the EIS-measurements. The best fit of the data, based on the corresponding equivalent circuits as marked in the figure, is also included. Z' is the real part of the impedance, while Z" is the imaginary part of the impedance. Q = Constant phase element, R = Resistance element, b = Bulk, GB = Grain boundary and BE = Blocking electrode.

$$Z(\omega) = \frac{R_1}{R_1 Q_1 (i\omega)^{\alpha_1} + 1} + \frac{R_2}{R_2 Q_2 (i\omega)^{\alpha_2} + 1} \Rightarrow \sigma_{tot} = \frac{t}{R_1 A} \tag{E.1}$$

$$Z(\omega) = \frac{R_1}{R_1 Q_1 (i\omega)^{\alpha_1} + 1} + \frac{R_2}{R_2 Q_2 (i\omega)^{\alpha_2} + 1} + \frac{R_3}{R_3 Q_3 (i\omega)^{\alpha_3} + 1} \Rightarrow \sigma_{tot} = \frac{t}{(R_1 + R_2) A} \tag{E.2}$$

**Table E.1:** Summary of the best fit parameters from the impedance data, as calculated by EC-lab. $\alpha$ = Phase argument of the CPE [-], Q = Magnitude of the CPE [F · s$^{\alpha}$ − 1] and $R$ = Resistance [Ω]].

| Sample | $Q_1$ | $\alpha_1$ | $R_1$ | $Q_2$ | $\alpha_2$ | $R_2$ | $Q_3$ | $\alpha_3$ |
|---|---|---|---|---|---|---|---|---|
| 0MgO @ 1h | $0.45 \cdot 10^{-9}$ | 1 | 1819 | $3.36 \cdot 10^{-9}$ | 1 | 1389 | $0.41 \cdot 10^{-6}$ | 0.74 |
| 1MgO @ 1h | $0.58 \cdot 10^{-9}$ | 1 | 1218 | $5.07 \cdot 10^{-9}$ | 0.94 | 2400 | $0.58 \cdot 10^{-6}$ | 0.68 |
| 5MgO @ 1h | $0.90 \cdot 10^{-9}$ | 0.97 | 1540 | $4.36 \cdot 10^{-9}$ | 0.93 | 3356 | $0.71 \cdot 10^{-6}$ | 0.64 |
| 0MgO @ 6h | $0.40 \cdot 10^{-9}$ | 1 | 1780 | $57.95 \cdot 10^{-9}$ | 0.79 | - | - | - |
| 1MgO @ 6h | $0.48 \cdot 10^{-9}$ | 0.99 | 2290 | $0.14 \cdot 10^{-6}$ | 0.72 | - | - | - |
| 5MgO @ 6h | $0.50 \cdot 10^{-9}$ | 1 | 2931 | $91.98 \cdot 10^{-9}$ | 0.69 | - | - | - |

**Table E.2:** The total resistance, $R_{tot}$, bulk resistance, $R_{tot}$, and the dimensions of the pellets used for EIS-measurements. $t$ = Thickness of polished pellet and $d$ = Diameter of pellet.

| Sintering program | Sample | $R_{tot}$ [Ω] | $R_b$ [Ω] | $t$ [mm] | $d$ [mm] |
|---|---|---|---|---|---|
| E-1150 °C@1h/M | 0 MgO–LALZO | 3208 | 1819 | 1.84 | 8.17 |
| | 1 MgO–LALZO | 3618 | 1218 | 1.87 | 8.12 |
| | 5 MgO–LALZO | 4896 | 1540 | 1.84 | 8.05 |
| E-1150 °C@6h/M | 0 MgO–LALZO | 1780 | - | 1.30 | 8.00 |
| | 1 MgO–LALZO | 2290 | - | 1.27 | 8.05 |
| | 5 MgO–LALZO | 2931 | - | 1.32 | 7.97 |

# F Bode plots

The Bode plots for the samples sintered at 1150 °C for both 1 h and 6 h (E-1150 °C@1h/M and E-1150 °C@6h/M) are shown in Figure F.1. Figure F.2 and Figure F.3 shows the individual Bode plots of the various pellet compositions for samples sintered with E-1150 °C@1h/M and E-1150 °C@6h/M, respectively. Each plateau with their corresponding bulk, grain boundary or bulk+grain boundary resistance contributions are marked with dashed lines.

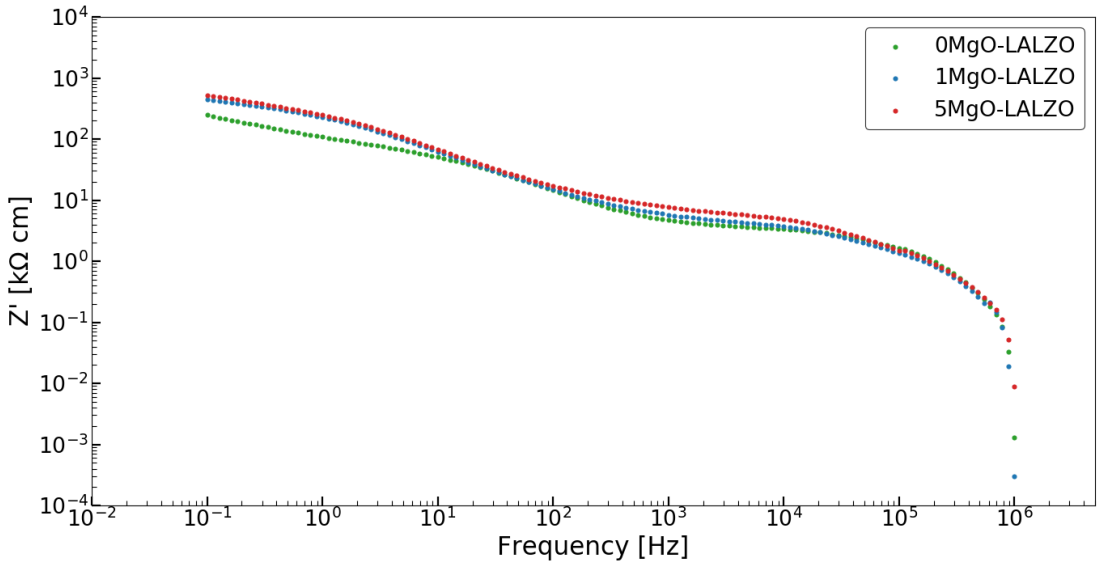


**(a)** E-1150 °C@1h/M

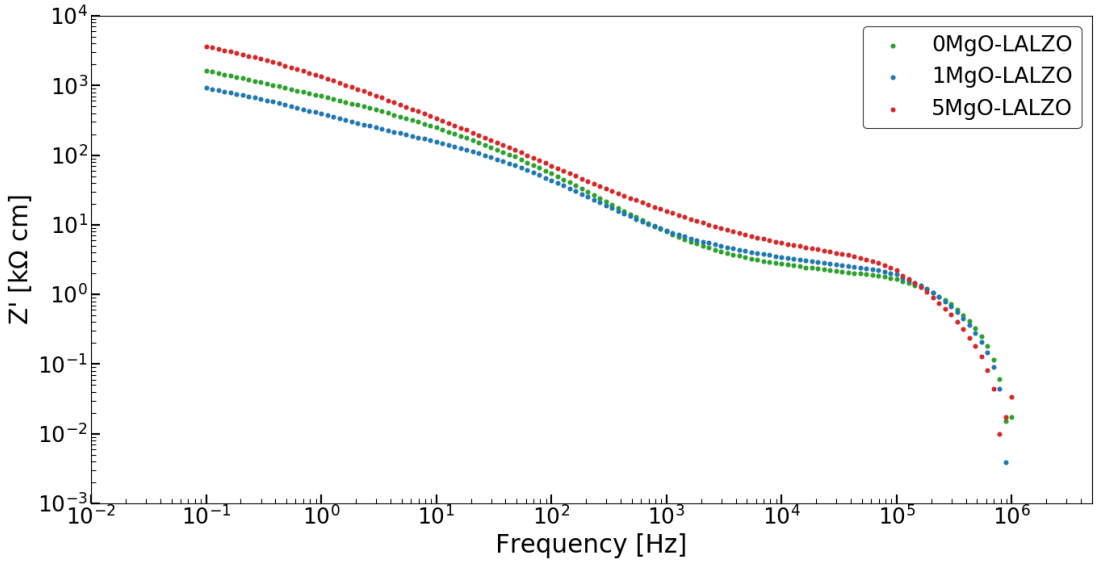


**(b)** E-1150 °C@6h/M

**Figure F.1:** Bode plots of the samples sintered at (a) 1150 °C for 1 h (E-1150 °C@1h/M) and (b) 1150 °C for 6 h (E-1150 °C@6h/M).

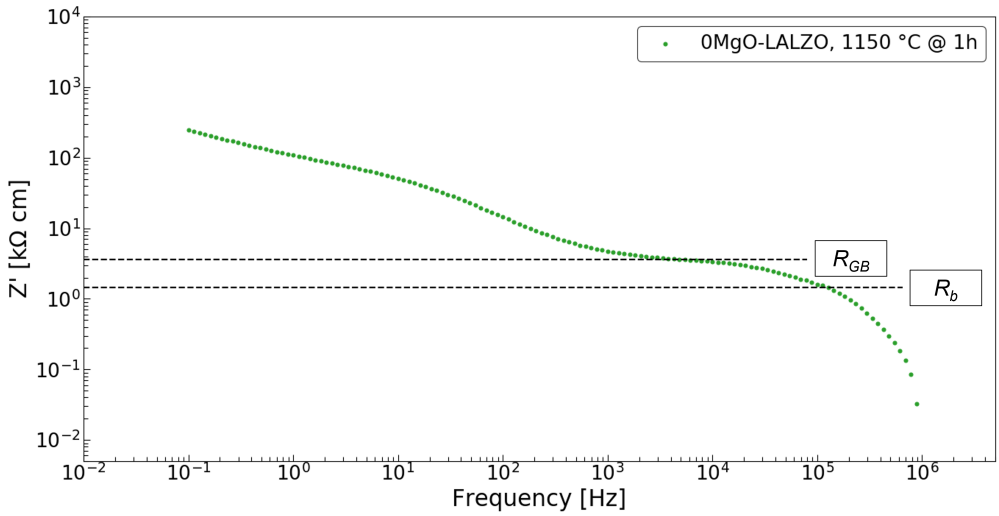


**(a)** 0 MgO–LALZO, E-1150 °C@1h/M

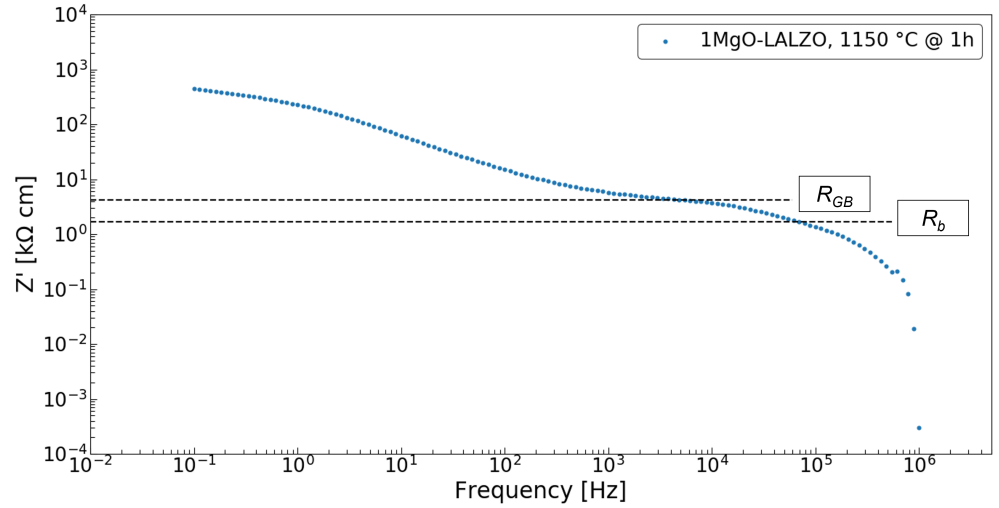


**(b)** 1 MgO–LALZO, E-1150 °C@1h/M

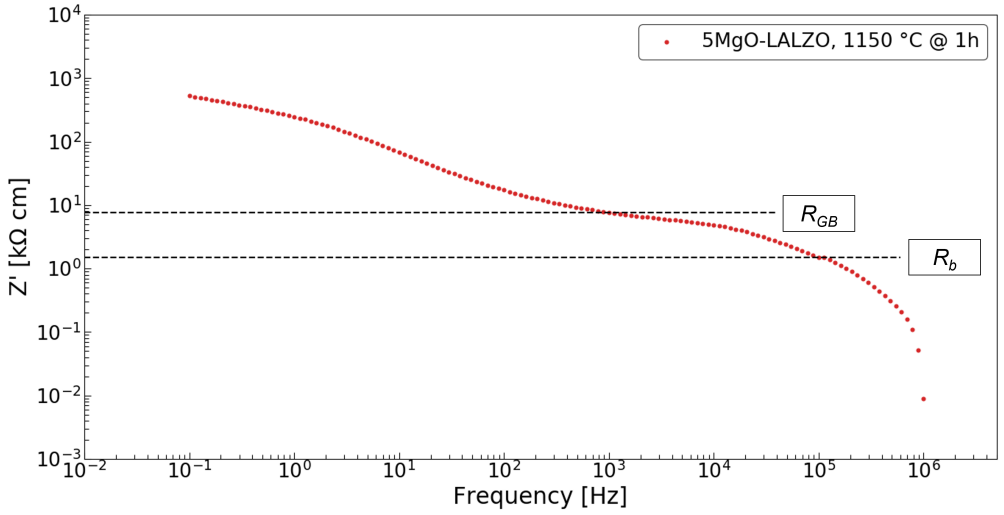


**(c)** 5 MgO–LALZO, E-1150 °C@1h/M

**Figure F.2:** Bode plots of the samples sintered at 1150 °C for 1 h (E-1150 °C@1h/M).

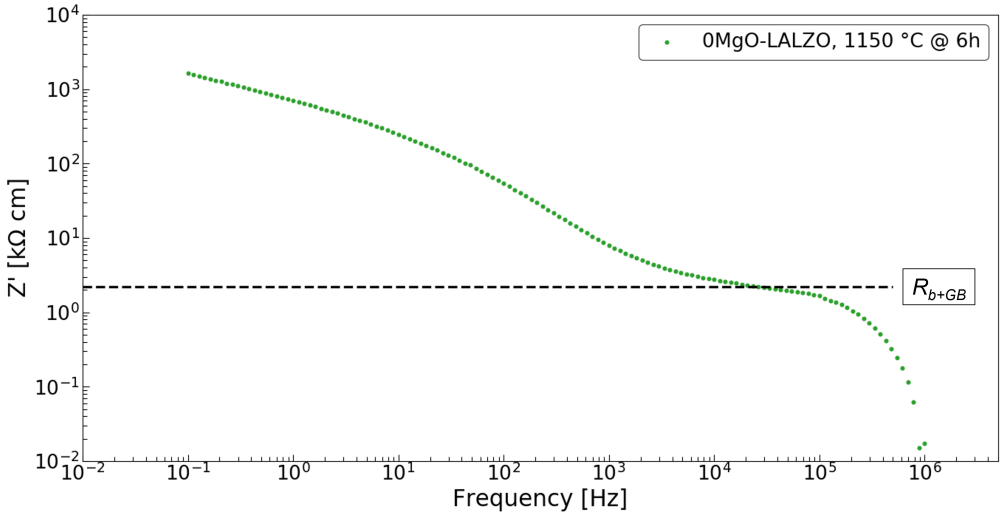


**(a)** 0 MgO–LALZO, E-1150 °C@6h/M

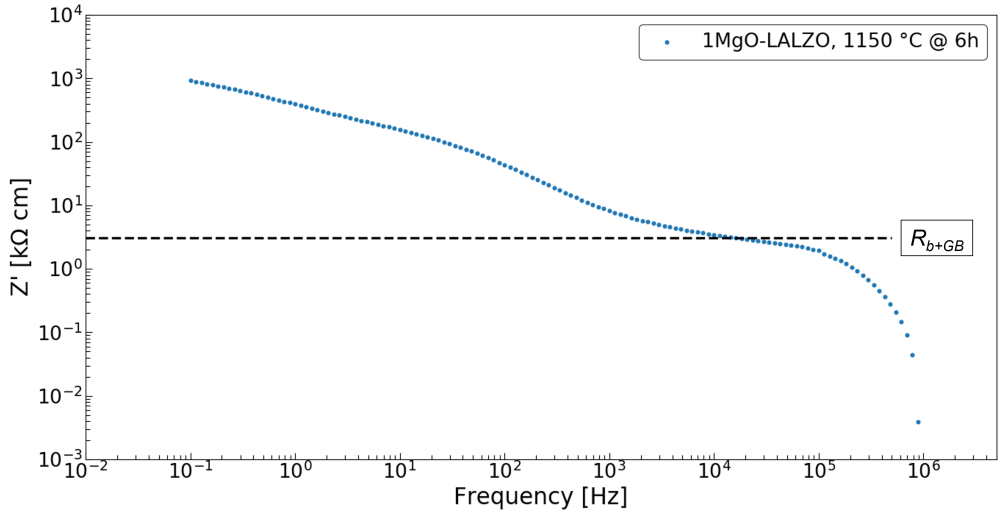


**(b)** 1 MgO–LALZO, E-1150 °C@6h/M

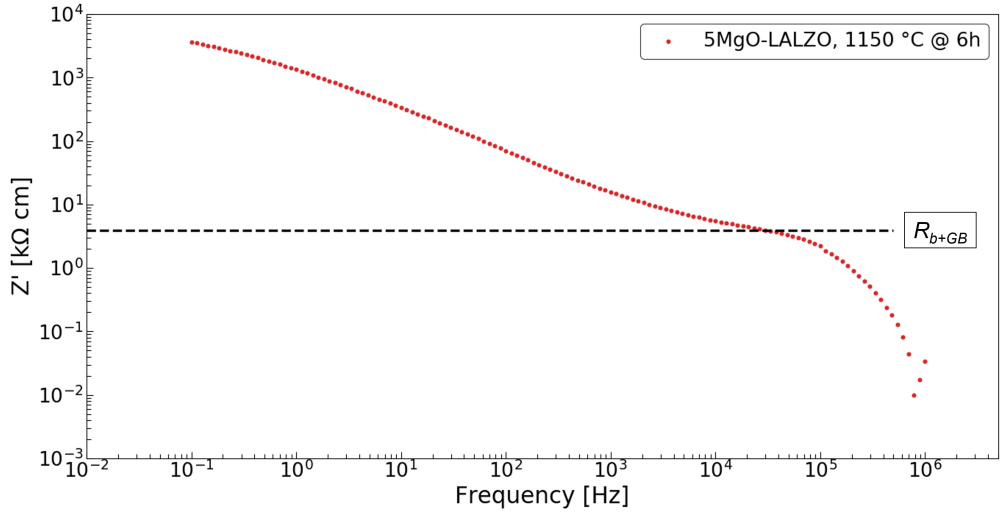


**(c)** 5 MgO–LALZO, E-1150 °C@6h/M

**Figure F.3:** Bode plots of the samples sintered at 1150 °C for 6 h (E-1150 °C@6h/M).

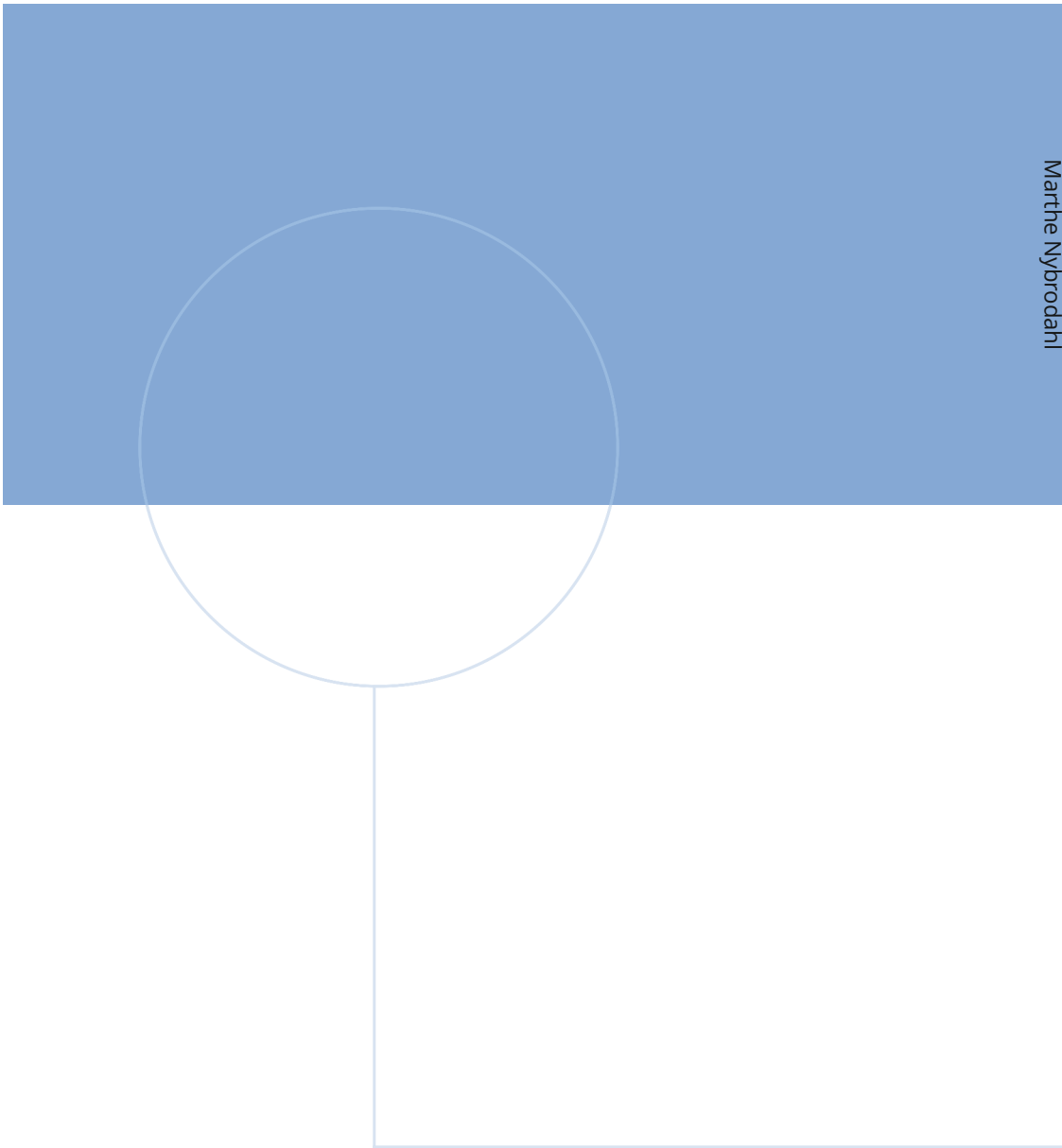

Marthe Nybrodahl

NTNU
Norwegian University of
Science and Technology